TECHNICAL REPORT No. 40

SPECTRAL CHARACTERISTICS OF THE ECMWF OBJECTIVE ANALYSIS SYSTEM

by

Roger Daley*

December 1983

*Visiting Scientist on leave from
National Centre for Atmospheric Research,
Boulder, Colorado 80307

C O N T E N T S

ABSTRACT

Four aspects of the ECMWF multi-variate optimum interpolation analysis system were examined:

(a)   the geostrophic and non-divergence constraints;

(b)   spectral responses;

(c)   the analysis of tropical divergence and

(d)   the analysis of tropical large-scale flow.

A particularly general form of the prediction error correlation model was used which relaxed the conventional non-divergence constraint. A hierarchy of increasingly complex and realistic experiments was performed constrained only by the assumption of two-dimensionality. Many interesting results were obtained, of which two are of particular importance. A slightly divergent generalization of the prediction error correlation model is advantageous in the tropics. Present day observing systems (even to FGGE standards) are incapable of providing acceptable analyses of the large-scale tropical flow.

1. INTRODUCTION

Multi-variate statistical objective analysis, originally developed by Gandin(1963), has gradually become the most widely-used method of meteorological objective analysis. This analysis method, which we will usually refer to as optimum interpolation (OI) has a sturdy statistical framework which is flexible enough to accommodate many generalizations.

The ECMWF has developed a powerful and mature form of the OI algorithm (Lorenc, 1981) which has been used operationally with considerable success. The ECMWF OI philosophy (if not the actual code) is particularly useful for experimentation and generalization.

Objective analysis in general and OI in particular is poor in good pedagogical material as compared with other branches of numerical weather prediction. This has meant that the field is poorly understood by the non-specialist and communication between modellers and analysis specialists has been inhibited. It is one of the intentions of the present work to produce didactic material on OI which will be readily understood by the non-specialist. There are also many empirically derived properties of OI which do not appear in the literature, and yet are useful and reasonable even though they lack a theoretical basis. We will attempt to provide a foundation for some of these empirical facts.

The present work will concentrate on three aspects of OI.

- multi-variate relationships.

- analysis of divergent tropical flows.

- analysis of tropical large-scale flow.

1

We will take a largely non-statistical approach to these problems, even though we are examining a statistically-derived objective analysis procedure. Most of our experiments will be idealized in some aspect or another, but the experiments will become progressively more realistic toward the end of the work. All experiments will be performed within a strictly horizontal framework; problems in the vertical will not be examined.

In Sect. 2 we will sketch the development of the OI formalism following Lorenc (1981). The prediction error covariance model adopted will be particularly general, with a number of novel free parameters. One of these free parameters will be used to control the level of divergence in the analysis. We will attempt to determine realistic values of these parameters.

In Sect. 3 we will examine the geostrophic and non-divergence relationships and their effects on OI. We will use a variety of idealized situations and techniques to examine these multi-variate relationships.

In Sect. 4 we will determine the two-dimensional scale response of the multi-box ECMWF analysis system. We will also examine the response of the OI procedure to large-scale spherical Rossby and Kelvin waves.

In Sect. 5 we will perform some realistic analyses of tropical divergent flows using FGGE data. The more general divergent prediction error covariance model developed in Sect. 2 will be tested on these situations.

In Sect. 6 we will examine the problem of analyzing the large-scale tropical flow using artificial data with a realistic spectrum and the FGGE observation network. We will test both the ECMWF OI technique and a least-square technique especially designed for the analysis of the long-waves.

2. BASIC THEORY

In this section will be developed the basic theory for the experiments to be described in later sections. The emphasis will be on those aspects of the theory which are important in the three questions we wish to investigate – namely multi-variate analysis, planetary-scale analysis and analysis of divergent flows.

The first sub-section will briefly establish the formal optimal interpolation theory and notation following Lorenc (1981).

The second sub-section will describe at some length the statistical covariance models to be used in later experiments. In some respects, these covariance models are more general than those used previously and they have more free parameters. The properties of these covariance models under variation of the free parameters will be investigated. In addition, some attempt has been made to determine realistic values of these parameters.

2.1 Notation and basic method

For the sake of completeness and in order to establish a consistent notation we will repeat here the basic optimal interpolation theory following the development of Lorenc (1981). In particular, the dimensionless form of the equations will be especially useful.

Thus B_i is any observed datum selected for the analysis and A_k any analyzed value within the analysis volume. Following Lorenc (1981) we assume predicted (first-guess) values P_i and P_k and true values T_i, T_k.

Deviations from the true values are denoted by lower case letters

$$a = A - T, \quad b = B - T, \quad p = P - T \tag{1}$$

3

All analyzed, observed or predicted values have associated error estimates E defined by

$$E^a = \langle a^2 \rangle^{\frac{1}{2}} \, , \quad E^p = \langle p^2 \rangle^{\frac{1}{2}} \, , \quad E^o = \langle b^2 \rangle^{\frac{1}{2}} \tag{2}$$

where angle brackets indicate an ensemble average.

In the non-dimensional form of the equations variables are divided by the appropriate prediction error estimates E^p. Thus

$$\varepsilon^o \alpha = a/E^p \qquad q = (B-P)/E^p \qquad \varepsilon^a = E^a/E^p$$

$$\varepsilon^o \beta = b/E^p \qquad r = (A-P)/E^p$$

$$\pi = P/E^p \qquad \varepsilon^o = E^o/E^p$$

The analyzed deviation from the prediction is given by a linear combination of N observed deviations

$$r_k = \sum_{i=1}^{N} W_{ik} \, q_i \tag{4}$$

which can be re-written in matrix notation as

$$r_k = W_k^T \, q$$

where $W_k = \begin{bmatrix} W_{ik} \end{bmatrix}$ and $q = \begin{bmatrix} q_i \end{bmatrix}$.

Squaring (4) and taking the ensemble average gives

$$(\varepsilon_k^a)^2 = 1 - 2 \, W_k^T \, h_k + W_k^T \, M \, W_k$$

where $h_k = \langle \pi_i \, \pi_k \rangle$.

4

and $\quad M = \left[\, < \pi_i \, \pi_j > \; + \; \varepsilon_i^o < \beta_i \, \beta_j > \; \varepsilon_j^o \, \right]$.

and we have assumed that the correlation between prediction error and observation error $< \pi_i \, \beta_j > \; = 0$. Superscript "T" indicates matrix transpose.

The "optimum" weights can be derived from (6) simply by minimizing with respect to each W_k in turn, which gives

$$W_k = M^{-1} \, h_k$$

and $\quad r_k = h_k^T \; M^{-1} \; q^-$

and the the estimated analysis error is

$$(\, \varepsilon_k^o \,)^2 \; = \; 1 \; - \; h_k^T \; M^{-1} \; h_k$$

2.2 Error statistics

As in Lorenc (1981) we must define the prediction and observation errors E^p and E^o and the prediction error and observation error correlations $<\pi_i \, \pi_j>$ and $<\beta_i \, \beta_j>$. E^p and E^o will be defined to be constant in any analysis box. $<\pi_i \pi_j>$ and $<\beta_i \beta_j>$ are normally functions of position and variable. In all the work to be described we will assume uncorrelated observational error — that is $<\beta_i \beta_j> = \varepsilon_o^2 \delta_{ij}$ where δ_{ij} is the Kronecker delta function. Thus $<\beta_i \beta_j>$ appears only as a positive augmentation of the main diagonal of the M matrix of equation (6).

5

As pointed out by Lorenc (1981) one of the most important aspects of the optimum interpolation formalism (particularly when using the box method employed at ECMWF) is the choice of model for the prediction error correlation $< \pi_i \ \pi_j >$. Consequently, we shall devote some effort to the development of such a model. The present procedure can be considered a generalization of that developed by Lorenc (1981) - although the further developments discussed here are implicit in Lorenc (1979).

We will derive the following non-dimensional prediction error correlations (bearing in mind that we are primarily concerned with the horizontal problem)

$$< u_i \ u_j > \ , \quad < v_i \ v_j > \ , \quad < u_i \ v_j > \ , \quad < u_i \ z_j > \ , \quad < v_i \ z_j > \ , \quad < z_i \ z_j >$$

where u and v are the wind components and z is the geopotential height. As in Lorenc (1981) we will use the scalar correlations of velocity potential(χ) and streamfunction (ψ). We will assume that the scalar correlations are homogeneous and isotropic. Thus we define 6 scalar correlations and characteristic scales as follows:

$$< \psi_1 \ \psi_2 > \ = \ E_\psi^2 \ F \ (r_{12}) \qquad\qquad\qquad - b_\psi$$

$$< \chi_1 \ \chi_2 > \ = \ E_\chi^2 \ G \ (r_{12}) \qquad\qquad\qquad - b_\chi$$

$$< \psi_1 \ \chi_2 > \ = \ < \chi_1 \ \psi_2 > = E_\chi \ E_\psi \ H(r_{12}) \qquad\qquad - b_{\chi\psi}$$

$$< z_1 \ \psi_2 > \ = \ < \psi_1 \ z_2 > = E_z \ E_\psi \ I(r_{12}) \qquad\qquad - b_{z\psi}$$

$$< z_1 \ \chi_2 > \ = \ < \chi_1 \ z_2 > = E_z \ E_\chi \ J(r_{12}) \qquad\qquad - b_{z\chi}$$

$$< z_1 \ z_2 > \ = \ E_z^2 \ K(r_{12}) \qquad\qquad\qquad - b_z$$

where F,G,H,I,J, and K are assumed to be non-dimensional correlations and $< \psi_1 \ \psi_2 >$, $< \chi_1 \ \chi_2 >$ etc. are assumed to be dimensional. r_{12} is the

dimensional scalar distance between arbitrary points 1 and 2.

$$r_{12} = \quad (x_1 - x_2)^2 + (y_1 - y_2)^2$$

where x_1, x_2 and y_1, y_2 are the cartesian coordinates of the points. Using Helmholtz's Theorem

$$u = -\frac{\partial \psi}{\partial y} + \frac{\partial \chi}{\partial x} \qquad\qquad v = \frac{\partial \psi}{\partial x} + \frac{\partial \chi}{\partial y}$$

we can derive the following dimensional prediction error covariances

$$<u_1 u_2> = E_\psi^2 \Gamma \left[F(r_{12}) \right] + E_\chi^2 \Delta \left[G(r_{12}) \right]$$

$$+ 2 E_\chi E_\psi \quad \Theta \quad \left[H(r_{12}) \right]$$

$$<v_1 v_2> = E_\psi^2 \Delta \left[F(r_{12}) \right] + E_\chi^2 \Gamma \left[G(r_{12}) \right]$$

$$- 2 E_\chi E_\psi \quad \Theta \quad \left[H(r_{12}) \right]$$

$$<v_1 u_2> = <u_1 v_2> = E_\psi^2 \quad \Theta \quad \left[F(r_{12}) \right] \qquad\qquad (10)$$

$$- E_\chi^2 \quad \Theta \quad \left[G(r_{12}) \right] + E_\chi E_\psi \Lambda \left[H(r_{12}) \right]$$

$$<z_1 u_2> = -<u_1 z_2> = E_z E_\psi \quad \Xi \left[I(r_{12}) \right]$$

$$- E_z E_\chi \quad \Pi \left[J(r_{12}) \right]$$

$$<z_1 v_2> = -<v_1 z_2> = -E_z E_\psi \Pi \left[I(r_{12}) \right]$$

$$- E_z E_\chi \Xi \left[J(r_{12}) \right]$$

$$<z_1 z_2> = E_z^2 K(r_{12})$$

where

$$\Gamma = \left[\ \frac{1}{r}\frac{\partial}{\partial r} \ + \ (y_1 - y_2)^2 \ \frac{1}{r}\frac{\partial}{\partial r}\frac{1}{r}\frac{1}{r} \ \right]$$

$$\Delta = \left[\ \frac{1}{r}\frac{\partial}{\partial r} \ + \ (x_1 - x_2)^2 \ \frac{1}{r}\frac{\partial}{\partial r}\frac{1}{r}\frac{\partial}{\partial r} \ \right]$$

$$\Theta = \left[\ (y_1 - y_2) \ (x_1 - x_2) \ \frac{1}{r}\frac{\partial}{\partial r}\frac{1}{r}\frac{\partial}{\partial r} \ \right]$$

$$\Lambda = \left[\ (y_1 - y_2) \ - \ (x_1 - x_2)^2 \ \right] \frac{1}{r}\frac{\partial}{\partial r}\frac{1}{r}\frac{\partial}{\partial r} \tag{11}$$

$$\Xi = \left[\ \frac{y_1 - y_2}{r} \ \frac{\partial}{\partial r} \ \right]$$

$$\Pi = \left[\ \frac{x_1 - x_2}{r} \ \frac{\partial}{\partial r} \ \right]$$

and where for simplicity we set $r_{12} = r$.

We now make the following assumptions.

$$K = F, \quad I = \mu F, \quad H = \lambda F, \quad J = \lambda^* F$$

where μ, λ, and λ^* are dimensionless constants. μ is the same constant defined by Lorenc (1981) - see his equation 36, which relates the streamfunction-geopotential correlation to the streamfunction-streamfunction correlation. Thus, where the geostrophic relationship is assumed to apply, μ will be large (≈ 1 north of 30 degrees north and ≈ -1 south of 30 degrees south) but will be assumed to be approximately zero in the tropics. λ and λ^* are similar dimensionless constants concerned with the velocity potential-streamfunction and velocity potential- height correlations.

8

We will assume the following relationships between the characteristic scales

$$b = b_z = b_\psi = b_{\psi z} = b_{\chi\psi} = b_{\chi z}$$

and relate G to F by

$$G = F \left(\frac{br}{b_\chi}\right)$$

If we now non-dimensionalize r by b, we can write non-dimensional prediction error correlations

$$\langle u_1 u_2 \rangle^* = (1-\nu)\, \Gamma\, (F) + \nu \Delta\, (G) + 2\sqrt{\nu-\nu^2}\ \lambda\, \Theta\, (F)$$

$$\langle v_1 v_2 \rangle^* = (1-\nu)\, \Delta\, (F) + \nu \Gamma\, (G) - 2\sqrt{\nu-\nu^2}\ \lambda\, \Theta\, (F)$$

$$\langle u_1 v_2 \rangle^* = (1-\nu)\, \Theta\, (F) - \nu\Theta\, (G) + \sqrt{\nu-\nu^2}\ \lambda\, \Lambda\, (F)$$

$$\langle z_1 u_2 \rangle^* = \sqrt{1-\nu}\ \mu\, \Xi\, (F) - \sqrt{\nu}\ \lambda^*\, \Pi\, (F) \tag{12}$$

$$\langle z_1 v_2 \rangle^* = -\sqrt{1-\nu}\ \mu\, \Pi\, (F) - \sqrt{\nu}\ \lambda^*\, \Xi\, (F)$$

$$\langle z_1 z_2 \rangle^* = F$$

where ν is a non-dimensional constant which is the ratio of the prediction error variance in the divergent wind component ($E^2_{v_\chi}$) to the prediction error variance of the total wind(E^2_v). Thus

$$\nu = E^2_{v_\chi} \,/\, E^2_v$$

$$E^2_v = \frac{E^2_\psi}{b^2} + \frac{E^2_\chi}{b^2_\chi} = E^2_{v_\psi} + E^2_{v_\chi} \tag{13}$$

where (*) indicates non-dimensional prediction error correlations which have

9

been normalized by E_v or E_z.

We will assume for most purposes the standard Gaussian functional form for F. Thus

$$F = e^{-.5 \ r^2} \tag{14}$$

By inserting this expression into equation (12) and using equation (11) we can derive the final expressions for the prediction error correlations as in Lorenc (1981). We retain the generality of allowing $b_\chi \neq b$ in order to permit different scales of divergent flow to be analyzed. For example, it may be desirable to have $b_\chi > b$ in order to suppress erroneous small-scale divergent circulations.

Fig. 1 is a plot of the prediction error correlations for the case $v=\lambda=\lambda^*=0$, $b_\chi=b$, $\mu=1$ which is the appropriate parameter setting for the present (1983) ECMWF operational scheme in the Northern Hemisphere extra-tropics. This diagram can be strictly compared with Fig. 3 of Schlatter (1975) and is included here only for convenience. The abscissa is $-3 < x < 3$ and the ordinate is $-3 < y < 3$ in units of b. Thus the zero line in the $v - v$ correlation falls at $x = \pm 1$ and the minimum at $x = \pm \sqrt{3}$.

For some purposes we have also used another function for F - a special case of the second order autoregressive function, which we will refer to as the Markov function.

$$F = (1 + |r|) \ e^{-|r|} \tag{15}$$

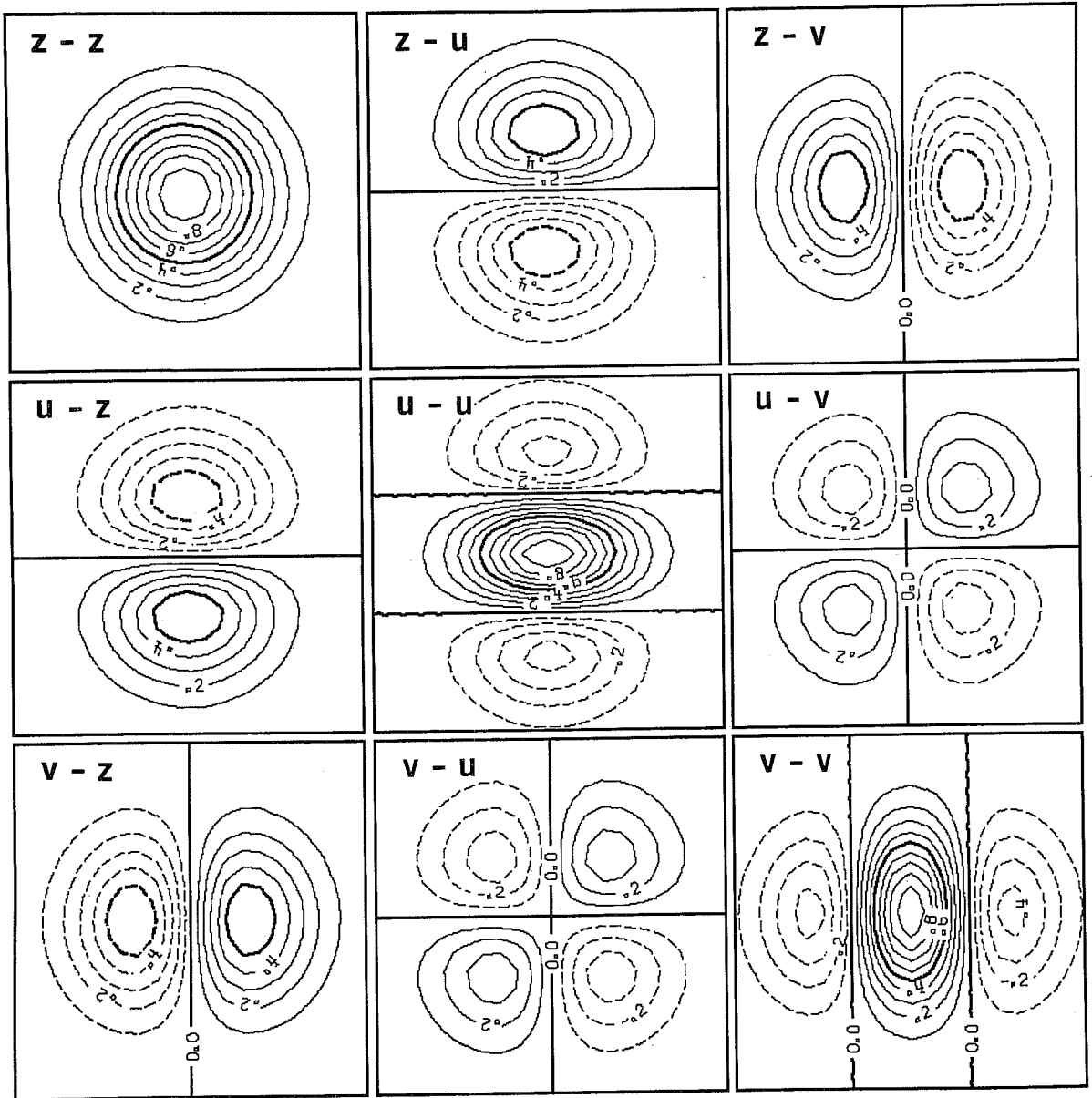We note that the Markov function, like the Gaussian function, satisfies the

Fig. 1 Prediction error correlations for the Gaussian model $\nu=\lambda=\lambda^*=o$, $\mu=1$.
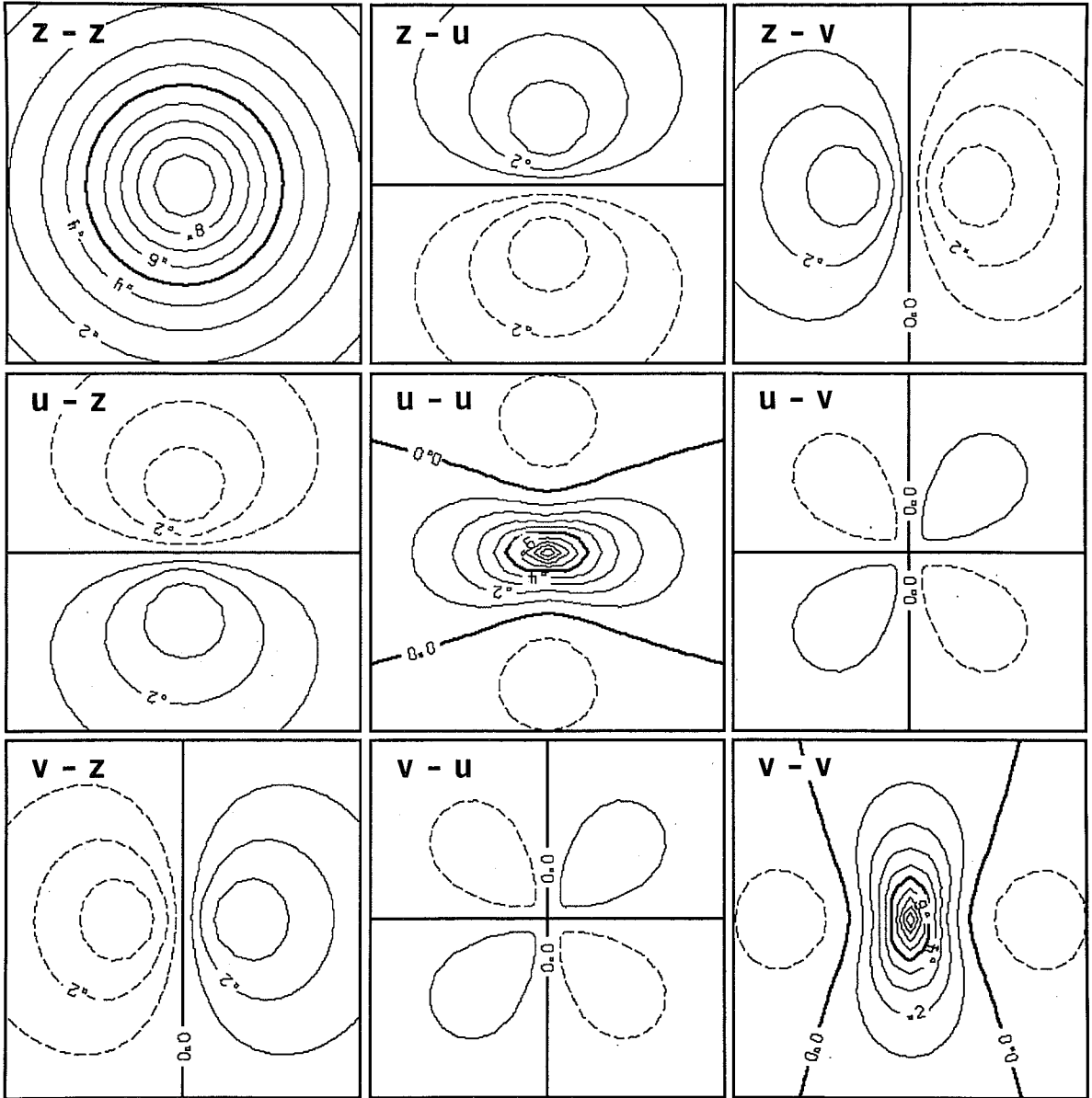
Fig. 2 Prediction error correlations for the Markov model $\nu = \lambda = \lambda^* = 0$, $\mu = 1$.

necessary continuity conditions at $r = 0$ as discussed by Julian and Thiebaux (1975). In Fig. 2 we plot the case $\nu=\lambda=\lambda^*=0$, $\mu=1$, $b_\chi=b$ for the Markov funtion in the same format as Fig. 1.

In comparing Figs. 1 and 2 we see that the Markov function has a much more spread-out $<z-z>$ correlation , but much more concentrated $<u-u>$ and $<v-v>$ correlations. In addition, the negative lobes of the $<u-u>$ and $<v-v>$ correlations are much weaker and the $<u-v>$,$<u-z>$, and $<v-z>$ correlations are also weaker. As we shall see later, there are both advantages and disadvantages of the Markov function as compared to the Gaussian function. We have introduced the Markov model in order to check the sensitivity of various aspects of the analysis procedure to the prediction error correlation model adopted.

For the remainder of this section, we shall be concerned with examining the correlations given by the standard Gaussian model under different settings of the parameters μ, ν, λ and λ^*.

Fig. 3a shows the $<u-u>$ correlation for the case $\lambda=\lambda^*=0$, $b_\chi=b$, $\nu=.5$. The $<v-v>$ correlation is identical and the $<u-v>$ and $<v-u>$ correlations are identically zero. In this case, the divergent and rotational components of the prediction error are equal in magnitude and thus the $<u-u>$ and $<v-v>$ correlations are isotropic, as pointed out by Lorenc (1979). An intermediate case for the $<u-u>$ correlations is shown in Fig. 3b with $\lambda=\lambda^*=0$, $b_\chi=b$, $\nu = .25$. The $<v-v>$ correlation is the same except rotated by 90 degrees. Thus, the effect of varying ν is expansion or contraction along the x or y axes.

In Figs .4 and 5, we examine the effect of varying λ . In Fig. 4a and b we show the $<u-u>$ and $<v-v>$ correlations for the case $\nu = .5$, $\lambda = -1$, $\lambda^* = 0$, $b_\chi = b$. In Figs. 5a and b we show the $<u-u>$ and
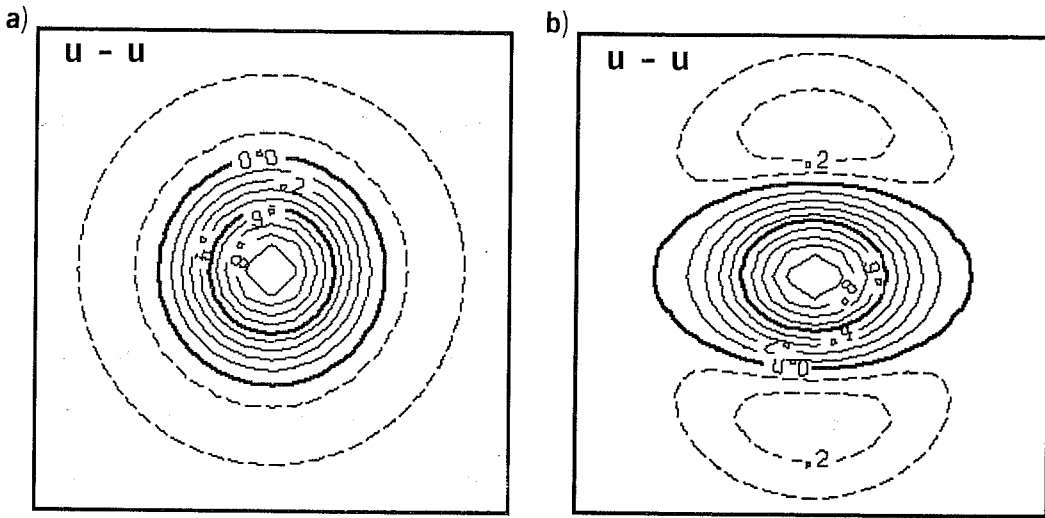
13

Fig. 3 Prediction error correlations (u-u) for the Gaussian model
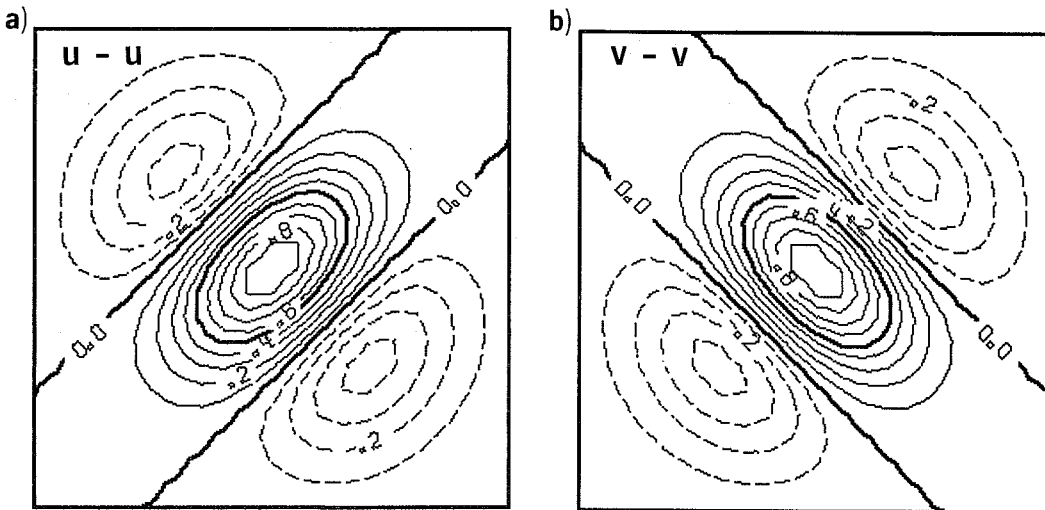$\lambda=\lambda^*=$o. Left $\nu=.5$; right $\nu=.25$.

Fig. 4 Prediction error correlations for the Gaussian model
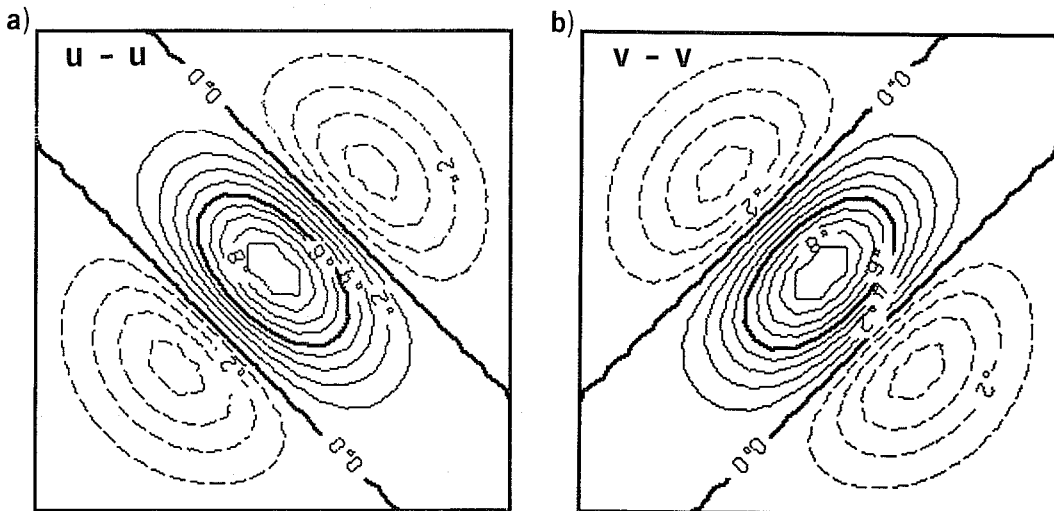$\nu=0.5, \lambda^*=$o$, \lambda=1$. Left (u-u); right (v-v).

Fig. 5 Same as Fig. 4 except $\lambda=-1$.

14

<v-v> correlations for the case $\nu = .5$, $\lambda = -1$, $\lambda* = 0$, $b_\chi = b$. We see that the effect of correlated divergent and rotational wind prediction error is a rotation of the <u-u> and <v-v> correlations.

We note that the <u-u> and <v-v> rotate together in the same direction and, in fact, the <v-u> and <u-v> correlations (not shown) also rotate in the same direction. Experiments performed with varying $\lambda*$ (not shown) also indicate a rotation of the <z-u> and <z-v> correlations. We see from Figs. 4 and 5 that $\lambda < 0$ corresponds to a clockwise rotation while $\lambda > 0$ corresponds to a counter-clockwise rotation. We can calculate the rotation angle as follows. We take the <u-u> equation (12) and insert the Gaussian correlation function (14). We then re-write the expression in cylindrical polar coordinates.

$$
\langle u_1 u_2 \rangle = \left[(1-\nu)(1-r^2 \sin^2\theta) + \nu(1-r^2 \cos^2\theta) \right.
$$
$$
\left. + 2 \sqrt{\nu - \nu^2} \; \lambda \, r^2 \sin\theta \cos\theta \right] F \qquad (16)
$$

where $\theta = \tan^{-1} \left[(y_1 - y_2) / (x_1 - x_2) \right]$

Differentiating equation (16) with respect to θ and setting the result to zero gives the angle of the maximum of $\langle u_1 u_2 \rangle$ as a function of ν and λ. For convenience defining $\nu = \sin^2 \alpha$ we find

$$
\theta_{max} = .5 \tan^{-1} \left[\lambda \tan 2\alpha \right]
$$

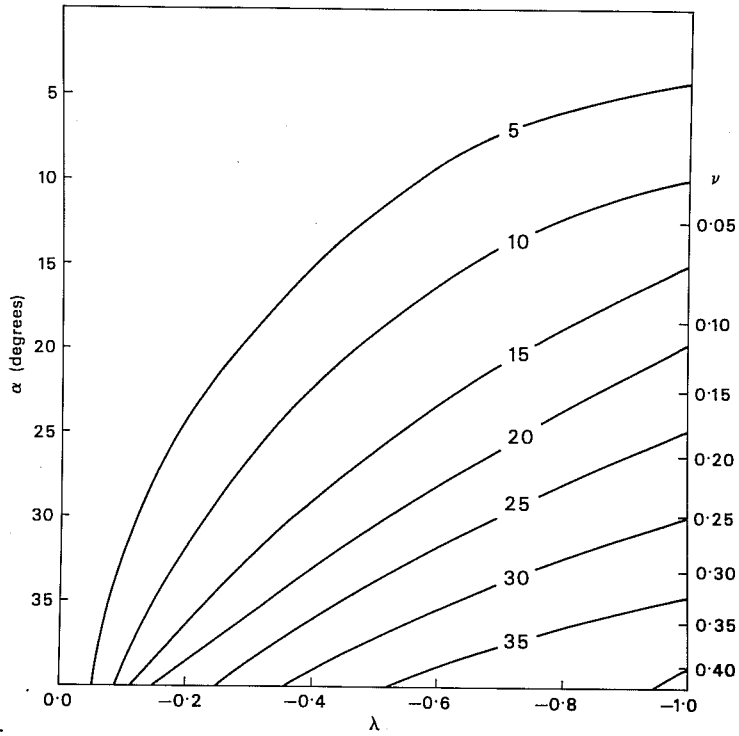These rotational angles are plotted in Fig. 6 as a function of λ and α (or ν).

Fig. 6   Rotation angle (degrees) of the (u-u) prediction
error correlation of the Gaussian model as a
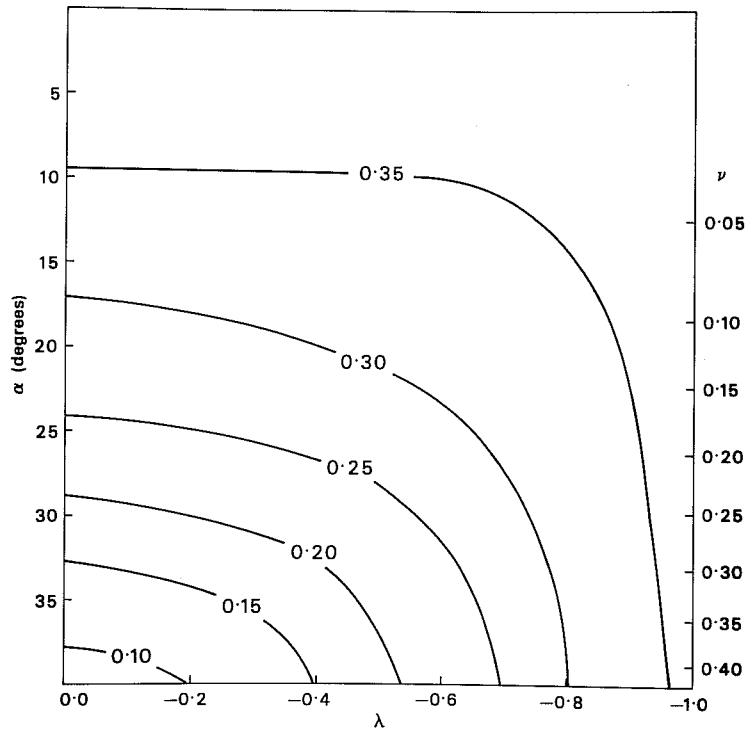function of ν (abscissa) and λ (ordinate).

Fig. 7   Maximum (u-v) correlation of the Gaussian model
as a function of ν (abscissa) and λ (ordinate).

Also of interest is the correlation between u and v as a function of λ and ν. In a similar fashion to equation (16) we can re-write the $<u-v>$ correlation (12).

$$<u_1 v_2> = \left[(1-2\nu) \sin \theta \cos \theta + \lambda \sqrt{\nu \, \nu^2} \left[(\sin^2\theta - \cos^2\theta)\right] \right] r^2 F$$

(17)

where θ, F are defined above. Differentiating this expression with respect to r we find $r_{max} = \sqrt{2}$. Thus, by inserting θ_{max} and r_{max} into equation (17) we find the maximum $<u-v>$ correlation as a function of λ and ν. These results are shown in Fig. 7. The maximum value of the correlation for any value of λ or α is $e^{-1} = .3678$.

The next task is to find appropriate values for ν, λ and λ^*. We shall first consider the problem of determining suitable values for λ and λ^*.

In this work we have naturally been concerned with the correlations of observations minus prediction as is appropriate for most applications of the optimal interpolation method. It is of interest, however, to consider the case of observations minus climatology where physical insight might be of some benefit. For example, one might hypothesize that in the Northern Hemisphere there is generally convergence into low pressure (cyclonic flow) and divergence from high pressure (anti-cyclonic flow). Therefore, in the Northern Hemisphere one might expect the $<\psi-\chi>$ correlation to be negative while in the Southern Hemisphere the $<\psi-\chi>$ correlation might be positive. The $<z-\chi>$ correlation one might expect to be negative in both hemispheres. We emphasize again that we are considering the case of observations minus climatology.

If there is, in the atmosphere, any strong correlation between the divergent and rotational components of the wind, this should show up in independent

17

studies of the wind correlation coefficients (observed minus climatology).
Seaman and Gauntlett (1980) summarize the results of several such studies -
Buell (1960,1972), Alaka and Elvander (1972), Ramanathan et al (1973) and
Seaman (1975). Seaman and Gauntlett (1980) argue ,based on these studies,
that there is an anti-clockwise rotation of the <u-u> correlation and a
clock-wise rotation of the <v-v> correlation in the Northern Hemisphere and
the opposite rotation in the Southern Hemisphere. Seaman and Gauntlett's
(1980) observations taken over Australia certainly support this argument.
The Northern Hemisphere observations of the other named authors only weakly
support this arguement, however. Thus, for example, Buell's results (taken
over North America) show a substantial anti-clockwise rotation of the <u-u>
component, but virtually no rotation of the <v-v> component.

The analysis of Seaman and Gauntlett (1980) requires the <u-u> and <v-v>
correlations to rotate in different directions whereas a correlation between
rotational and divergent components (of either sign) requires a rotation in
the same direction. The results of Seaman and Gauntlett (1980) and all
references contained therein does not suggest any particular correlation
between rotational and divergent components of the wind in the atmosphere.
Thus, the plausible hypothesis of a negative correlation between the velocity
potential and the streamfunction (in the Northern Hemisphere) does not seem
to be supported by observation. Whatever correlation there is appears to be
swamped by other effects of inhomogeneity or non-representativeness.

Of course, it is possible that there is a correlation between the
streamfunction and velocity potential for the case of observed minus
predicted , but at this point it does not seem worth pursuing. Consequently,
in the remainder of this work we shall assume λ and $\lambda* = 0$.

The final task is to obtain an appropriate value for ν. The correct way to do this would be to collect statistics of observed minus predicted rotational and divergent wind components and then calculate ν from equation (13). Unfortunately, we do not observe the rotational and divergent wind components separately and it is necessary to do some areal calculation to separate them. In principle, this can be done using the irregularly-spaced observational network, but in practice it is much simpler using a regularly-spaced grid. Consequently, we decided to calculate ν using the following approximate method due to Arpe (1982)*

The analysis minus predicted values of the wind field (analysis increments) on the standard ECMWF analysis grid were collected for 5 consecutive days (20 analysis periods) from September 15-20, 1982. These were then analyzed into their rotational and divergent components and the resulting variances averaged over longitude and time for the area 20 degrees North to 60 degrees North. From these rotational and divergent variances the following values of ν were obtained.

$$1000 \text{ mb} \qquad \nu = .13$$

$$500 \text{ mb} \qquad \nu = .08$$

$$\text{average } 1000\text{-}200 \text{ mb} \qquad \nu = .10$$

From these values we have chosen $\nu = .10$ as a representative value.

----

* Klaus Arpe - 1982 - personal communication.

3. ASPECTS OF MULTI-VARIATE RELATIONSHIPS

In this section we will be concerned with examining the effects of the two multi-variate relationships commonly used in optimal interpolation - namely, the geostrophic relation and the non-divergence condition. Since these two relationships are unique to meteorology and related disciplines their application in analysis techniques have not been extensively examined by interpolation or statistical theorists. Although the multi-variate aspects of optimal interpolation are undoubtedly amenable to analytic techniques, we will use a number of simpler, practical techniques which nonetheless yield interesting results.

In all cases considered in this section, the results are obtained from one or two-dimensional optimal interpolation schemes applied to a single analysis box. The number of degrees of freedom is small and the arrays of observation points are regular. The three-dimensional analysis box can be considered the fundamental building-block of the ECMWF analysis system and it is always instructive to consider individual box analyses.

We will consider 3 separate techniques for examining single box analyses.

(a) Examination of the analysis weights (W_k in equation 7).

(b) Examination of the eigen-structure of the prediction error correlation.

(c) Examination of the scale-dependent response of the analysis.

We also use the analysis box technique to investigate potential difficulties in longwave analysis.

3.1 Examination of the analysis weight

We will define a 5x5 two-dimensional observation network as in Fig. 8. The dependent variables u, v, and z are defined at each of the 25 points of the grid - which is in fact an Arakawa A-grid (Mesinger and Arakawa-1976). The grid-distances Δx and Δy are defined to be equal. We use the normalized form of the analysis equations(1-8). The observation error ratio $\varepsilon_0^2 = (E^O/E^P)^2$ is defined to be equal to .25 and the distances are defined in terms of $b = b_x$. The prediction error correlation functions are of the Gaussian form (equation 14). We will consider the analysis points to be identical to the observation points.

We will calculate the analysis weights $W_k = M^{-1} h_k$ (equation 7) for this system. There are $(3 \times 25)^2$ such weights. To reduce the amount of information we will consider the weights given to each of the u, v, z at each of the 25 points in the analysis of u_c, v_c, z_c at the central point (marked c in Fig. 8). We can further reduce the quantity of information by exploiting the symmetries of the problem. Thus, we will consider the $v_c - u$ and $z_c - z$ weights along the diagonal line 1 and the $v_c - v$ and $v_c - z$ weights along line 2. We will examine the analysis weights as a function of r, ν (equations 12 and 13) and observation density ($\Delta x / b$).

In Fig. 9 we show the z-z, v-v and v-z weights as a function of r. In this case $\nu = 0$ and $\Delta x / b = .5$. Thus, for example, the observations along the x axis would be at -1.,-.5, 0.,+.5,+1. In Fig. 9a we show the z-z weights along line 1 of Fig. 8 and in Fig. 9b and c respectively the v-v and v-z weights along line 2. The values $\mu = 1$ (solid line), $\mu = .9$ (dashed line), $\mu = .5$(dash-dot line) and $\mu = 0$ (dot-dot line) are shown. (The $\mu = .5$ line has been omitted in v-v case). We can regard the $\mu = 1$ and $\mu = 0$ curves as marking the completely geostrophic and completely uncorrelated limits. It is evident that the variation of the weights as a function of μ is highly non-linear. Thus, at $\mu = .9$ the weights have
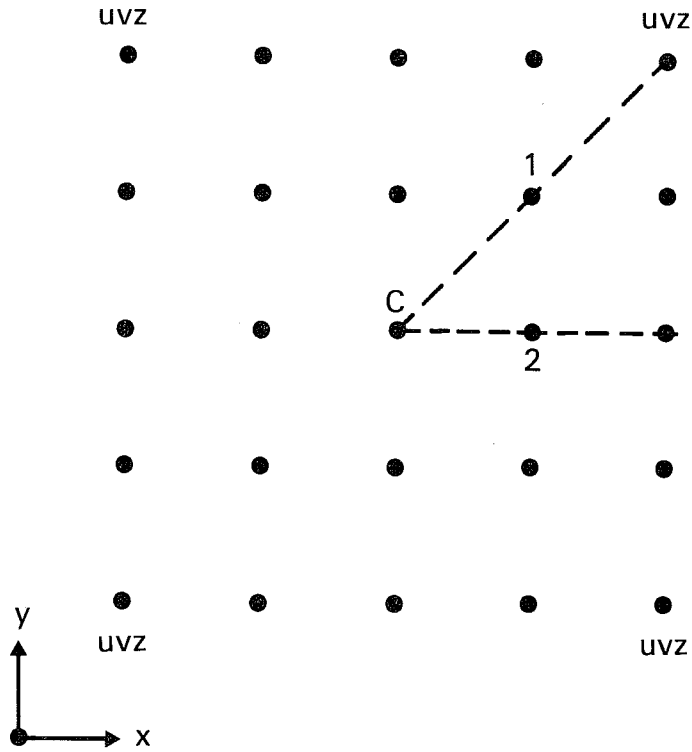
Fig. 8 5x5 two-dimensional observation network used in
        section 3.1. `c´ defines the central point and
        u,v,z are defined at each of the 25 points. Dashed
        lines 1 and 2 define the two cuts through the
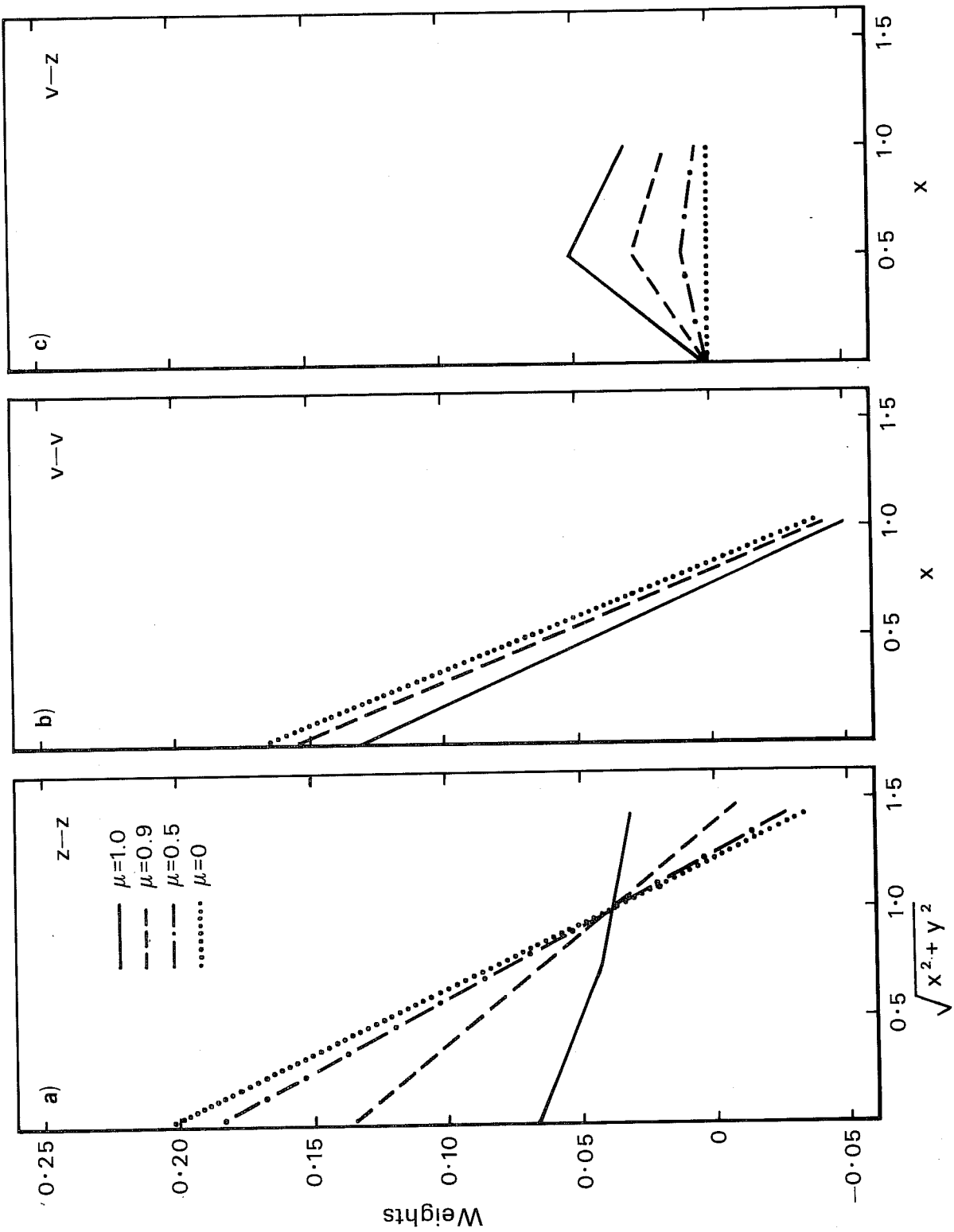   network.

Fig. 9 The z-z, v-v and v-z analysis weights as a function of μ. (ν=o, $\Delta x/b$ = .5).
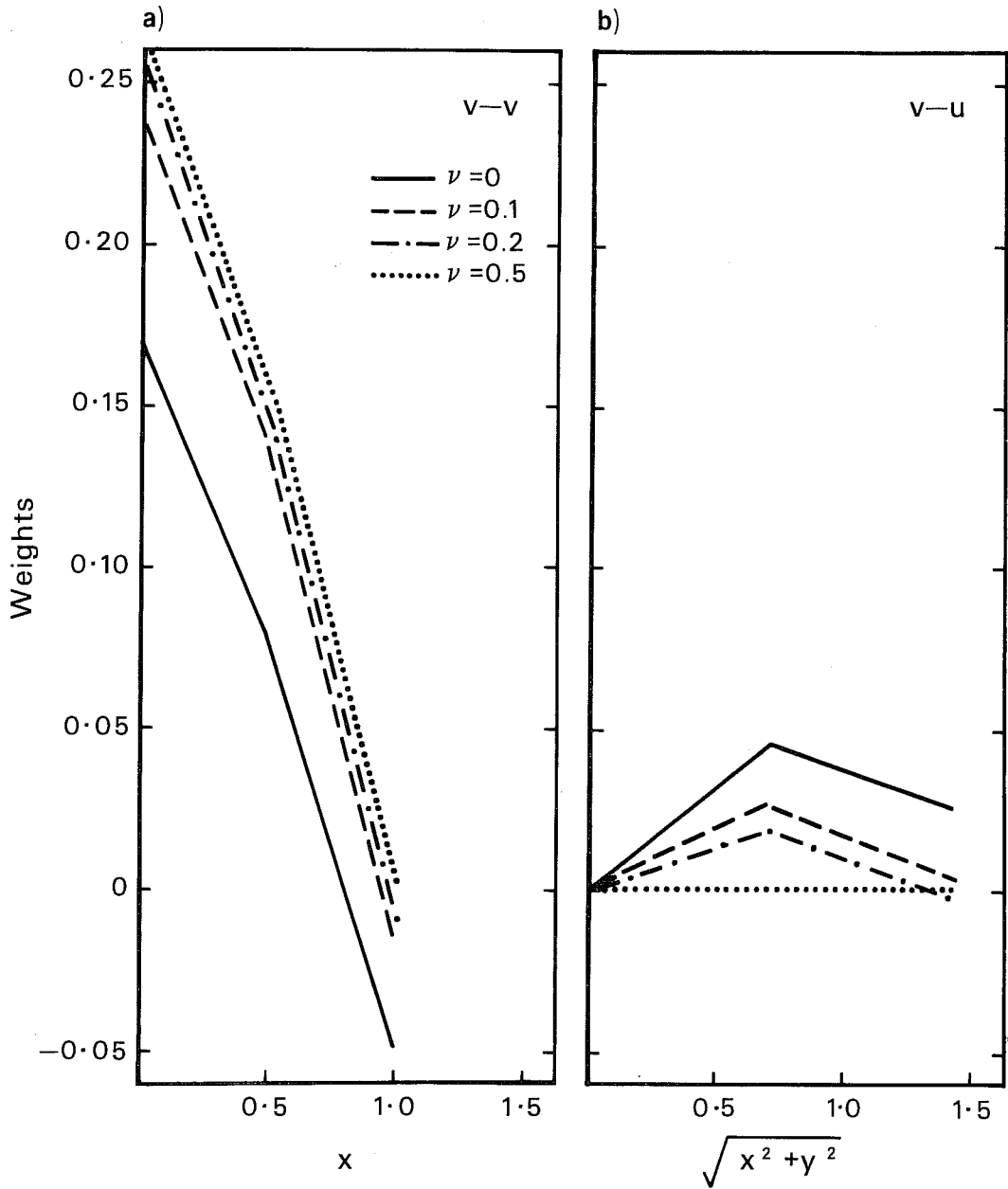
Fig. 10   The v-v and v-u weights as a function of ν in the same format
as Fig. 9   (μ=o., Δ x/b = .5).

already moved half-way between the geostrophic and uncorrelated limits and by $\mu = \cdot 5$ the weights are virtually the same as the uncorrelated weights.

In Fig. 10 we plot the v-v and v-u weights as a function of ν in the same format as Fig. 9. In this case $\mu = 0$ and $\Delta x / b = \cdot 5$. The values $\nu = 0$ (solid line), $\nu = \cdot 1$ (dashed line), $\nu = \cdot 2$ (dash-dot line) and $\nu = \cdot 5$ (dot-dot-dot line) are shown. We can regard $\nu = 0$ as the non-divergent limit and $\nu = \cdot 5$ as the uncorrelated (u-v) limit. Again, the variation of the weights as a function of ν is far from linear and as ν is increased slightly above zero, the weights move rapidly toward the uncorrelated limit.

The analysis is linearly dependent upon the observations (equation 4). It does not appear to be linearly dependent upon the correlations μ and ν. This might be surmised from equation (7) which involves inversion of matrix(M), which is itself linearly dependent upon μ and ν. These results appear to be largely independent (in a qualitative sense) of ε_o^2 , $\Delta x/b$ or the number of observation points.

Similar results (not shown) were obtained for the variation of λ and λ^* of equation (12). The variation of the analysis weights as a function of λ and λ^* was non-linear between the completely correlated and completely uncorrelated limits.

Thus, in all cases where μ, ν, λ and $\lambda*$ are varied the analysis weights are substantially the same as in the uncorrelated limit unless the correlation is assumed to be large. For the Gaussian model, it is tempting to conclude that unless the correlation is large, one might as well assume that the correlation is zero. The results from this section influenced our earlier decision to ignore the $<\psi-\chi>$ and $<\chi-z>$ prediction error correlations.
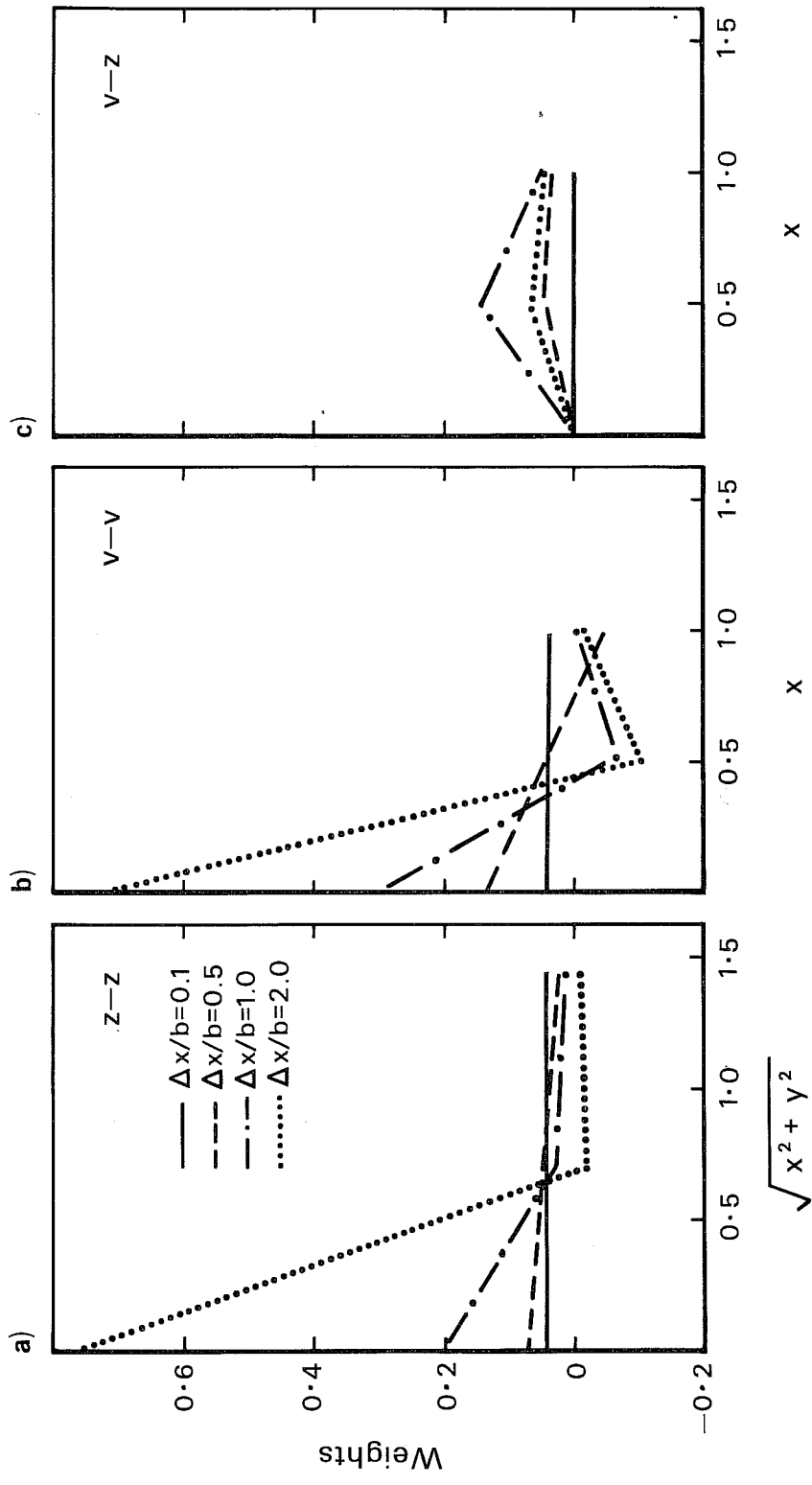
Fig. 11 The z-z, v-v and v-z analysis weights as a function of $\Delta x/b$ for the case $\mu=1$, $\nu=0$, in the same format as Fig. 9.

26

It should be noted, however, with respect to μ that the case considered here has both wind and height input observations. In the case where there are only height observations, or only wind observations, μ appears only in the vector h_k^T of equation (7), not in M^{-1}, and thus the analysis weights would be linear in μ. Thus, in this special case, even a small value of μ might be expected to be of some use in creating analyzed values of the non-observed variable.

We complete this section with plots of the analysis weights z-z, v-v, and v-z as a function of $\Delta x / b$ for the case $\mu = 1$, $\nu = 0$. These plots are shown in Figs. 11a,b,c as a function of x. The cases $\Delta x / b = .1$ (solid line), $\Delta x / b = .5$ (dashed line), $\Delta x / b = 1.$ (dash-dot line) and $\Delta x / b = 2.$ (dot-dot line) are shown. The limiting weight for z - z and v - v cases at $\Delta x / b = \infty$ is $(1 + \varepsilon_o^2)^{-1} = .8$ and the limit at $\Delta x / b = 0$ is $(5 \times 5)^{-1} = .04$. The easiest way to understand Fig. 11 is to assume that the observation analysis network is fixed and that b is varied. It is also possible to imagine that b is fixed and the observation density is varied. Note, that in this latter case the results are somewhat meaningless at low observation density ($\Delta x / b \gg 1$) because there is no consideration of the analysis that would normally be produced in between the widely-scattered observation points.

3.2 Eigenstructure of the prediction error correlation.

A useful technique for investigating the OI procedure is the eigenvector decomposition of the prediction error correlation as described by Hollingsworth (1984). We will use this technique to examine the effect of the geostrophic and non-divergent constraints.

The eigenvector decomposition can be briefly described as follows. The relationship between the analysis increments and the observation increments is described by the scalar equation (7).

$$r_k = W_k^T \, q$$

where r_k is the analyzed deviation from the prediction at the arbitrary

point and q is the column vector of observation deviations at the

observation points $1 \leq i \leq I$. Let us examine the analysis increments at

the I observation points and re-write equation (7) as follows.

$$r = P \, (P+E)^{-1} \, q \tag{18}$$

where r is the column vector of analyzed deviations from the prediction

$1 \leq i \leq I$, P is the prediction error correlation $\langle \pi_i \, \pi_j \rangle$ and E is the

diagonal matrix of $\varepsilon_i^o \, \varepsilon_i^o$.

We will further specify that the $\varepsilon_i^o \, \varepsilon_i^o$ are all equal to ε^2. We are

examining the analysis increments at the observation points and thus the

matrix $P \, (P+E)^{-1}$ can be defined as a response matrix.

Consider the eigenstructure of the matrix P which is of order I. Suppose

P_ℓ is an eigenvector of matrix P.

$$P \, p_\ell = \lambda_\ell \, p_\ell$$

$$P \, (P+E)^{-1} \, p_\ell = \frac{\lambda_\ell}{\lambda_\ell + \varepsilon^2} \, p_\ell = \gamma_\ell \, p_\ell \tag{19}$$

Thus γ_ℓ describes the response of the eigenvector p_ℓ to the OI analysis

procedures defined by $P \, (P + E)^{-1}$. P is a symmetric real matrix so

all the eigenvalues λ_ℓ are real. All the elements of P on the main

diagonal are equal to 1 so that

28

$$\sum_\ell \lambda_\ell = I$$

In general, if $0 < \varepsilon^2 << \lambda_\ell$ then $\gamma_\ell \to 1$. If $0 < \lambda_\ell << \varepsilon^2$ then $\gamma_\ell \to 0$. Usually, P would be positive definite so that λ_ℓ , for all ℓ would be positive. Thus, λ_ℓ large corresponds to a well-resolved structure whereas λ_ℓ small corresponds to a structure which is damped by the analysis procedure.

We will now apply this technique to a simple one-dimensional observation network of heights and winds in order to examine the effect of the geostrophic constraint. The observation network has 5 points lying on the x axis - 3 heights and 2 v winds with the wind and height points interleaved. The points are equi-spaced(Δx) and the characteristic scale of the prediction error correlation is defined to be b. The system has 5 eigenvectors. We will consider the case $\Delta x/b = \cdot 5$, $\nu = 0$.

In Fig. 12 we show the 5 eigenvectors for the case $\mu = 0$ (top row) and $\mu = 1$ (bottom row). The 3 height values are connected by solid lines and the 2 wind points by dashed lines. In the case $\mu = 0$ the height and wind eigenvectors separate out and we have ordered them by decreasing scale as Z_1, Z_2 and Z_3 for the height eigenvectors and W_1 and W_2 for the wind modes. For the case $\mu = 1$ the corresponding eigenvectors G_1 , G_2 , and G_3 are geostrophic and the A_1 and A_2 (again ordered by decreasing scale) are anti-geostrophic. (We define an anti-geostrophic eigenvector when the wind and height gradient have the opposite sense to that defined by the geostrophic relationship.) We see that G_1 is a combination of Z_1 and W_2 , G_2 is a combination of W_1 and Z_2 , G_3 is a combination of W_2, Z_1 and Z_3 etc.
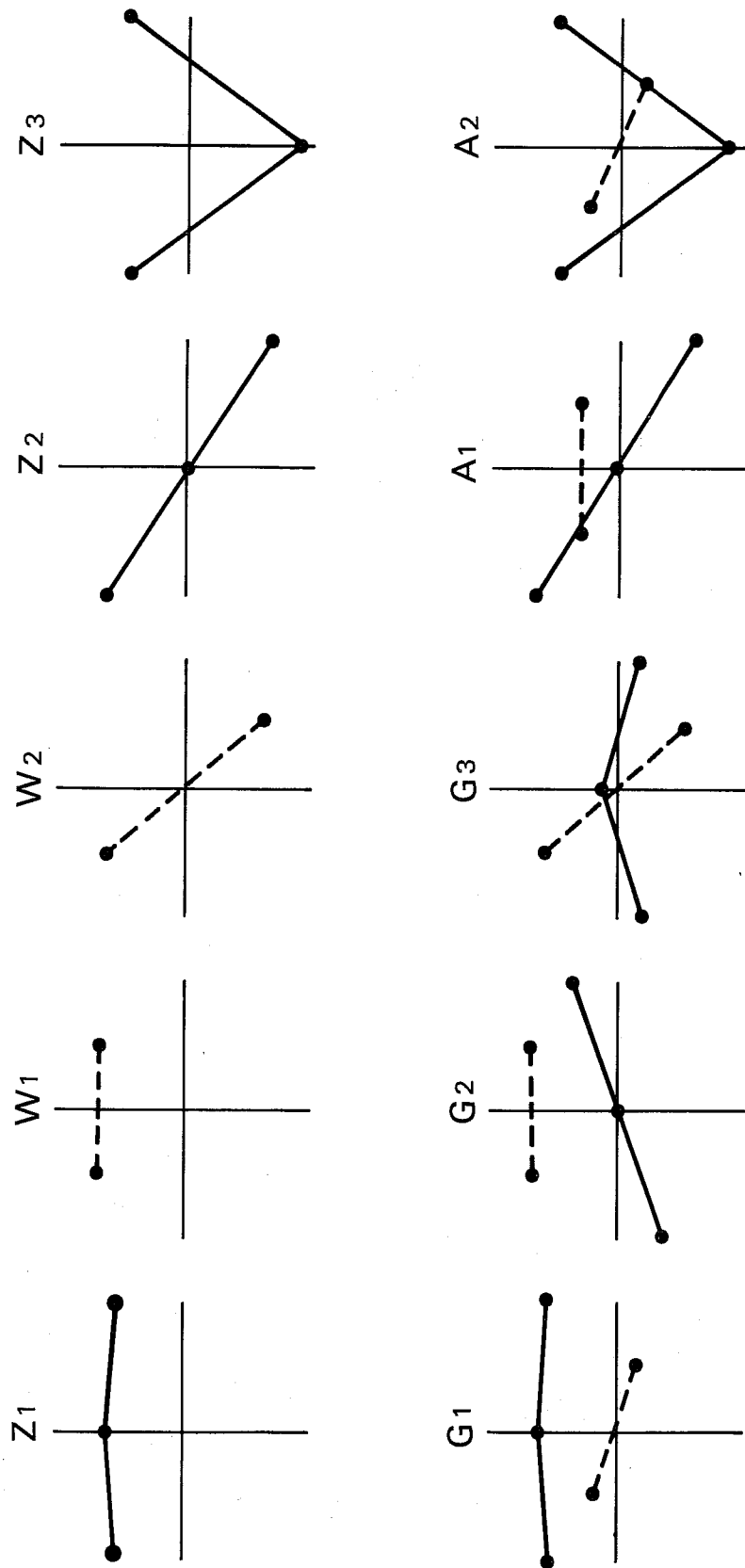
Fig. 12 The 5 eigenvectors for the one-dimensional 5 point network of section 3.2. The dashed lines connect wind points and the solid lines geopotential points. In the top row the case $\mu=0$ is shown and in the bottom row $\mu=1$. The eigenvalues are ordered by decreasing eigenvalues with Z indicating geopotential eigenvector, W - wind, G - geostrophic and A - anti-geostrophic.
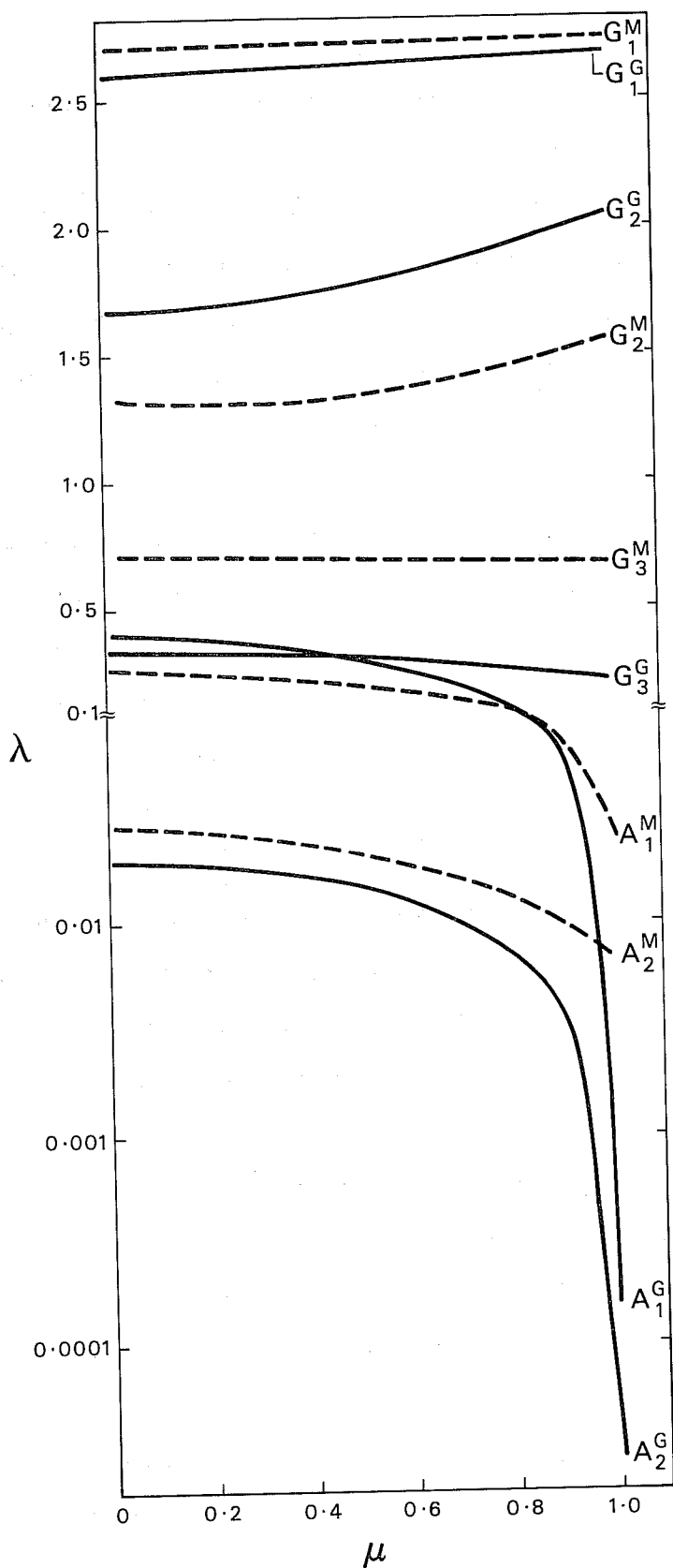
Fig. 13 The eigenvalues for the eigenvectors of Fig. 12 as a function
of μ. G indicates geostrophic, A – anti-geostrophic. Superscript
G indicates Gaussian while superscript M indicates Markov.
The abscissa is μ and the ordinate is the value of the
eigenvalue. Note the break in the ordinate at .1 with a loga-
rithmic scale below.

We show in Fig. 13 the eigenvalues λ_ℓ for these 5 eigenvectors as μ is varied. During this process G_1 degenerates into Z_1, G_2 into W_1 etc. We plot the eigenvalues for two prediction error correlation models (Gaussian - solid curves and Markov - dashed curves). The Gaussian eigenvalues are indicated with a superscript G and the Markov eigenvalues by a superscript M. There is a break in the ordinate at $\lambda = \cdot 1$ with a linear relationship above and a logarithmic relationship below.

Considering first the Gaussian case, we notice that the geostrophic eigenvalues for the modes G_1^G, G_2^G, and G_3^G are much larger than the anti-geostrophic at $\mu = 1$. Thus, the anti-geostrophic eigenvectors will generally be damped by the analysis procedure as we might expect. At $\mu = 0$ the eigenvalues are ordered principally by scale, with the larger scales being more effectively analyzed.

At $\mu = 1$ the anti-geostrophic eigenvalues are extremely small, but increase very rapidly as μ is decreased, effectively asymptoting at $\mu = \cdot 8$. This result is consistent with the results of the last section which showed that most of the variation in the analysis weights occurred between $1 \leq \mu \leq \cdot 8$.

Considering the large-scale geostrophic modes G_1^G and G_2^G we see that the eigenvalues increase as μ is increased. This implies that a given geopotential structure will be better analyzed if (1) $\mu=1$ and (2) there are supporting wind observations which are geostrophically consistent.

Experiments with the Markov model (dashed lines) indicate quite different results. In particular, for $\mu = 1$, the anti-geostrophic modes have much larger eigenvalues than for the Gaussian model, indicating that these eigenstructures are not as effectively suppressed. This is not surprising considering the relatively weak $<u-z>$ and $<y-z>$ correlations shown in Fig. 2.

One question that might be raised by the results plotted in Fig. 13 is: why are the eigenvalues for the anti-geostrophic mode A_1 and A_2 not equal to zero at $\mu = 1$? After all, we can write equation (7) as

$$r_k = h_k^T W_k$$

where the W_k have been determined by the OI procedure, and the h_k^T (at $\mu = 1$) are in exact analytical geostrophic balance. Thus, the resulting analysis (within an analysis box) should be in exact geostrophic balance and there should be no anti- geostrophic flow. The answer to this apparent discrepancy lies in the fact that in equation (18) we have produced the analysis on a discrete set of points. (This discrete set of analysis points happens to coincide with the observation points, but this is not relevent to the present argument). Because the geostrophic relationship implied by both Gaussian and Markov models is analytic, it is not consistent with any discretization procedure applied on the analysis grid. We can demonstrate this simply by replacing the Gaussian model with its discrete finite difference analogue using second order finite differencing.

The $<z-v>$ correlation becomes

$$e^{-\cdot 5\alpha^2} \quad \frac{\sinh \alpha x}{\alpha} \quad e^{-\cdot 5x^2} \tag{20}$$

and the $<v-v>$ correlation becomes

$$\frac{e^{-\alpha^2}}{\alpha^2} \left[\sinh \alpha^2 \cosh^2 \alpha x - \cosh \alpha^2 \sinh^2 \alpha x \right] e^{-\cdot 5x^2}$$

where $\alpha = \Delta x / \alpha$.

As $\alpha \to 0$ the operators degenerate to the normal analytical form.

$$< z\text{-}v >^2 = - x\ e^{-.5x^2}$$

$$< v\text{-}v > = (1 - x^2)\ e^{-.5\ x^2}$$

If we find the eigenstructure using the prediction error correlations of equation (20) we find that there are only 3 non-zero eigenvalues, those corresponding to the 3 geostrophic eigenmodes G_1, G_2, and G_3.

The results of Fig. 13 spotlight a fundamental conflict in multi-variate optimal interpolation. If we desire to suppress ageostrophic flow then some of the eigenvalues of equation (19) must be small and positive. At the same time, there is difficulty in inverting the matrix $P + E$ if there is a great range in the eigenvalues of P. It is for the latter reason that E has to be occasionally augmented to make $P + E$ more diagonally dominant.

We will next use the eigenvector decomposition technique to investigate the non-divergence constraint. In this case, it is appropriate to work in two-dimensions (although the one-dimensional case can be analyzed, the results do not bear much resemblance to the much more important two-dimensional case.) We define an observation network consisting of an equilateral triangle of 3 points with an observation spacing Δx. At each of the 3 points there are u and v components of the wind. We will set $\mu = 0$, so that z does not enter into the problem. The characteristic scale of the prediction error correlation is defined to be b.

We show in Fig. 14 the 6 eigenvectors of the system for $\Delta x/b = .5$. Eigenvectors 1 and 2 define the u and v means, 3 and 4 represent deformation structures, 5 is a rotational eigenvector and 6 is a divergent mode.
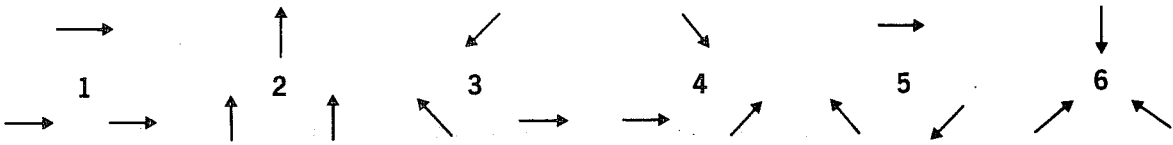
34

Fig. 14 The 6 eigenvectors for the two-dimensional wind only case. The eigenvectors are plotted at $\nu=0$, $\Delta x/b = .5$ by decreasing eigenvalue.
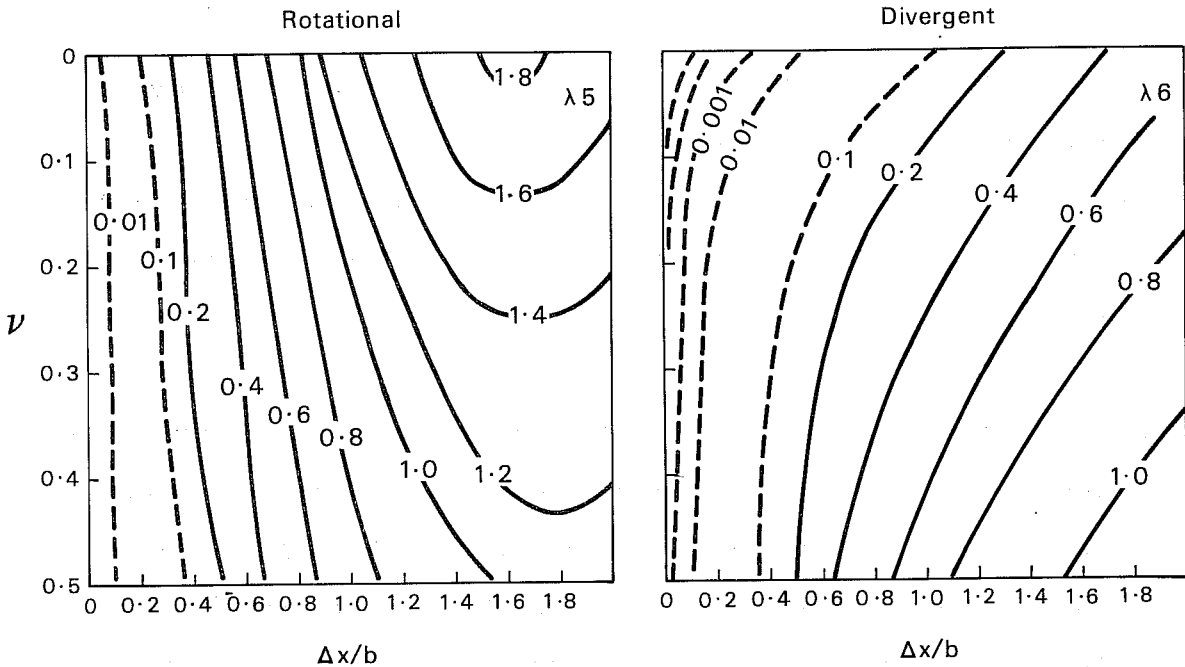

Fig. 15 The eigenvalues corresponding to the eigenvectors of Fig. 14 as a function of ν (ordinate) and $\Delta x/b$ (abscissa) for the rotational (left $-\lambda_5$) and divergent (right $-\lambda_6$) eigenvectors for the Gaussian case. The contour interval is .2, except logarithmic for values less than .1.
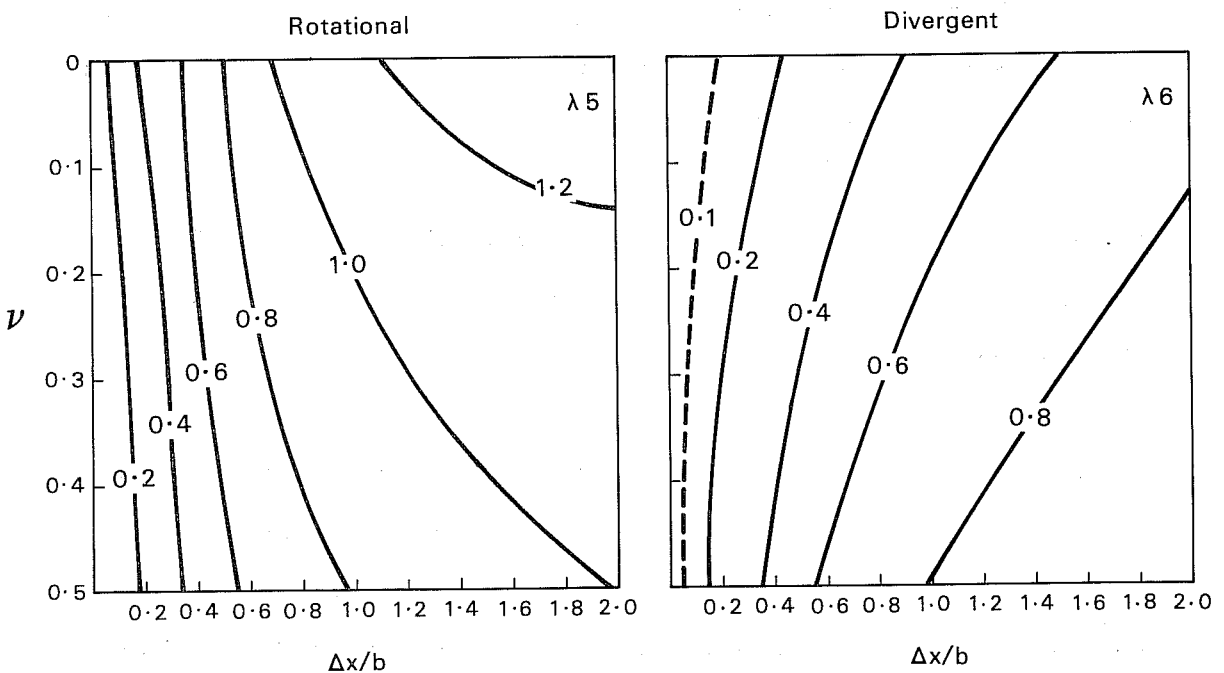

Fig. 16 Same as Fig. 15, except for the Markov case.

35

Eigenvectors 5 and 6 are invariant under variation of ν and $\Delta x/b$, the other 4 eigenvectors are not. Consequently, we will concentrate our attention on the invariant eigenvectors 5 and 6.

We show in Fig. 15 the eigenvalues λ_5 and λ_6 (rotational and divergent eigenvalues) for the Gaussian model as a function of $\Delta x/b$(abscissa) and ν (ordinate). Isopleths of constant λ are plotted generally with a contour interval of 0.2. For very small values of λ logarithmic contours are drawn.

At very small $\Delta x/b$ both λ_5 and λ_6 are small because for this very close observation spacing (or large b) the mean eigenvalues (1 and 2) are dominant. Recall that the sum of the eigenvalues is invariant. At very large values of $\Delta x/b$ all eigenvalues tend to 1. The results at large $\Delta x/b$ become difficult to interpret for the reasons given at the end of the previous section.

In general λ_6 is much smaller than λ_5 at $\nu = 0$, but they become equal at $\nu = \cdot 5$. The largest variation in λ_6 is between $\nu=0$ and $\nu =\cdot 1$, which is consistent with the results of the last section concerning the variation of the analysis weights with ν .

In Fig. 16 we plot the results for the Markov model in the same format as Fig. 15. The relative lack of sensitivity of the Markov model to variation of $\Delta x/b$ and ν is evident.

We complete this section with a brief examination of a more complex case. We consider the two-dimensional array consisting of 9 geopotential observations and 4 wind observations on an Arakawa B-grid (Mesinger and Arakawa, 1976). The u and v wind components are collocated at positions equidistant from the

4 nearest geopotential points. There are $9 + 2 \times 4 = 17$ degrees of freedom and thus 17 eigenvectors. We will consider a Gaussian model with $b_\chi = b$ and $\Delta x/b = .5$. We show 3 examples $\nu = 0, \mu = 1.$ - Fig. 17, $\nu = 0., \mu = 0.$ - Fig. 18 and $\nu = .1, \mu = 0$ - Fig. 19.

We show the 17 eigenvectors starting at the upper left hand corner and proceeding downward and to the right by decreasing eigenvalue. Above each eigenvector is shown the corresponding eigenvalue. All eigenvectors (except the first) have been normalized so that the absolute value of the largest wind or height value is equal to one. The height contours are .2 with negative values dashed and positive values solid. The winds are indicated by arrows.

There are multiple eigenvalues in all three figures which correspond to a two-fold symmetry. Single eigenvalues have 4-fold symmetry. We consider first the effect of the geostrophic constraint (Figs. 17 and 18). Several of the features noted earlier in this section are also apparent here. The combination of eigenvalues 1 and 6 from Fig. 18 to produce eigenvalue 1 of Fig. 17 increases the eigenvalue and this is true of other large-scale modes. With $\mu = 1.$ there are only 6 eigenvectors (Fig. 18) which have large eigenvalues, the rest are effectively damped.

Comparing Figs. 18 and 19 we see how the eigenvalue of the divergent mode (number 10 in Fig. 18) increases by 2 orders of magnitude as ν is increased to .1.

3.3 Scale decomposition of the analysis error with simple explanation of large-scale deficiencies

One of the aims of the present work is to examine the scale response of the OI method. In this section a technique developed by Seaman (1977) will be used to investigate the scale response of a simple one-dimensional box analysis. The scale response of the two-dimensional multi-box f-plane case will be examined in Sect. 4 using a different technique.
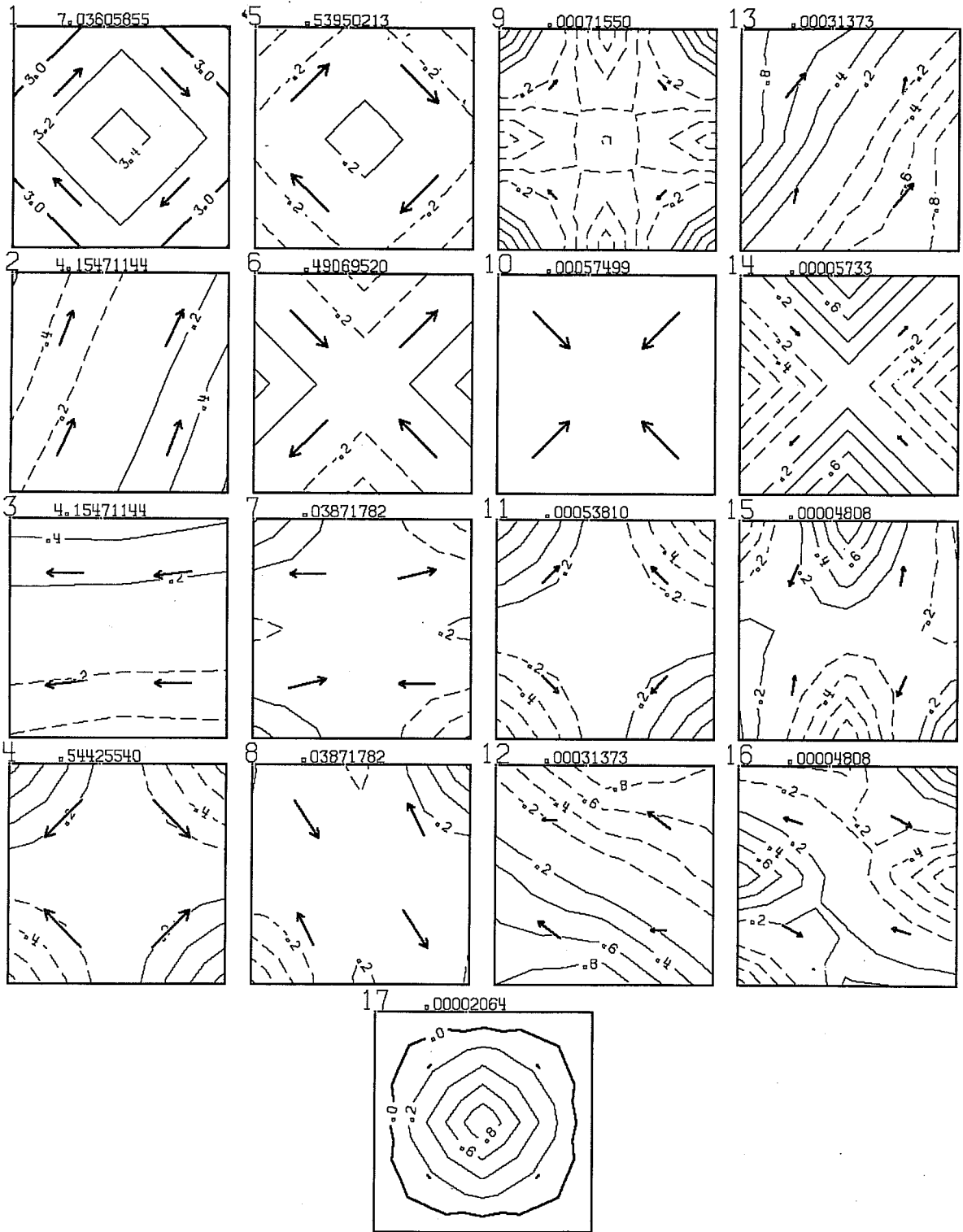
Fig. 17 Eigenvalues of the two-dimensional Arakawa B grid system (17 degrees of
freedom) for the case Δx/b=.5, ν=o, μ=1. The eigenvectors are arranged
by decreasing eigenvalue downward and to the right. The eigenvalue is
listed immedialtely above each eignevector. The height contour internal
is .2, and the wind direction is shown by the arrows.

Fig. 18 Same as Fig. 17, except ν=o, μ=o.

Fig. 19 Same as Fig. 17, except $\nu=.1$, $\mu=$o.

40

Seaman's (1977) technique can be explained as follows. The expected analysis error in a single box analysis at an analysis point k can be calculated using equation (6).

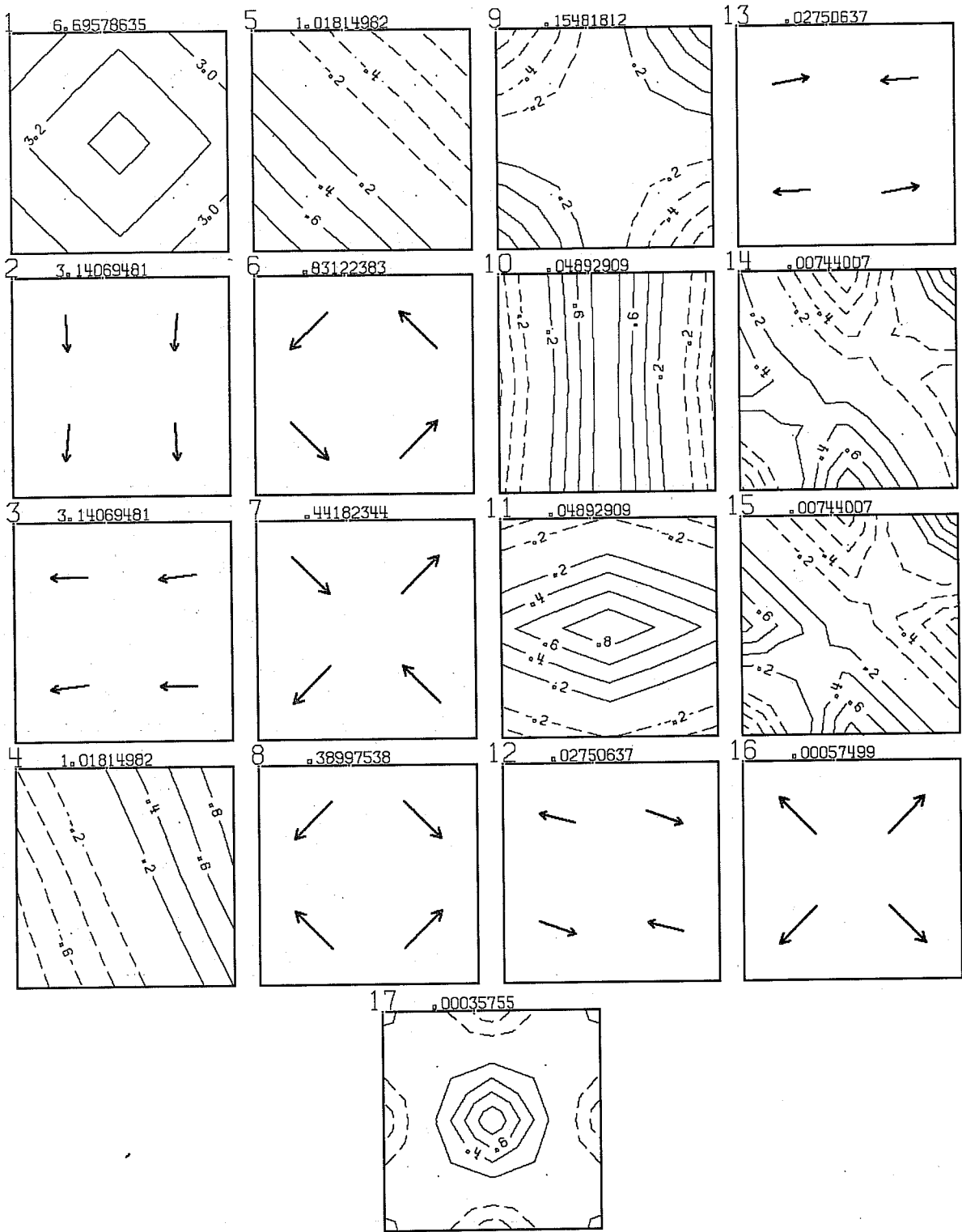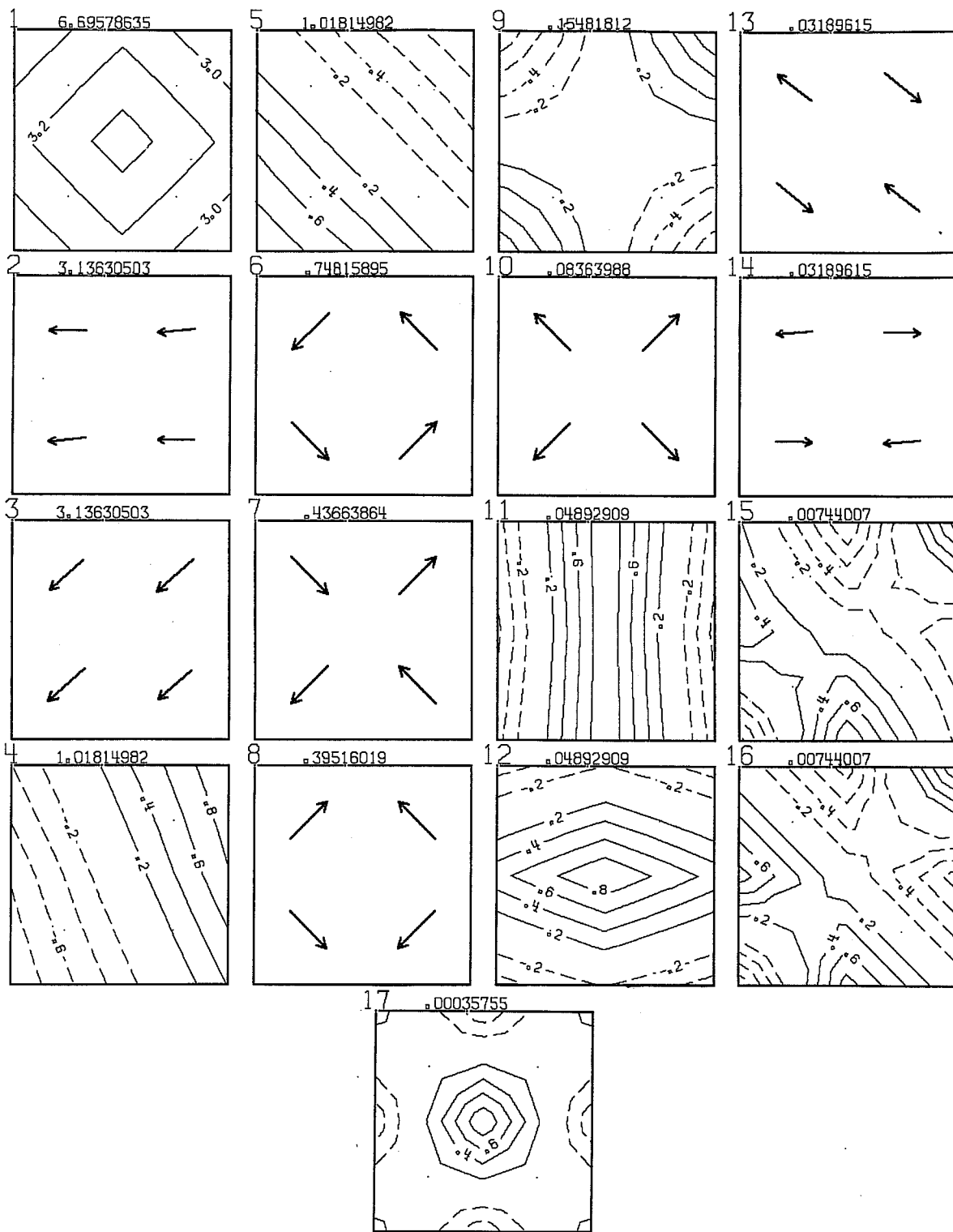$$(\varepsilon_k^a)^2 = 1 - 2\, W_k^T\, h_k + W_k^T\, M\, W_k$$

which is the more general form of equation (8). $(\varepsilon_k^a)^2$ will be a minimum if the W_k are chosen according to equation (7). Suppose, however, that we have a sub-population q^* of the parent population q of observed minus forecast values. We suppose further that the means and variances of the sub-population are the same as those of the parent population $E_p^* = E_p$, $E_o^* = E_o$ etc. This sub-population is assumed to have a different spectral distribution than that of the parent population. We will assume the same prediction error correlation models for the two populations, but the characteristic scale of the sub-population will not equal the characteristic scale of the parent population. Seaman (1977) shows that the expected analysis error in this case is given by

$$(\varepsilon_k^{a\,*})^2 = 1 - 2\, W_k^T\, h_k^* + W_k^T\, M^*\, W_k \tag{21}$$

where W_k are derived by equation (7) for the parent population and the h_k^* and M^* are derived by equation (6) for the sub-population.

We will use this technique to examine the expected analysis error for a population of observed minus forecast increments which is different from that assumed in the specified prediction error correlations. In particular, we shall be interested in the case where the population of observed minus forecast increments has a larger scale than that assumed.

We have calculated $(\varepsilon_k^{a*})^2$ for a simple one-dimensional analysis box as a

function of observation density and sub-population characteristic scale. We

assume the characteristic scale b of the parent population to be 600 km and

define sub-population scales ranging from 300 km to 20,000 km. We fix these

numbers for the sake of concreteness, but they can all be scaled by b. We

define a 7 point one-dimensional observation network with equal spacing Δx .

z and v are collocated at every point of the observation network. We then

vary the observation spacing between Δx =200 km and Δx =4000 km. We

calculate the expected analysis error $(\varepsilon_k^{a*})^2$ at each point k of the

observation network. We assume the same observation error as in section a –

$\varepsilon_o^2 = .25.$ We assume a Gaussian prediction error correlation model with

$\nu = 0$ and $\mu = 1.$

In Fig. 20 we show the expected analysis error averaged over the 7

points of the observational network as a function of sub- population

characteristic scale (abscissa) and network spacing(ordinate). Four cases

are shown. The left hand column is the calculation of z and v analyses from

geopotential observations only; the right hand column is the calculation of z

and v analyses from wind (v) observations only; $(\varepsilon_k^{a*})^2 \geq 1.$ indicates a

worthless analysis.

The optimal interpolation method produces a minimum in analysis error

integrated over all scales and for many realizations provided that the

spectral distribution of the observed minus predicted is the same as that

assumed in the correlation model. The OI method will not necessarily produce

a minimum analysis error in any particular scale, although one would expect a

relative minimum in scales of approximately b. In particular, scales which

are much larger or much smaller than b would not necessarily be individually

optimally analyzed. Julian and Thiebaux (1975) have argued that there are

implied spectral windows in the prediction error correlation function caused

by the minimum and maximimum observation spacing with which the correlations
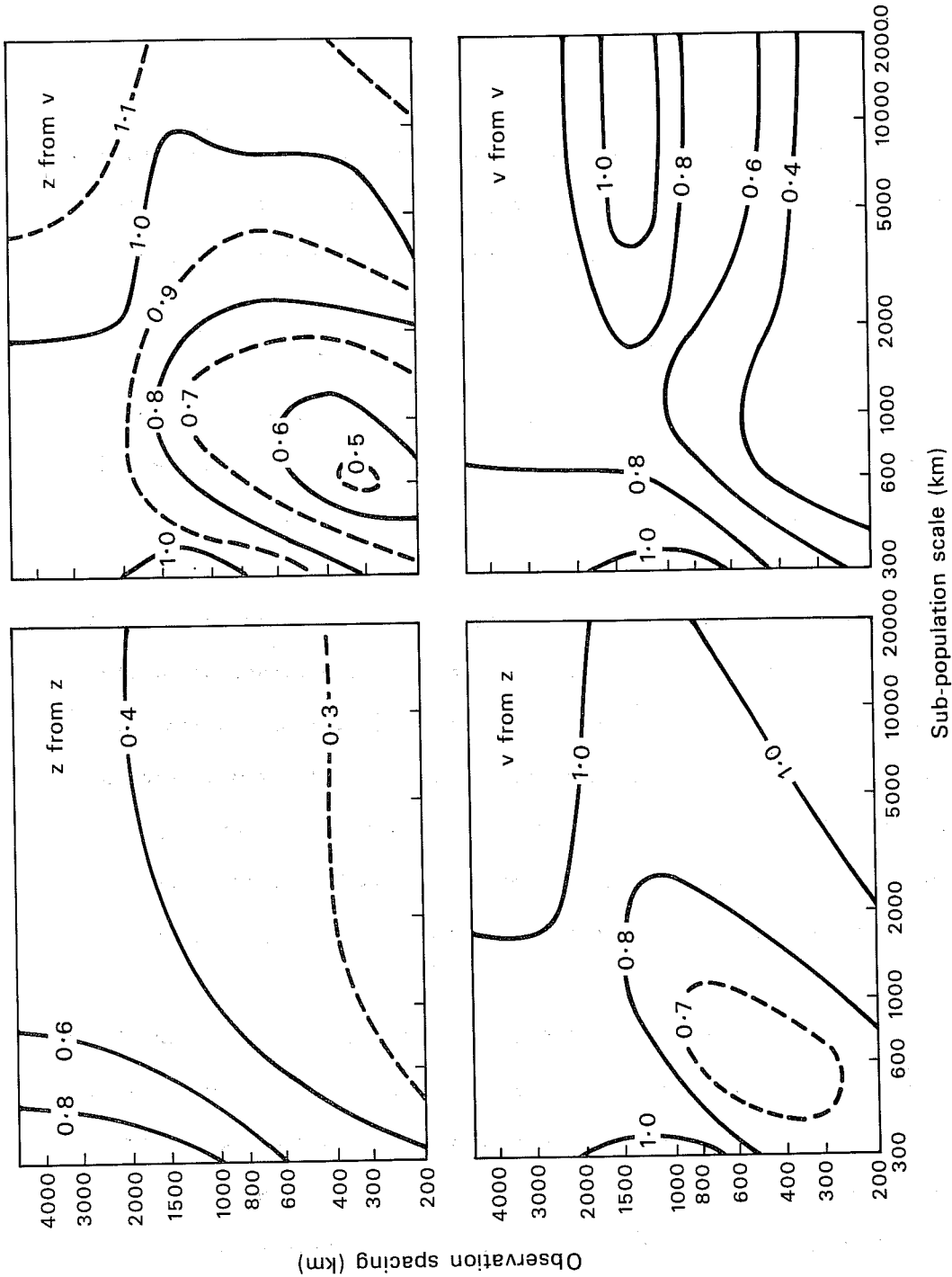
Fig. 20   The expected analysis error obtained by the method of Seaman (1977) for the 7 point observational network of section 3.3. The 4 cases shown are z from z (upper left), z from v – (upper right), v from z – (lower left) and v from v (lower right). The abscissa is sub-population characteristic scale (km) and the ordinate is uniform observation spacing (km).

43

are calculated. Moreover, the planetary scale motion is dominated by the stationary component of the flow and exhibits a marked anisotropy and non-homogeneity (Boer and Shepherd, 1983) which violates the assumptions implicit in Sect. 2.

The problems at small scale, particularly for large observation spacing, are evident in all panels of Fig. 20. This result is as expected, and it is clearly desirable to damp very small scale structures from the analysis in any case.

The large expected analysis error at large-scales (sub-population characteristic scales larger than 2000 km) are not as well-known and we will devote the rest of the sub-section trying to understand them.

Considering first the calculation of geopotential analyses from geopotential observations (z from z), we notice that the large-scale analyses are quite good, but with a tendency to deteriorate at large observation spacing. The calculation of wind analyses from wind only observations (v from v) show a substantially different long-wave problem. Here, there are relatively greater long-wave errors than in the z from z case, with a strong relative maximum error (more than 100%) at an observational spacing (Δx) equal to 2b.

The v from z and z from v plots show different patterns again with very large long-wave errors with a weak minimum at observational spacing at Δx equal to 2b. We will examine the reasons for these long wave errors using a very simple one-dimensional box model. Here, we will assume that we have 9 observations of wind(v) and height (z) collocated and separated by an observational spacing Δx. We will then produce a very high resolution analysis (virtually continuous) from these observations using a one box OI method. We assume a Gaussian prediction error correlation model($\mu=1$ and
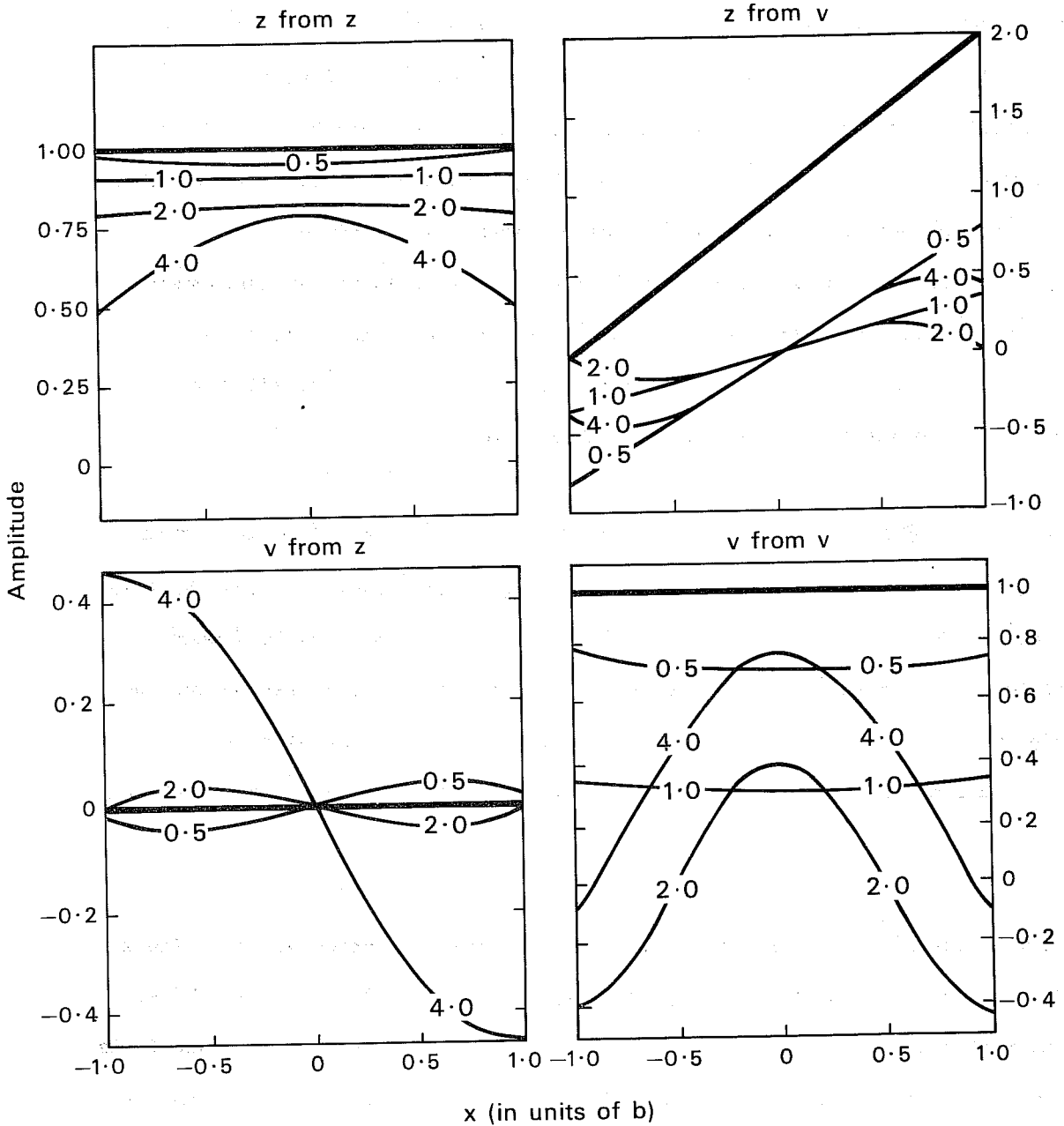
Fig. 21 Continuous analyses produced from a 9 - point one-dimensional uniform
         observation network. The 'truth' is indicated by the heavy solid
         line. The analyses are shown for different values of observation
         spacing Δx - viz Δx = .5b, b, 2b and 4b. The ordinate is amplitude
         and the abscissa is x in units of b. Four cases are shown arranged
         in the same order as in Fig. 20. This case assumes a Gaussian model
         with $\mu = 1$ and $\nu = 0$.

$v = 0$) and an observational error $\varepsilon_o^2 = .25$. We will display the

resulting analyses between $-b$ and $+b$. We will do 4 different cases – z from

z, z from v, v from z, and v from v with different observational spacings

$\Delta x = .5b$, $\Delta x = b$, $\Delta x = 2b$, and $\Delta x = 4b$. We stress again that these are

(virtually) continuous analyses and not simply projections back on the

observation points. We will use a very large-scale observation field. Thus

for the geopotential only observations we assume $z=1$ everywhere; the

appropriate geostrophic winds ($\mu = 1$) in this case would be $v=0$ everywhere.

For wind only observations we assume $v=1$ everywhere; the appropriate

geostrophic height in this case would be $z = 1 + x$. (We have added an

arbitrary constant of integration in this case).

We show in Fig. 21 the resulting analyses in the 4 cases. The solid thick

lines indicate the true solutions; the lighter solid lines show the resulting

analyses for $\Delta x = .5b$, $\Delta x = b$, $\Delta x = 2b$, and $\Delta x = 4b$. Edge effects have been

minimized in these plots because the observational points go far beyond the

edge of the plots – thus, for example, for $\Delta x = .5b$ the most distant

observations are 2b and for $\Delta x = 4b$ the most distant observations are at 16b.

We will examine first the cases with geopotential only observations. The z

from z case shows a reasonably good analysis except at $\Delta x = 4b$ in which case

the analysis goes to $(1 + \varepsilon_o^2)^{-1} = .8$ at the observation point ($x=0$) and falls

off in between. (At the large Δx limit each analysis is produced with one

observation and reflects the shape of the structure functions in between

observations).

Looking at the resulting geostrophic wind (v from z in lower left hand panel)

we see that $x = 4b$ results in a large spurious positive v for positive x and a

large spurious negative v for negative v. In two-dimensions this would be

expressed as a spurious local maximum or minimum of z with a corresponding spurious

geostrophic wind around this geopotential extremum. At the other extreme for

$\Delta x = .5b$ the geopotential analysis is good, but the resulting wind analysis

is in error in the opposite sense. There is a relative minimum in the wind

error at $\Delta x = b$ (obscured by the true solution - heavy solid line in Fig. 21).

Thus, we can see that there is some justification for the relative minimum

in the large-scale wind error in Fig. 20 (lower left hand panel).

We turn now to the wind only observation cases on the right hand side of Fig. 21.

In the z from v case, the OI method is unable to obtain the constant of

integration as noted by Lorenc (1981). In fact the constant of integration

has been set to zero. Also the method does not produce the large-scale geopotential

gradient correctly either. It might be noted in Fig. 20 (upper right hand

corner) that there are some scales where the constant of integration is small

and thus a reasonable analysis of z can be obtained from v.

For the v from v case there is the same fall off between observation points at

$\Delta x = 4b$ as in the z from z case. What is more interesting, though, is the

serious underdrawing of the large-scale windfield for the intermediate

observation spacing $b < \Delta x < 2b$. The reason for this can be seen by examining

Fig. 1 which shows that the <u-u> and <v-v> correlations have large negative

lobes. Thus, for a very large-scale windfield the observations at $x = 2b$

would be negatively weighted in the analysis of v at $x = 0$.

Further light is shed on the v from v large-scale analysis problem in Fig. 22.

There are two v from v cases plotted here, in the same format as Fig. 21.

In both cases the experimental parameters are the same as in Fig. 21 with

the following modifications. In the left hand panel we used 21 observations

instead of 9. The observation spacing is the same as in Fig. 21, but we

search further for them. In the right hand panel we assume 9 observations,

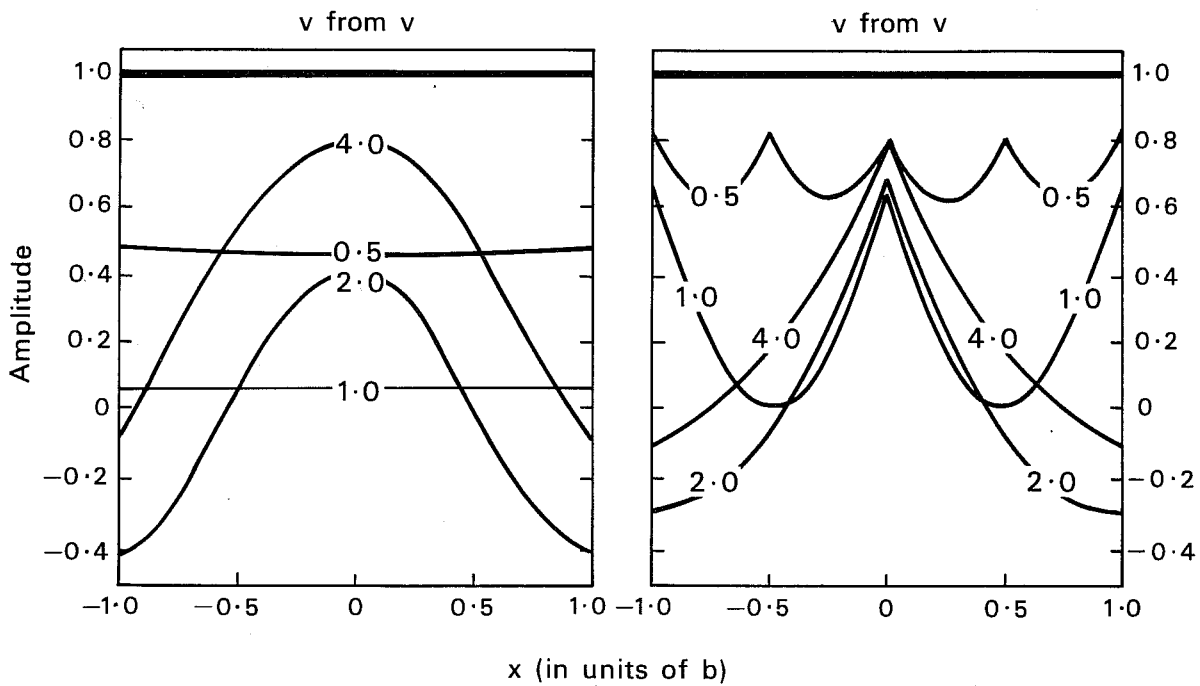but we use the Markov model. The 21 point case demonstrates that the

Fig. 22 Same as Fig. 21 except for the 21 point array (left panel) and Markov function (right panel).

underdrawing gets worse for the large-scale windfield as more observations (further away) are included. Fig. 1 shows that the <u-u> and <v-v> correlations are negative over most of the domain so this result is not surprising (although the effect may be exaggerated in one-dimension).

The Markov model (Fig. 22 - right hand panel) shows quite different results from the Gaussian model. Here, the underdrawing at the observational points is not as severe as in the Gaussian case, but there is a serious underdrawing in between the observation points - in fact the curve represents a series of isolated structure functions. This is presumably because of the weaker negative lobes in Fig. 2 in the u-u and v-v correlations.

This section has uncovered some interesting and largely unknown potential problems in the OI analysis of large-scale waves. The problems of generating large-scale wind analyses from geopotential observations and vice versa are probably merely curiosities because the assumed geostrophic relationship is incorrect for the large-scale flow on the sphere in any case. The problem of underdrawing the large-scale windfield when only wind observations are used is potentially serious in the tropics.

4. TWO-DIMENSIONAL MULTI-BOX ANALYSES ON F-PLANE AND SPHERE

The simple box experiments of Sect.3 have provided a number of useful insights into the internal mechanisms of multi-variate optimal interpolation. We are now ready to relax some of the constraints of Sect.3 and to examine more realistic and complex experimental situations. In particular, we shall now introduce spherical geometry and the multi-box procedure used at the ECMWF. However, we shall still retain other important simplifications : viz, no vertical variations, no data checking, a homogeneous observation network and error free data. In Sect. 4.1 we shall perform multi-variate multi-box experiments on a two-dimensional f-plane. Our particular aim is to obtain a complete two-dimensional scale response for the geopotential, rotational wind

component and divergent wind component. We shall pay particular attention to some of the problems noted in Sect. 3.3 concerning longwave analysis.

In Sect. 4.2 we shall examine the effect of spherical geometry on the analysis scheme. These experiments were inspired by the results of Cats and Wergen (1982) who showed that if the ECMWF analysis system was presented with a single large-scale Rossby or Kelvin wave, there were serious errors in the resulting analysis, even with a homogeneous observation network. Here too, we shall be concerned with the analysis of large-scale Rossby and Kelvin waves, but the emphasis will be strictly horizontal.

4.1 Multi-box analysis on an f-plane.

The box-averaging scheme for producing the final ECMWF analysis from a large number of single box analyses is a unique feature of the ECMWF OI scheme. The box-averaging simply requires that the final analysis at a given point be a weighted linear combination of the local analyses produced in the neighbouring boxes, evaluated at the point. The weights are related to the distance of the analysis point from the box centre (maximum at the box centre and falling linearly to zero at the box boundaries.) From a didactic point of view, this procedure implies that analysis on an infinite plane is a simple extension of the single box results of Sect. 3. Analysis on an infinite plane offers two pedagogical advantages: edge effects are eliminated and a proper divergent response can be obtained.

In this section the basic technique is simply to present the multi-box analysis scheme with a single two-dimensional Fourier component in u,v and/or z and then determine the response of the analysis scheme to this wave. As before, we assume that we are dealing with the observation minus first guess differences. Thus, we have specified a multi-box analysis scheme with the following representative characteristics. The box centres are 660 km apart

50

and each analysis box is 1320 km x 1320 km, so they are overlapping as in the ECMWF scheme. The observational network is specified to have a regular spacing. The characterisic scale b has been chosen to be 600 km, the observation error ratio ε_o^2 = .25 and we have used the Gaussian model. The analysis grid spacing is 200 km.

The results of these experiments are not insensitive to the data selection strategy chosen. The responses could differ between the selection strategy of ECMWF which includes large numbers of observations and the strategy at other centres which includes a small number of highly correlated observations. In order to make the present study as general as possible we have deliberately included large numbers of observations in the hope that they will define some type of asymptotic limit. Thus in each analysis box we search out radially 3.5 times the observation spacing to obtain data. This gives approximately 40 observations of each data type per box (ie. 120 observations if u,v and z observations are used.) Thus the present experiment uses approximately the same number of observations as the ECMWF system (although the ECMWF system searches vertically as well, so that the horizontal search would be more confined than in the present experiment).

The experimental parameters which we vary in these investigations are ν, μ, b_χ, the observation spacing Δx and the scale of the two-dimensional Fourier component. The input winds and heights have an x scale ℓ_x and a y scale ℓ_y. We will relate the quarter wavelength of these waves to the circumference of the earth (40000 km). For example, a wave with a quarter wavelength of 10000 km would be wavenumber 1. In most experiments we will assume $\ell_x = \ell_y$.

A typical experiment is shown in Fig. 23. Here the input is wavenumber 20 ($\ell_x = \ell_y = 20$). The observation spacing $\Delta x = 800$ km, $\nu = 0$ and $\mu = 1$. The input or truth is shown on the botton panel (height on left, winds on the right). The

51

Height analysis   Wind analysis

Height observations only   Wind observations only

Height and wind observations

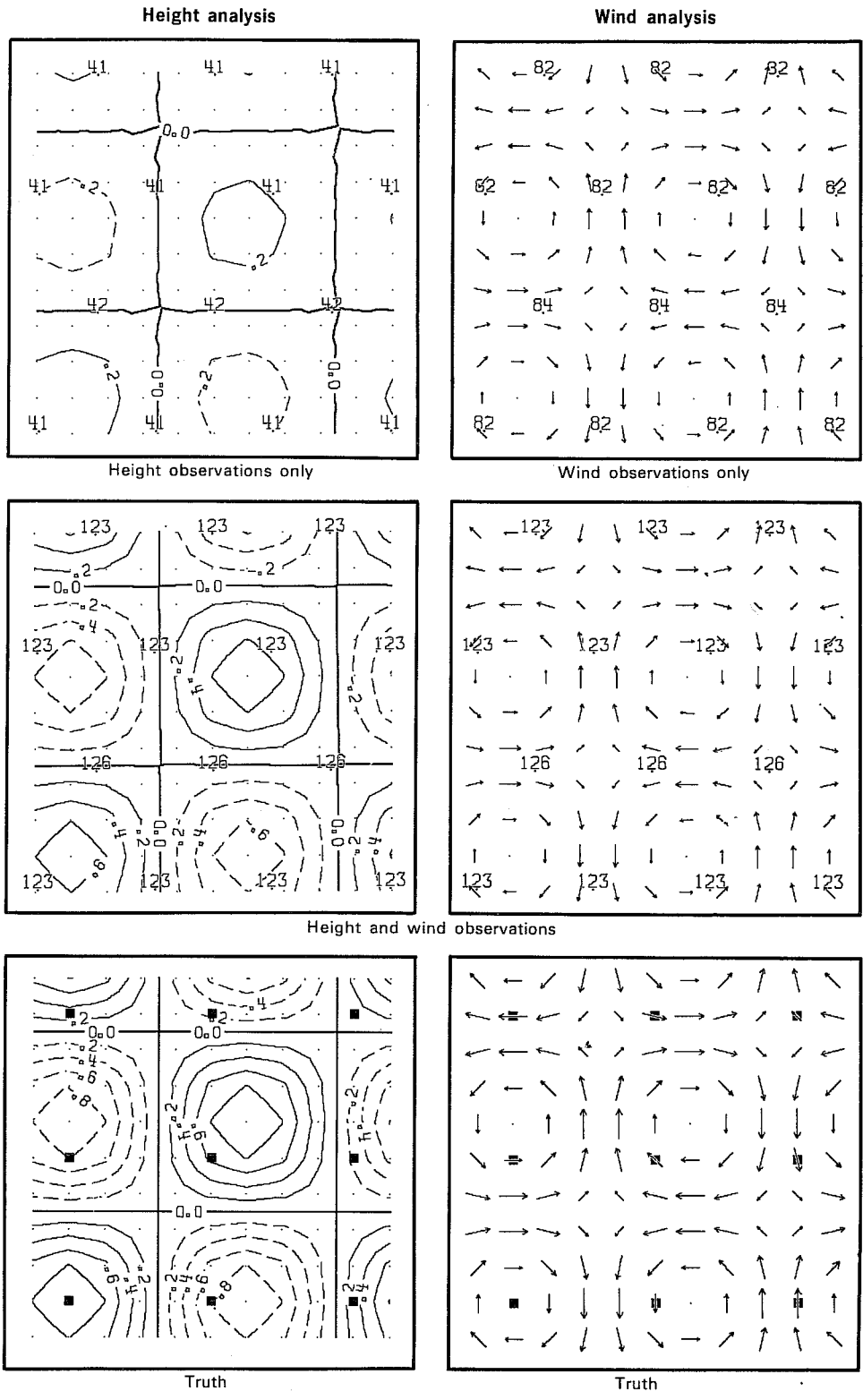Truth   Truth

Fig. 23 A typical multi-box f - plane experiment - height is on
         the left, winds on the right. Box centers are shown by
         the location of the numbers, with the numerical value
         indicating the number of observations used in that box.
         In this experiment the input is wavenumber 20 with
         heights and winds geostrophically related and the uni-
         form observational spacing is 800 km. The bottom panel
         is the 'truth', the middle panel is the analysis with
         wind or height observations only and the top panel is
         the analysis with both wind and height observations. The
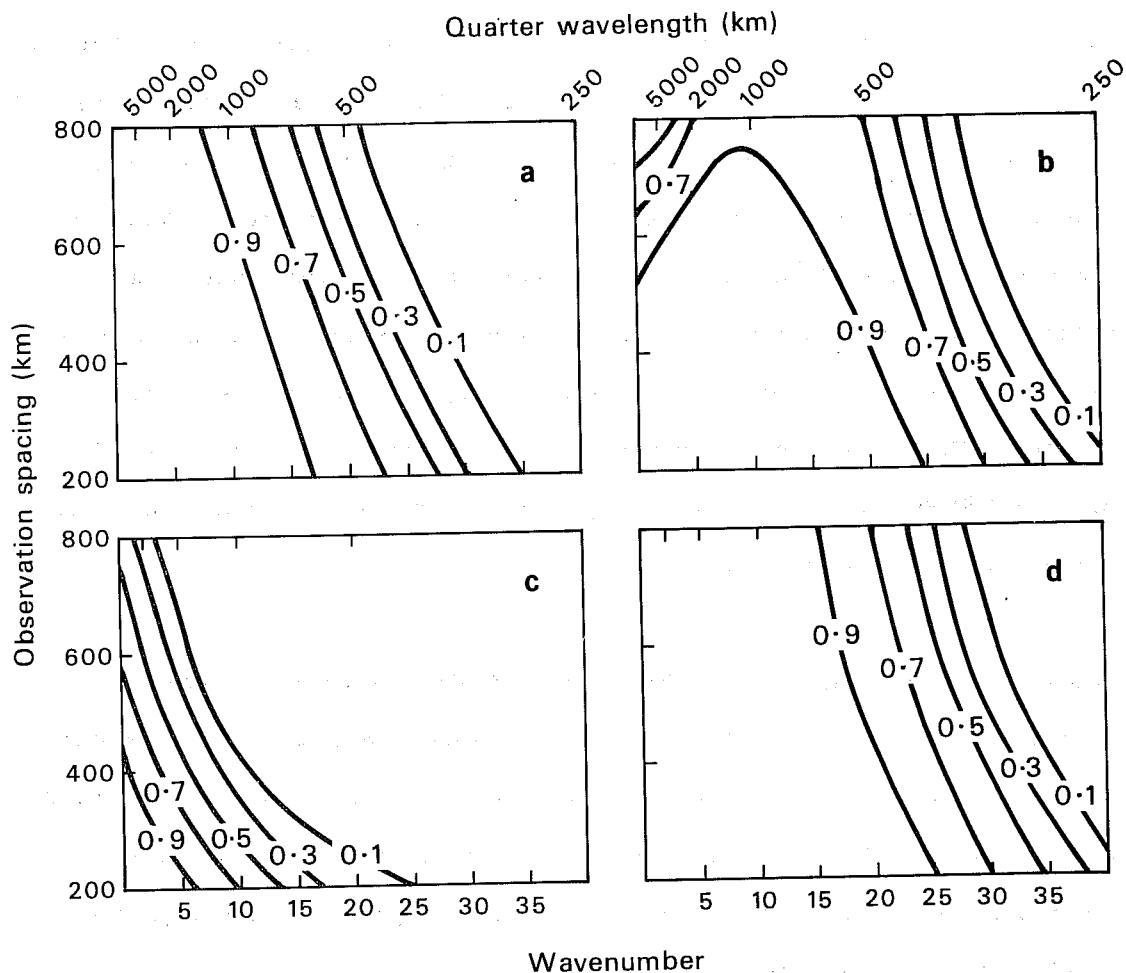   small black squares indicate the observation points.

52

Fig. 24 Summary of the results of all experiments of the type illustrated in Fig. 23. These are response diagrams as a function of input wavenumber (abscissa) and observation spacing (ordinate). On the top of each diagram is also shown the quarter wavelength (km). (a) geopotential response to geopotential observations, (b) wind response to non-divergent wind observations, (c) wind response to irrotational wind observations, (d) the response of height or wind to geostrophically consistent winds and heights. The experiments are for $\mu=1$, $\nu=o$

53

inputs are exactly geostrophically coupled, so there is no divergent flow. The observation positions are indicated by the small black squares on the bottom panel - they are exactly collocated. The height variation is from -1 to +1 with contour interval .2 and all wind analyses can be strictly compared to the wind input. In the top and middle panels of Fig. 23 we show the resulting analyses of height (left side) and winds (right side). The large numbers in these analyses indicate the position of the box centres and the values indicate the number of observations used in that particular box. This plot shows only a sub-section of a larger plot, so that no edge effects are visible. The analysis of the top panel uses height observations only (left side) and wind observations only (right side). The middle panel uses both height and wind observations.

Examining the responses of height and wind fields we see that the wind response is about .7 in both cases. On the other hand, the height response is about .2 with only height observations, but .7 with the addition of wind observations. This result confirms one of the conclusions drawn in Sect. 3 section b, namely that when $\mu = 1$ and there is a supporting geostrophically consistent wind, the height will be better analyzed.

The results with many input scales are summarized in the response diagrams of Fig. 24. Here we plot isopleths of response (.9, .7, .5, .3, .1) as a function of observation spacing (abscissa) and input scale (ordinate). We indicate abscissa values in both wavenumber and quarter wavelength. All parameters describing the analysis scheme are as described above. Responses less than .3 are hard to determine, for there may be spurious components of different character or scale in the analysis.

In Fig. 24a we show the geopotential response to geopotential observations only; in 24b the wind response to non-divergent wind observations only; in
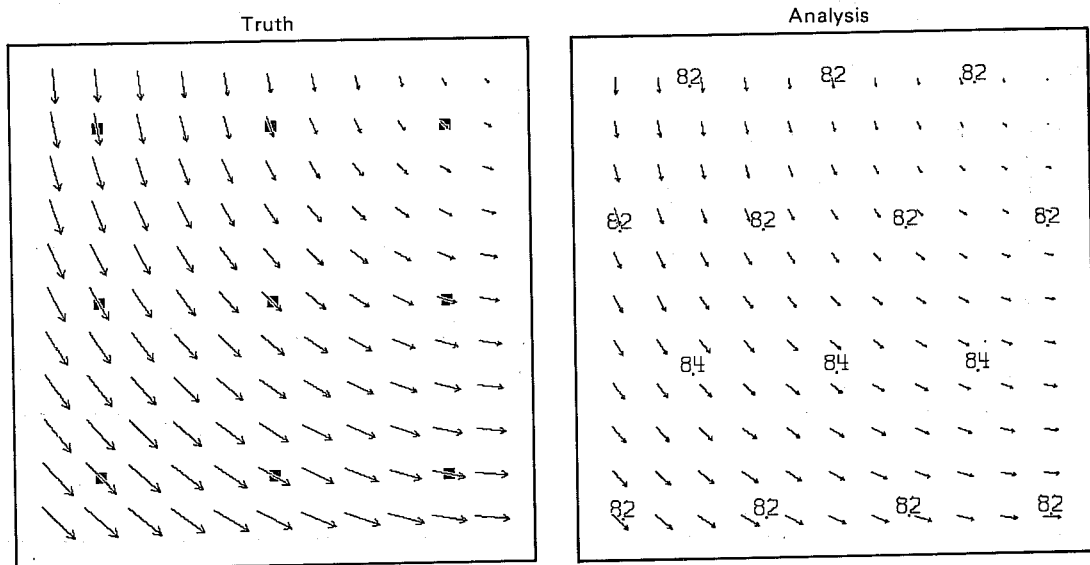
Fig. 25   An example of under-drawing the large-scale windfield. The input
          windfield observations are wavenumber 1 – non-divergent and the
          uniform observation spacing is 800 km.
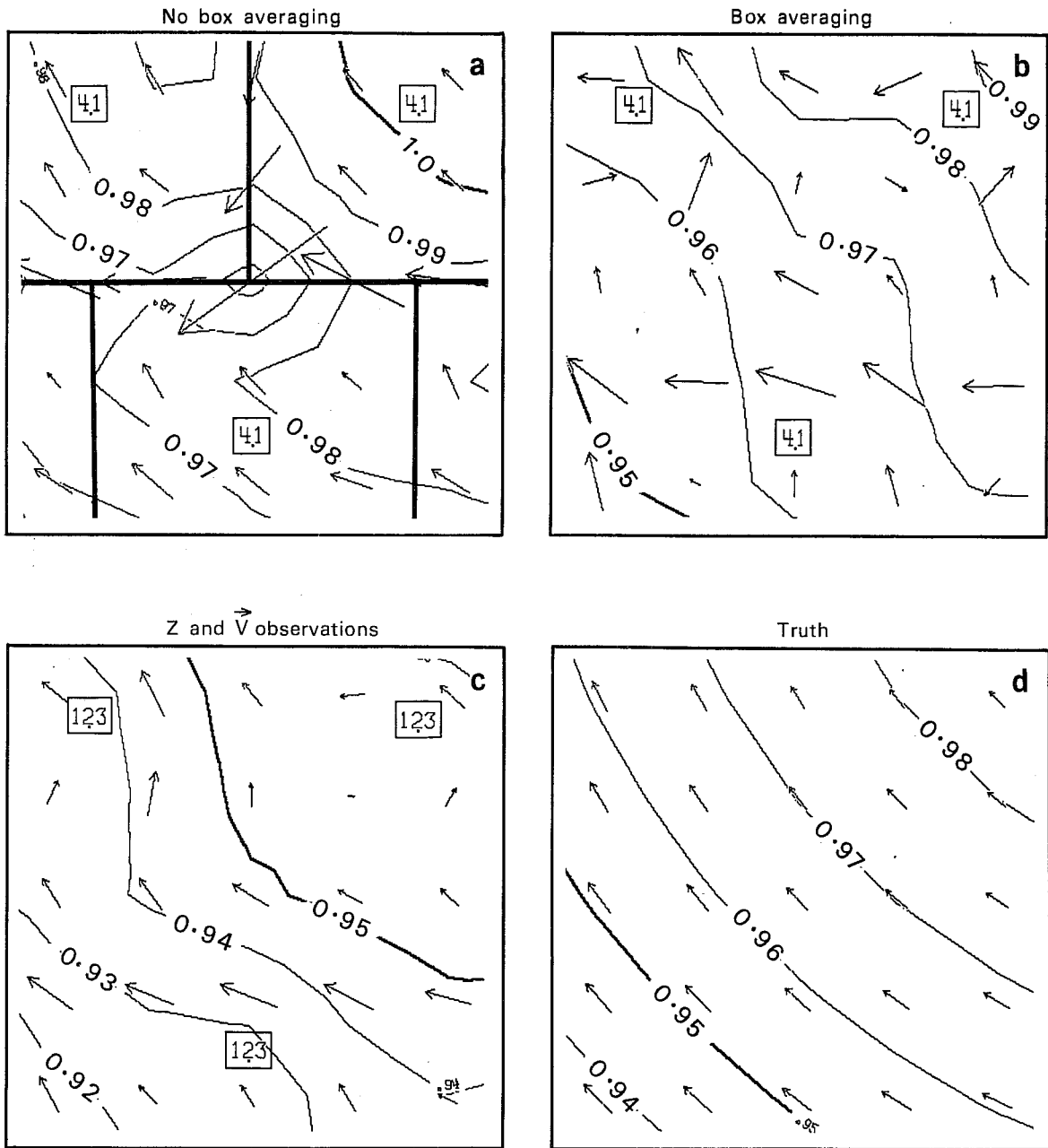
Z observations only

Fig. 26 An example of problems with the geostrophic coupling in large-scale flow. The boxed numbers indicate the box centers and the number of observations used in that particular analysis box. The height contour interval is .01.(a)(b)(c) are analyses while (d) is the 'truth'.(a)and (b) have height observations only,(c)has both wind and height observations.

24c the wind response to irrotational wind observations only; and in 24d the response of either wind or height (they are the same) to geostrophically consistent wind and height observations.

Examining 24a, b and d we note that small-scale wind fields can be analyzed better than small-scale height fields, which might be expected from an examination of the structure functions of Fig. 1. The problem with under-analysis of the large-scale windfield shows up in the upper left hand corner of Fig. 24b. We note that 24d shows how the addition of geostrophically consistent wind observations assists the analysis of the multi-scale height field. As indicated earlier, most of the results were obtained with $\ell_x = \ell_y$. We did a few runs with different aspect ratios, however, and did not find much sensitivity.

In Fig. 25, we demonstrate the under-drawing of the large-scale windfield that appears in Fig. 24b. This is a wavenumber 1 case with truth on the left and analysis on the right. The observation points ($\Delta x = 800$ km) and box centres are indicated as before. The extensive underdrawing shows up clearly.

In Fig. 26 we examine the problem with large-scale height and wind analyses indicated in the lower left hand corner of Fig. 24d. This is a blow-up of one section of the analysis. The observation spacing is 200 km, $\mu=1$, and the box centres are indicated by numbers as before. The height contour interval is .01. This is a wavenumber 1 case with the geostrophically consistent truth in the lower right hand corner (26d). The observation positions are indicated by the position of the wind arrows in Fig. 26d. In this case the observation network and analysis grid coincide.

Wind analysis (ν=0)

Wind analysis (ν=0.10)

Truth

Fig. 27 Same as Fig. 25 except for irrotational wind input of wavenumber
         15. The 'truth' and analyses for ν=0 and ν=1 are shown.
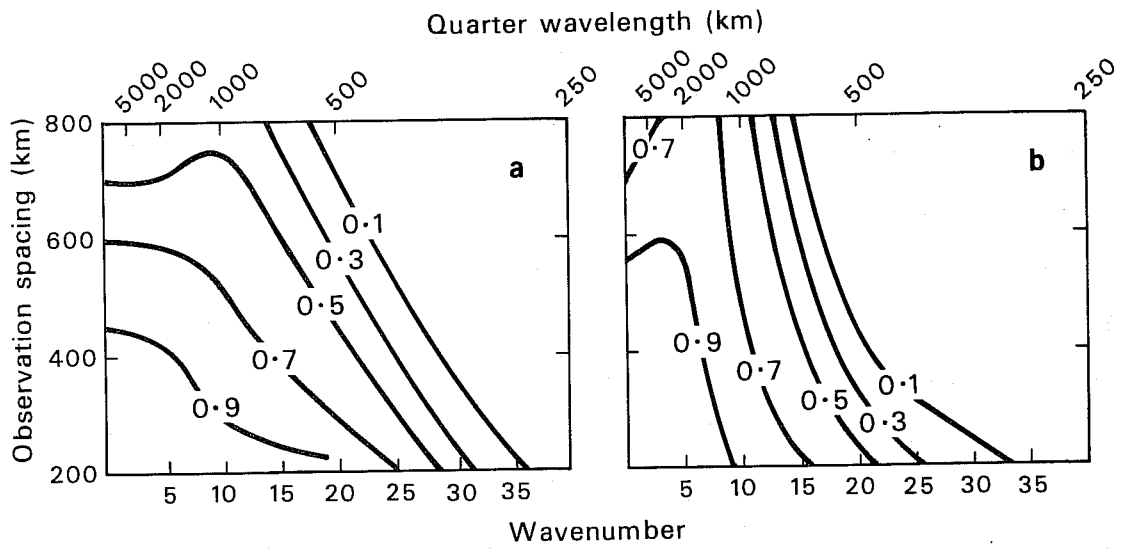
Fig. 28   Response curves in the same format as Fig. 24 for irrotational wind
input for two cases - left $\nu=.1$, $b_\chi=b$ and right $\nu=.1$, $b_\chi=2b$.

In Fig. 26 a, b, c we show the resulting analyses in 3 cases. In Fig. 26a and

b we show the analyses of height and wind when only height observations

are used. Fig. 26b shows the resulting normal analysis and it is obvious

that it is not at all geostrophically consistent. In Fig. 26a we show the

same analysis without box-averaging (the analysis box boundaries are shown by

straight black lines). In Fig. 26a the analyses are geostrophic within the

boxes (as they must be when $\mu = 1$). It is the box averaging which produces

the non-geostrophic effects. This effect occurs, as has been noted

previously by others (Cats, G. - personal communication), because the

lateral variation of the box-averaging weights is not considered in

calculating the geostrophic winds. In Fig. 23d we show that the addition

of wind observations assists the problem, but does not cure it. We stress

that this pathological example is not as worrying as it might seem. Firstly,

the geostrophic relationship is not really valid on these scales anyway.

Secondly, it requires a very weak height gradient compared to the absolute

magnitude of the height, and thus the geostrophic winds are very weak in any

case.

We turn now to consideration of the divergent wind. We show in Fig. 27 an

example of analysis of a divergent windfield. The truth is on the bottom and

two resulting analyses are above. At the top is the case $\nu = 0$ and in

the centre $\nu = .1$. In this case $b_\chi = b$ and all other experimental parameters

are as before. The input is wavenumber 15 and the observation spacing is

600 km. The observation positions and box centres are indicated as before.

We see that for this example, $\nu = 0$ virtually suppresses the divergent

motion, whereas $\nu = .1$ gives a response of about .5.

The divergent response for the case $\nu = 0$ are shown in Fig. 24c. The

complete suppression of the divergent wind (compared to the rotational)

except at very large-scales and dense observation networks is evident. In

Fig. 28 we show the divergent responses in the case $\nu = .1$, $b_\chi = b$ (Fig. 28a)
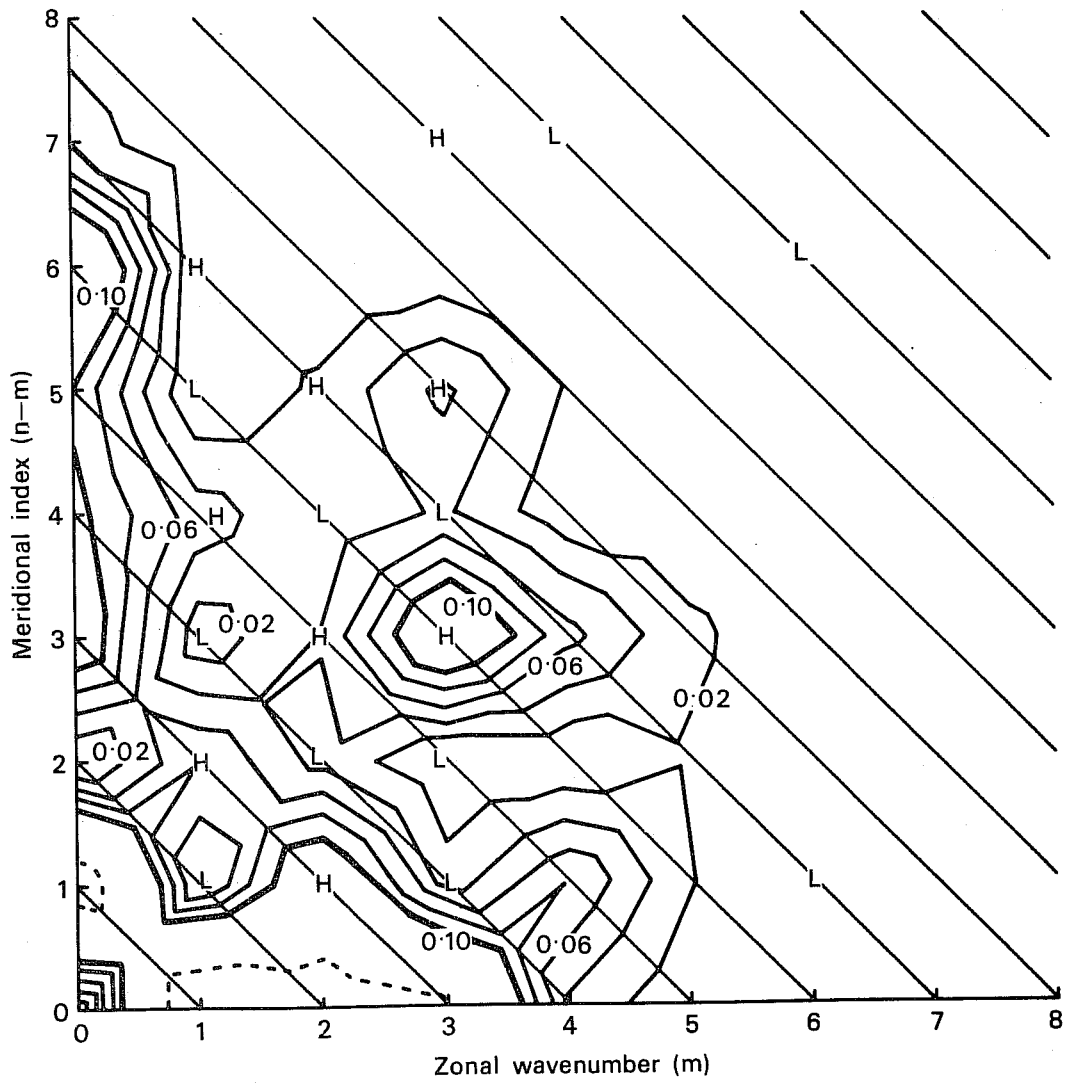
Fig. 29   Spherical harmonic spectrum of the kinetic energy of the 200 mb
divergent wind for January 1979 (reproduced from Hollingsworth and
Cats - 1981).

and $\nu = .1$, $b_\chi = 2b$ (Fig. 28b). The much stronger response in the shorter waves is evident in Fig. 28a. It is probably undesirable to have too strong a divergent response in the short waves, so there is good reason to make b_χ larger than b. The choice of $b_\chi = 2b$ reduces the response for the short waves (except when the data density is high), but increases the response in the long waves for low data density. It might be noted in passing that the change of b_χ and ν does not change the response to the rotational wind except for an improvement in the longwave, low data density case. This is because, for a single analysis box, longwave rotational and divergent flows are indistinguishable.

Our response curves for the divergent flow in the case $\nu = 0.$ (Fig. 24c) is consistent with the spectrum of analyzed divergence obtained from the FGGE data set using the ECMWF system. We reproduce in Fig. 29 a plot of the spherical harmonic spectrum of the kinetic energy of the 200 mb divergent wind for Janauary, 1979. This plot was originally due to Kanamitsu and was presented in Hollingswoth and Cats (1981). It demonstrates that there is really very little analyzed divergent kinetic energy in wavenumbers higher than 6. Now, these FGGE analyses are produced from a linear combination of first guesses and analysis increments. Our Fig. 24c demonstrates that the ECMWF analysis system (with $\nu = 0.$) underestimates the divergent winds on the shorter scales, which is consistent with Fig. 29. The lack of divergent kinetic energy in the first-guess field is explained by the damping effect of the full field interpolation plus adiabatic initilization.

4.2 Analysis of planetary scale modes in pseudo-spherical geometry

Cats and Wergen (1982) determined the response to the full ECMWF analysis system to the input of planetary scale modes. They specified an analytical "observed minus forecast field" which they then sampled on a homogeneous 7.5 degree observation network. The specified input consisted of individual

normal modes of the ECMWF gridpoint prediction model. These normal modes were then analyzed using the full ECMWF system. The resulting analyses could then be back-projected onto the normal modes and the response of the input mode and the aliasing onto other modes could be determined.

Cats and Wergen (1982) presented the full ECMWF analysis system with various large-scale Rossby and Kelvin modes of different equivalent depths and zonal and meridional scales. They concluded that the mid and high latitude analyses of these modes were acceptable, but that the tropical analyses were poor. Consequently, the modes, particularly the Rossby and Kelvin waves, tended to alias substantially in the analysis. Part of the problem, at least, they attributed to difficulties with the vertical prediction error correlations, but there were probably horizontal effects as well.

Inspired by the results of Cats and Wergen (1982) and the conclusions of Sect. 4.1, we decided to examine the horizontal aspects of the planetary scale analysis problem. This could be done using a fairly straightforward extension of the f-plane code developed in the preceeding section.

We decided not to use true spherical geometry because of the many complexities in the vicinities of the poles. Instead we decided to limit our analysis to the region 60 degrees north to 60 degrees south and to make the following modification to the coordinate system to partially account for the convergence of the meridians. We relate our usual x,y coordinates to the pseudo-spherical latitude (θ) and longitude(λ) in the following way.

$$y = s\,\theta \qquad x = s\lambda \cos\theta$$

(22)

$$v = s\,\dot{\theta} \qquad u = s\left[\cos\theta\,\dot{\lambda} - \lambda\,\dot{\theta}\,\sin\theta\right]$$

where $s = 110$ km/degree

63

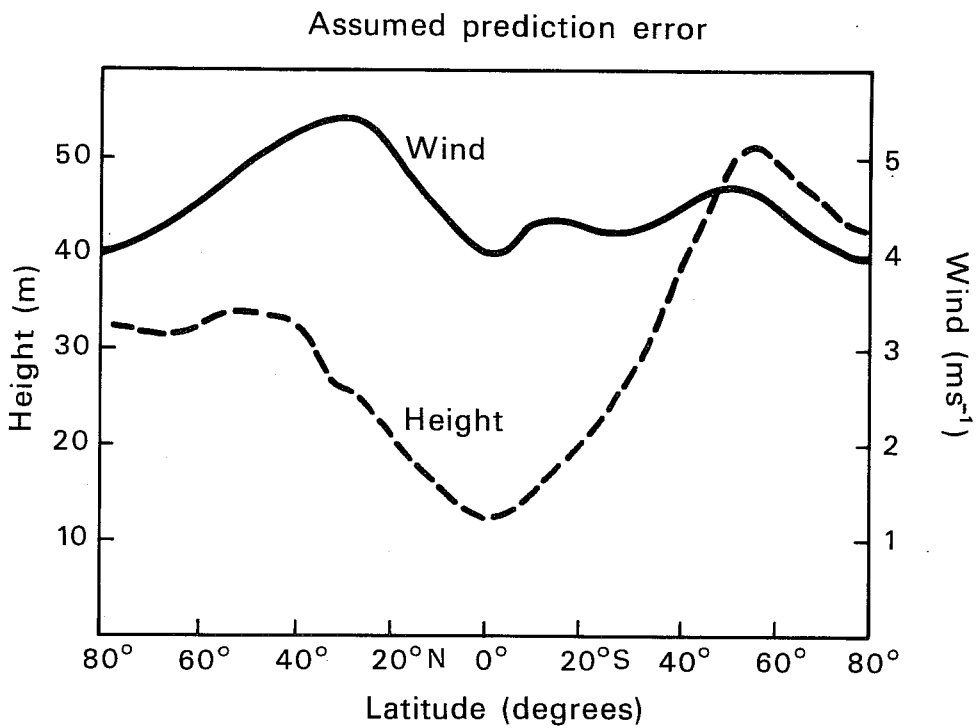## Assumed prediction error

Fig. 30 Assumed prediction error in the heights (dashed line) and winds (solid line) as a function of latitude for the experiments of section 4.2. The ordinate scale for the heights (m) is on the left and for the winds (ms^{-1}) is on the right.

It is necessary to make this spherical correction in order that the geopotential gradients be consistent with the winds in the x,y coordinate system.

We defined a multi-box analysis scheme with box centres 660 km apart and with each analysis box being 1320 km x 1320 km as before. Following the ECMWF system, b is defined to be 600 km north of 30N, 900 km south of the equator and linear in between. We define μ =.95 north of 30N, -.95 south of 30S and sinusoidal in between. We assume a Gaussian model with ν =0. The observation spacing is 750 km (similar to Cats and Wergen, 1982) and in each analysis box we search out radially a distance of 3b looking for observations. This gives approximately 50-70 observations per analysis box.

We assume an observation error of $3.4\,ms^{-1}$ in the wind and 12.1 m in the height everywhere. The prediction error was specified to be the zonally-averaged 500 mb winter values used by the ECMWF system. These are plotted in Fig. 30. These are related geostrophically in the extratropics $(E_V = gE_z/fb)$

We presented the analysis program with a series of large-scale normal modes of the ECMWF gridpoint model, which we linearly interpolated to our observation network. Rossby, Kelvin and gravity modes, symmetric and anti-symmetric, of different equivalent depths and zonal and meridional wavenumbers were all tested. We show here 4 examples. These are all external modes with an equivalent depth of 11886 m.

Fig. 31 shows the truth (left) and analysis (right) of the first symmetric Rossby mode of wavenumber 1 (5 day wave). The plots extend from 10 degrees south to 60 degrees north. The longitude, by equation 22, varies from top to bottom. The geopotential is contoured with a contour interval of 1 and
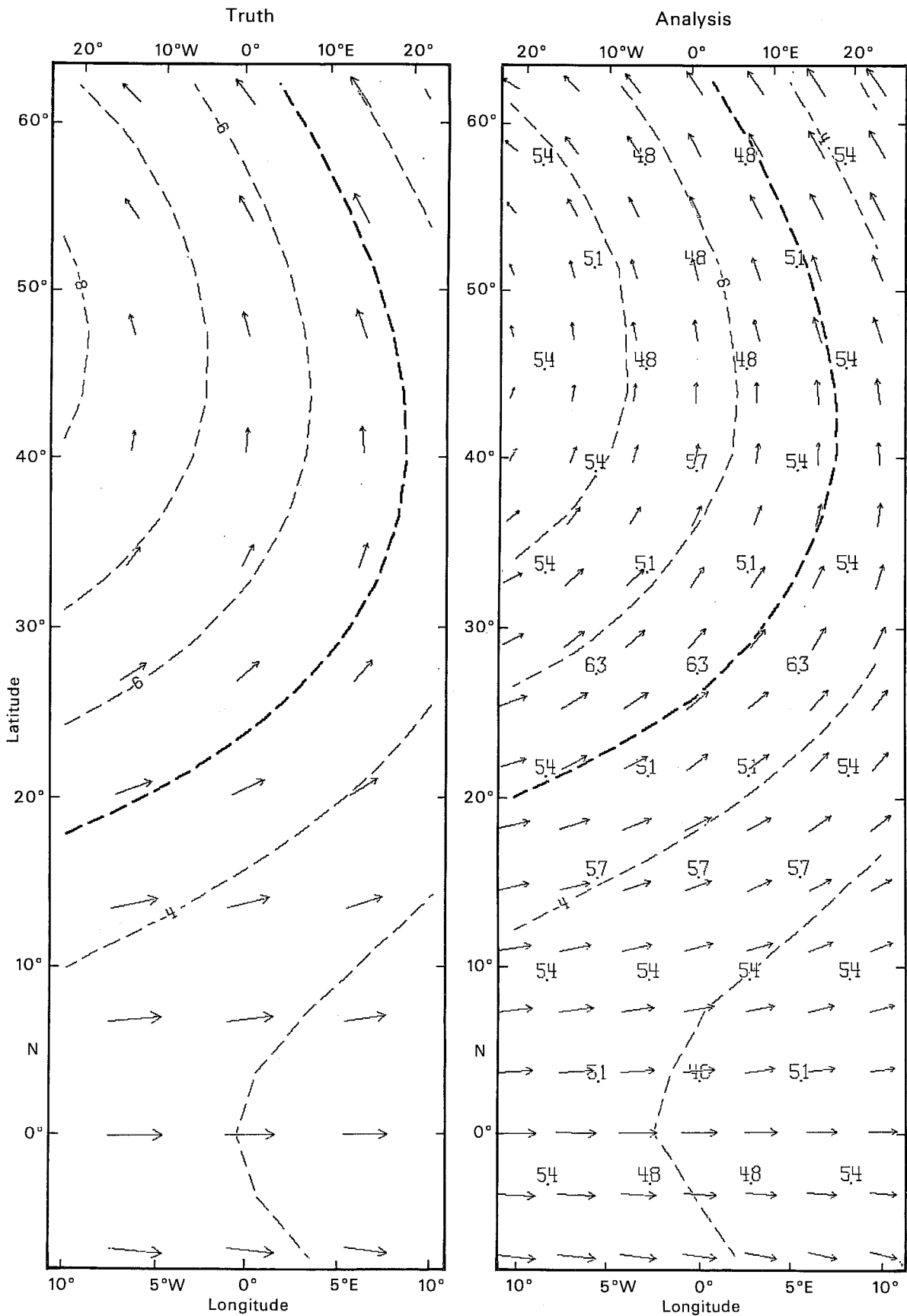
Fig. 31 An example of an analysis of a large-scale global mode by the OI
analysis system. This example is the first symmetric Rossby mode of
wavenumber 1. 'Truth' is on the left and the analysis on the right. The
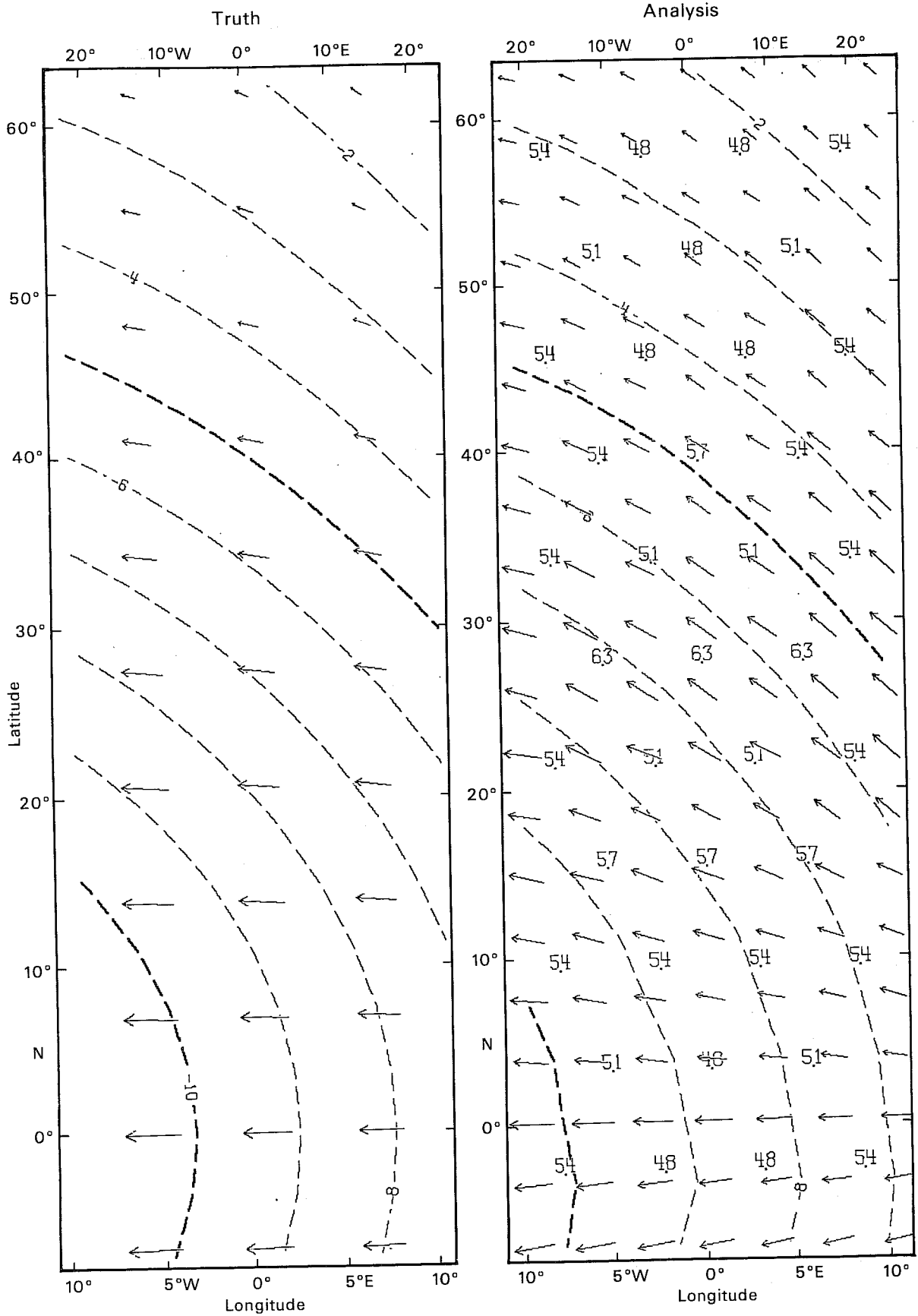ordinate is latitude and the abscissa is longitude.

Fig. 32   Same as Fig. 31 except for Kelvin mode (gravest symmetric eastward gravity mode of wavenumber 1).
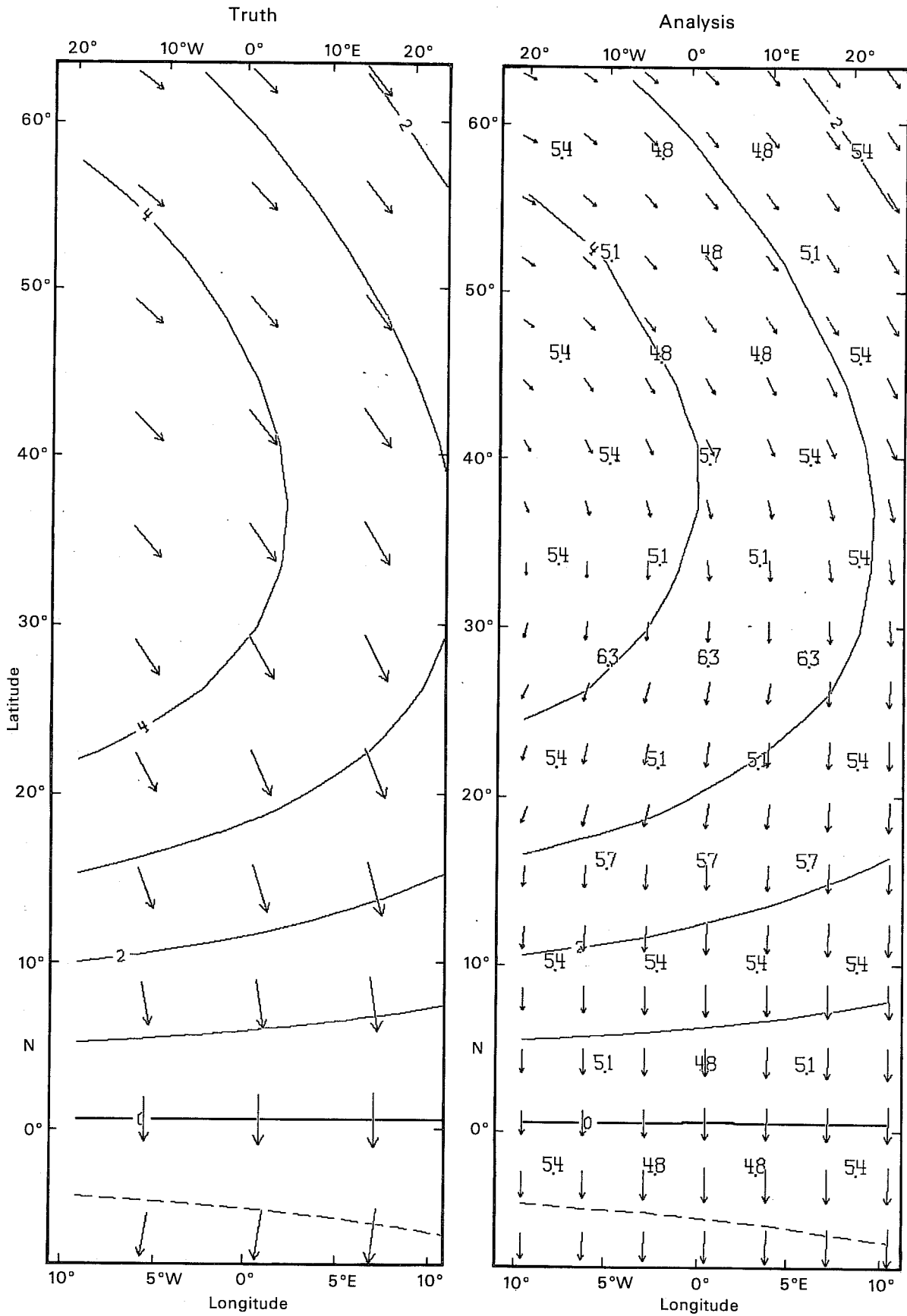
Fig. 33 Same as Fig. 31 except for mixed Rossby-gravity mode (gravest anti-
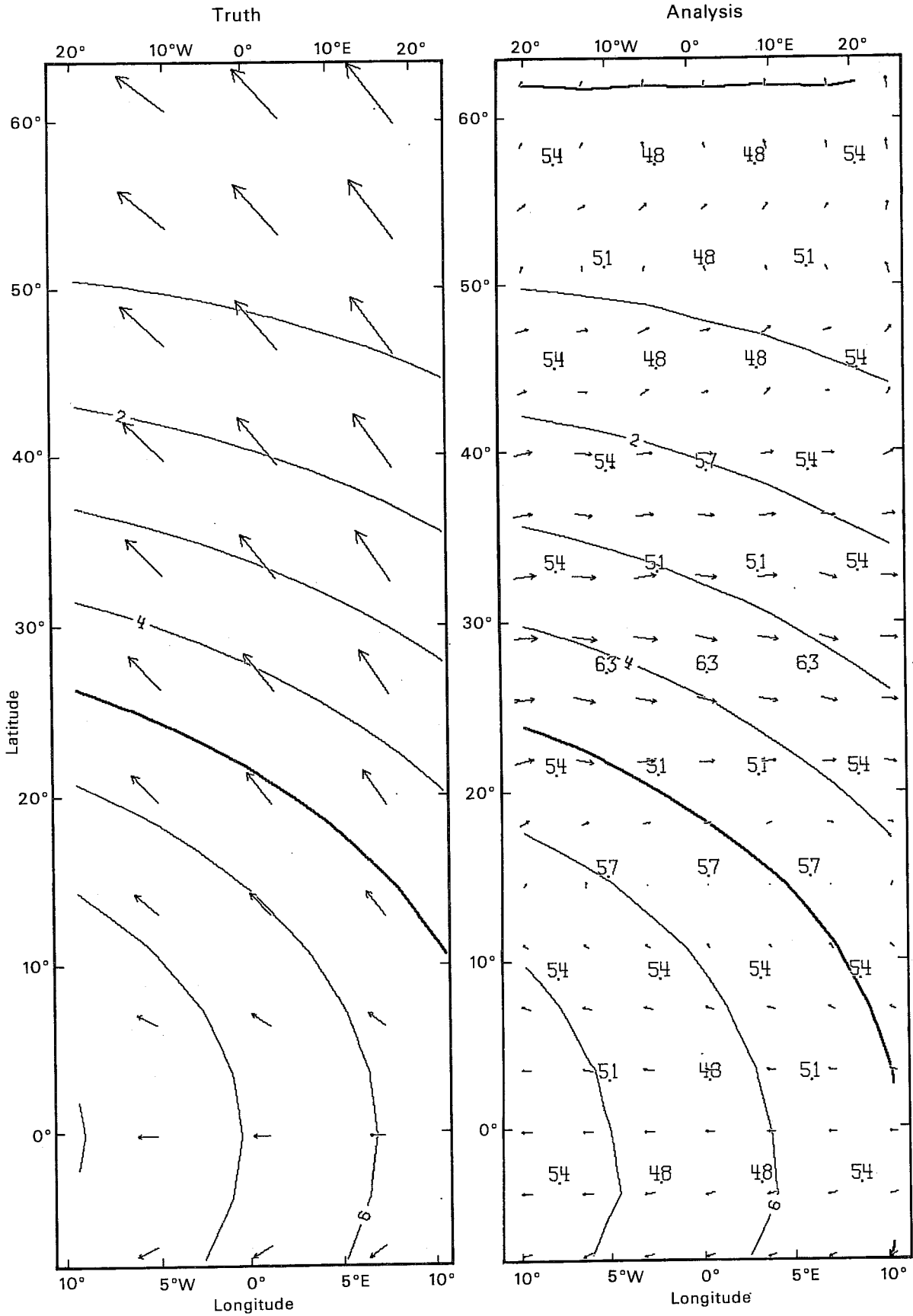symetric Rossby mode of wavenumber 1).

Fig. 34 Same as Fig. 31 except for gravest symmetric westward gravity mode of wavenumber 1.

the winds are indicated by the wind arrows. The winds can be strictly

compared between truth and analysis. The positions of the observations are

indicated by wind arrows on the truth plot. The box centres are indicated by

the large numbers on the analysis plot and the values of the numbers indicate

the number of observations used in that particular box. The analysis is

evaluated on a 400 km grid (indicated by the wind arrows on the analysis

plot). The analysis extends out further than is plotted, so there are no

edge effects.

Fig. 31 shows that the first symmetric Rossby mode is fairly geostrophic

except near the equator. The analysis scheme does a reasonably good job on

this mode except for a systematic under-drawing of the winds in the tropics.

The height analysis is good everywhere. All the parameters of the analysis

scheme are at most functions of latitude, so the relative response of the

analysis scheme is independent of longitude. (This is not the case with Cats

and Wergen's(1982) results, where the assumed prediction error is a function

of longitude and pressure as well).

Fig. 32, in the same format as Fig. 31, shows the first symmetric external

eastward gravity mode of wavenumber 1 (Kelvin mode). Again there is a very

good height analysis and under-drawing of the tropical windfield. In

addition, there is a systematic turning of the winds toward geostrophic in

the sub-tropics. In other words, this mode which is geostrophic at high

latitudes, is not completely geostrophic in the sub-tropics, but the analysis

system forces in geostrophy.

Fig. 33, in the same format as Fig. 31, shows the first antisymmetric

external Rossby wave of wavenumber 1 (mixed Rossby- gravity wave). Again the

height analysis is good everywhere and the high latitude wind analysis is

also good. The remaining wind analysis is very poor. The wind in the

tropics is under-drawn and there is substantial spurious turning of the wind

70

in the sub-tropics. This mode is the least geostrophic of the modes we
have shown so far, and it is not surprising that it is poorly analyzed.
However, the period of this mode (1.16 days) is not all that small and it
should be analyzed properly.

Fig. 34, in the same format as Fig. 31, shows the first symmetric
westward gravity mode of wavenumber 1. This is a true gravity mode and is
really nowhere geostrophic. As might be expected, the height is analyzed
well, but the winds are completely modified to be in geostrophic balance.
In effect, this gravity mode has been analyzed as a sort of Rossby mode.

Figs. 31-34 show that the analysis scheme analyzes the large-scale
geopotential field well. It generally does a good job on the winds at
high latitudes. It under-draws the large-scale windfield in the tropics
and enforces geostrophy too strongly in the sub-tropics. Most of these faults
disappear if a characteristic scale b is chosen which is more appropriate to
the large-scale flow - i.e. b ≃ 2000-5000 km. These general conclusions
are not at variance with those of Cats and Wergen (1982). Their specific
conclusions for a particular mode may differ from ours because of the
complicating effects of the vertical analysis problem. For example,
artificial analysis deficiencies could introduce an over-drawing of the tropical
windfield which could counteract the under-drawing noted in the present
experiments. Both the results of Cats and Wergen (1982) and the results of
this section are influenced in part by the choice of observation spacing
of 7.5 degrees. A finer observation spacing would produce less under-
drawing in the tropics.

5. CASE STUDIES OF DIVERGENT TROPICAL FLOW

The results of Sects. 3 and 4 suggest that there are real advantages in
using slightly divergent structure functions rather than the conventional
non-divergent structure functions. In particular, Fig. 28 shows the much
improved divergent response for intermediate waves if the non-divergence

71

constraint is relaxed slightly. However, there is one serious objection to
the use of divergent structure functions. That is the possibility that the
analysis procedure will produce more 'noise' or be less effective in
rejecting bad data.

To see how the slightly divergent structure functions behaved under more
realistic conditions we decided to do two case studies taken from the FGGE
data archives. These two cases - 12 GMT 16 December 1978 and 18 GMT 16
December 1978 had both been previously examined by Julian (1980). They were
both 200 mb analyses in the tropical western Pacific in which Julian (1980)
suspected that there were strongly divergent flows which were not well
analyzed by the conventional analysis system. We have chosen these cases
because the divergent outflow from the tropical convective clusters is at
about 200 mb, and because there are a great many aircraft reports and
satellite cloud winds at this level. The cases differ from each other
primarily in the amount of data available.

5.1 Case I - 12 GMT 16 December 1978

We show in Fig. 35 a wind analysis for this case. The region shown is from
2S to 22N and from 172W to 148W - i.e. in the tropical western Pacific. The
5 panels of Fig. 35 show the 6 hour forecast (produced by the ECMWF model),
the observations, the observation increment (observation minus forecast), the
analysis increment and the final analysis. The latitude is indicated along
the ordinate and the longitude along the abscissa. The wind speeds and
directions are indicated by the arrows. The wind magnitude can be obtained
from the box in the lower right hand corner of each panel which shows a wind
arrow and the corresponding speed in m/s. Note that the increment has been
scaled by a factor of 3. In the 6 hour forecast, analysis increment and
analysis the winds are on a regular 2 degree grid. Also shown in these 3
panels is the divergence field with a contour interval of 10^{-5} s^{-1}
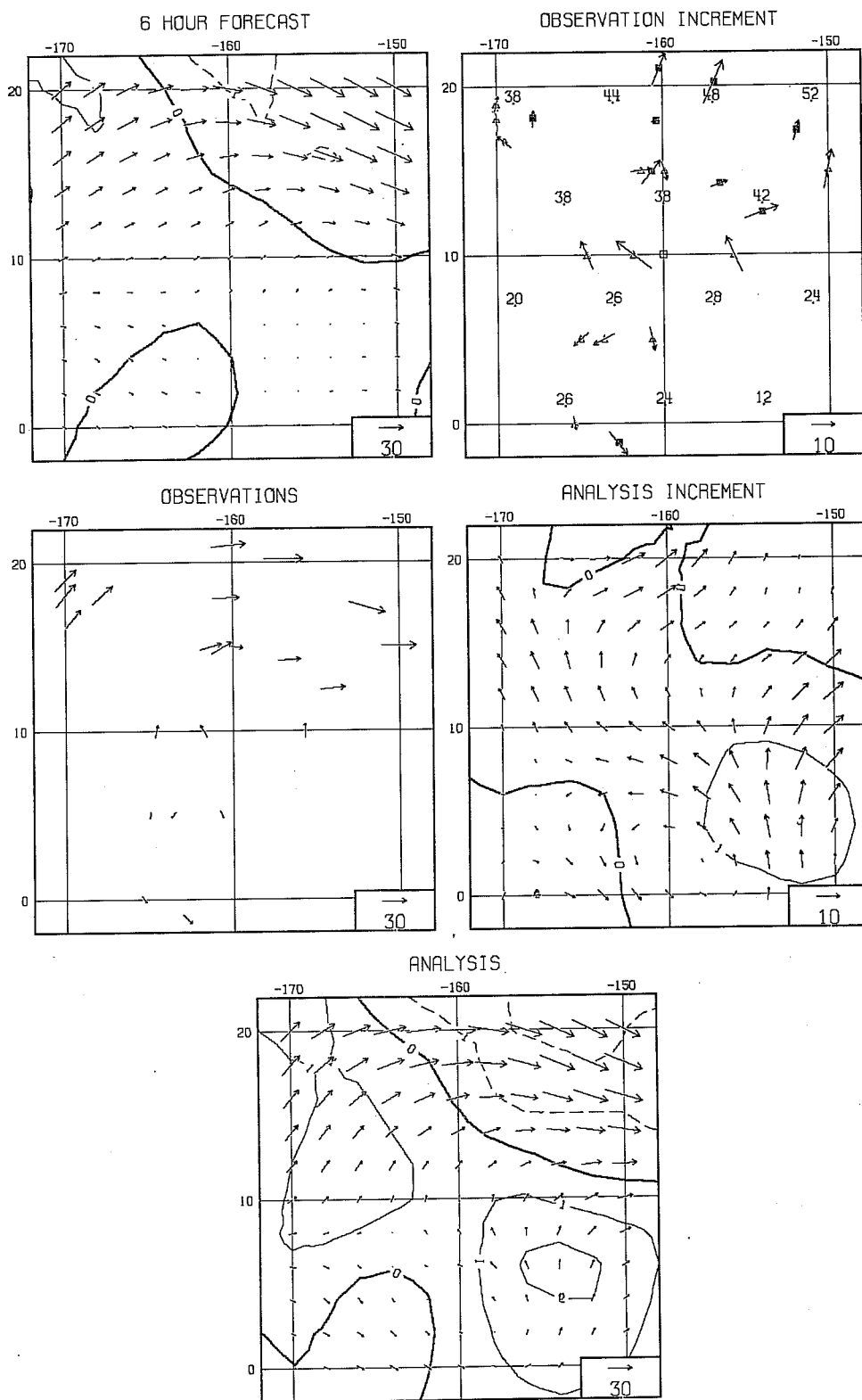(positive contours are solid while negative contours are dashed). This

Fig. 35   Wind analysis for the case of 12 GMT 15 December 1978 discussed
in section 5.1. The abscissa is latitude and the ordinate is
longitude. The winds are shown by arrows and the divergence by
the contours spaced at 10^{-5} 5^{-1}. The 5 panels shown are the 6
hour ECMWF forecast, the observations, the observation incre-
ment, the analysis increment and the final analysis. The box
centers and numbers of observations are shown in the observa-
tional increment panel. This panel also shows types of observa-
tions (key in text). The wind magnitudes (ms^{-1}) are indicated
by the box in the lower right hand corner.

divergence is calculated in a straightforward fashion using second order

centred differences. This divergence field would be similar, but not exactly

the same as that calculated by the finite difference operators of the ECMWF

model.

The 6 hour forecast was that used in the preparation of the FGGE IIIb grid

point analyses, interpolated to our 2 degree grid. The observations were

taken from the ECMWF FGGE archives. No geopotential or temperature

information was used. Three types of observations were used - aircraft winds

(AIREPS), satellite cloud winds (SATOBS) and radiosondes (TEMPS and PILOTS).

Any AIREP or SATOB between 300 mb and 100 mb was used directly with no

correction for off-time or off-level. The AIREPS are indicated by an open

triangle and the SATOBS are indicated by a solid square in the analysis

increment panel. There are no PILOTS or TEMPS visible in the panels shown.

All data checking was done manually and in the area of interest no data was

rejected.

A multi-box two-dimensional analysis was performed over an area approximately

twice the area shown to avoid edge effects. The position of the box centres

and the corresponding numbers of data in each box are shown by the numbers in

the observation increment panel. The box centres are 1320 km (6 degrees)

apart, with each analysis box being 6 degrees by 6 degrees. We define the

value of b exactly as in Sect. 4.1 and μ is assumed to be zero

everywhere. The prediction error was assumed to be 9.5/5.4 times the prediction

error shown in Fig. 30. This multiplicative factor reflects the

fact that we are doing a 200 mb analysis rather than a 500 mb analysis. We

assumed an observation error of 8.4 m/s for AIREPS, 7.5 m/s for SATOBS and

3.4 m/s for TEMPS or PILOTS. In Fig. 35 we used a Gaussian correlation

model with $\nu = 0$. The observation search radius was 1200 km.

Julian (1980), in examining this case, noted that there appeared to be a strong region of divergence oriented along a line from 8N, 170W to 9N, 150W. This was surmised, not only from the data plotted, but also from data 6 hours previously and also from GOES - WEST imagery for this time period. The analysis for this case made by the ECMWF system can be seen in Fig. 11 of Julian (1980) and can be directly compared with the wind analysis of our Fig. 35 (Note that the scaling of the wind vectors is not the same as ours and Julian plots isotachs rather than divergence.) Despite the use of a two-dimensional system with no vertical structure functions, the present analysis is reasonably consistent with the ECMWF analysis.

The ECMWF analysis apparently produced divergence of the order of 1-2 x $10^{-5}s^{-1}$ extending along the aforementioned line. Julian (1980) made a subjective analysis of the divergence in this case and determined that there were divergences in excess of 8 x $10^{-5}s^{-1}$ in the area. Julian (1980) attributed the apparently weak divergence in the ECMWF analysis to the use of non-divergent structure functions. We are now in a position to examine Julian's (1980) conjecture.

In Fig. 36, we show the analysis increment field (including the divergence) for CASE I as a function of ν; upper left hand corner (ν =0.), lower left hand corner (ν =.1), upper right hand corner (ν =.5), lower right hand corner (ν =1.). In all cases b= b_χ.

In examining Fig. 36 two points are fairly obvious. First of all, relaxing the constraint of non-divergence does not greatly enhance the divergence in this case. Secondly, the more divergent analyses even with ν =1. are not noticeably 'noisier' than for the non-divergent structure functions (ν =0.).

We will consider first the apparent failure of $\nu \neq 0$ to substantially enhance the divergence field. The results of Fig. 28, together with the
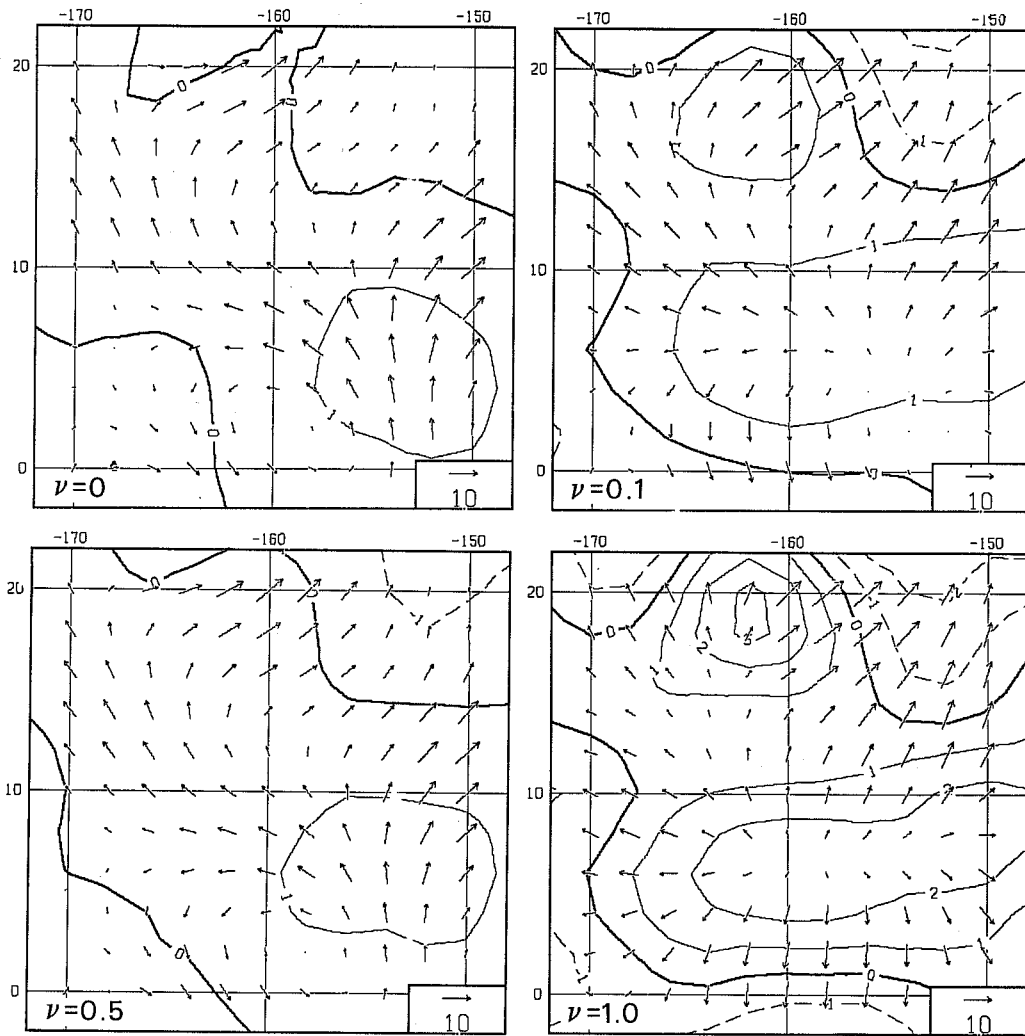
75

ANALYSIS INCREMENT

Fig. 36 Wind increments for the case shown in Fig. 35 for values of
ν=0, .1, .5 and 1

conjecture of Julian (1980) both gave reason to expect a stronger divergence

response when ν was increased. There is some increase in the divergence as

ν is raised, but the maximum value when $\nu = 1.$ is only $\simeq 3 \times 10^{-5} \, s^{-1}$.

The fact that the maximum divergence calculated here is much less than that

calculated subjectively by Julian (1980) is not particularly worrying because

the calculation of divergence is strongly dependent on grid-spacing and

choice of finite difference operator. What is a little harder to understand

is why the change in calculated divergence field between $\nu = 0.$ and $\nu = \cdot 1$

is so small when compared to the response diagrams of Sect. 4.

The major problem in this case is that there really isn't enough data to

define the divergence field well. Subjectively, the divergence field is

defined by the 3 northward pointing wind vectors at 10N and the 3 southward

pointing vectors at 5N in the observation increment field of Fig. 35. On

the other hand, the analysis increment for $\nu = 0.$ (Fig. 36) has the main

divergence centred at 5N , 155W where there is really no data at all. Very

likely, there is a large fictitious component of divergence in all the

analyses of Fig. 36. This situation is far removed from the regular

observation network used in producing Fig. 28.

We will now consider the second point mentioned earlier, the apparent lack

of 'noise' in the analyses with divergent structure functions $(\nu \neq 0.)$ of

Fig. 36. The apparent 'smoothness' of these analyses even when $\nu = 1.$

were somewhat surprising at first, because it is widely believed that the

constraint of non-divergence acts as a noise filter for the analyzed wind

field.

We can explain our result with the following simple thought experiment.

Suppose we had two situations of wind observation increment which were very

close to each other and yet completely disagreed.
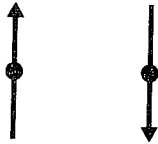
Type A   Type B

We will assume the distance between observations $\Delta x \ll b$ and that there is no

external reason to reject any of the data. Both of these situations would

tend to produce noise in the analysis. An analysis with $\nu = 0.$ would

completely suppress TYPE B noise, but would partially draw for TYPE A

'noise'. On the other hand, and analysis with $\nu = 1.$ would completely

suppress TYPE A 'noise', but would partially draw for TYPE B 'noise'. The

form of 'noise' produced in the two cases would be different - TYPE A 'noise'

would be rotational and TYPE B 'noise' would be divergent - but the magnitude

of the 'noise' would be the same. Since situations represented by TYPE A are

just as likely to arise as the situations represented by TYPE B, the kinetic

energy spectrum of an ensemble of analyses would contain approximately the

same amount of small scale 'noise' for the case $\nu = 1.$ as for the case of

$\nu = 0.$ In fact, examination of Fig. 3 might suggest the 'noise' would be

minimized for $\nu = .5.$ It would seem that the 'noise' is controlled by the

choice of structure functions and characteristic scale and not by setting

$\nu = 0.$

The results of CASE I were not as expected. Slightly relaxing the non-divergent constraint did not greatly increase the divergence as might have been expected from Sect. 4. On the other hand, the wind analyses, even with $\nu = 1.$, were not nearly as 'noisy' as expected.

5.2 CASE II - 18 GMT 16 December 1978

We show in Fig. 37 the 6 hour forecast, observations, observation increment, analysis increment and analysis for this case in the same format as Fig. 35. The prediction error correlation model is Gaussian, $\nu = 0.$ and the search radius is 1200 km. All other parameters are exactly as in Fig. 35. It is apparent that there are many more data for this case as an apparent divergent flow can be seen by eye in the observation increment field.

In Fig. 38 we show the analysis increments for this case as a function of ν in the same format as Fig. 35. That is, $\nu = 0.$ upper left hand corner, $\nu = .1$ lower left hand corner, $\nu = .5$ upper right hand corner, $\nu = 1.$ lower right hand corner. What is immediately obvious is the large change between the cases of $\nu = 0.$ and $\nu = .1$. The flow becomes noticeably more divergent with $\nu = .1$ in this case. The divergence naturally increases as ν is increased, but at $\nu = 1.$ there is scarcely any more divergence than in CASE I. Again, as in CASE I there is no appreciable increase in 'noise' in going from $\nu = 0.$ to $\nu = 1.$

In Fig. 39 we show the analysis increments for CASE II in the same format as Fig. 38 for the case where we have used a Markov structure function instead of a Gaussian. As before, there is a fairly strong change between $\nu = 0.$ and $\nu = .1$, but by and large, there is as much divergence produced as in the Gaussian case. There is, however, noticeably more 'noise' in the Markov case; both in the windfield and in the divergence field. This result might have been anticipated from Sect. 3.
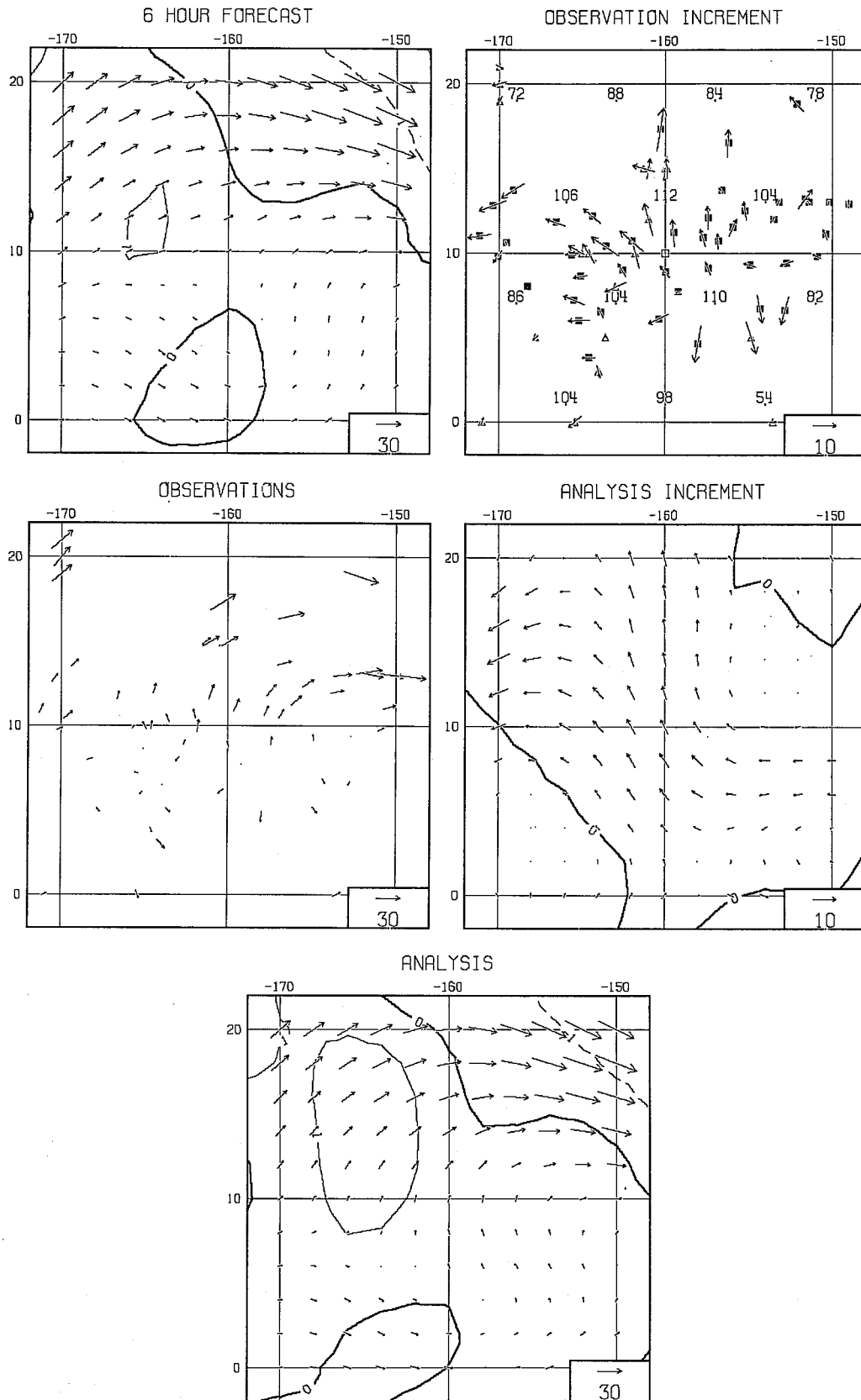
Fig. 37   Wind analysis for the case of 18 GMT 16 December 1978 in the
          same format as Fig. 35.

ANALYSIS INCREMENT
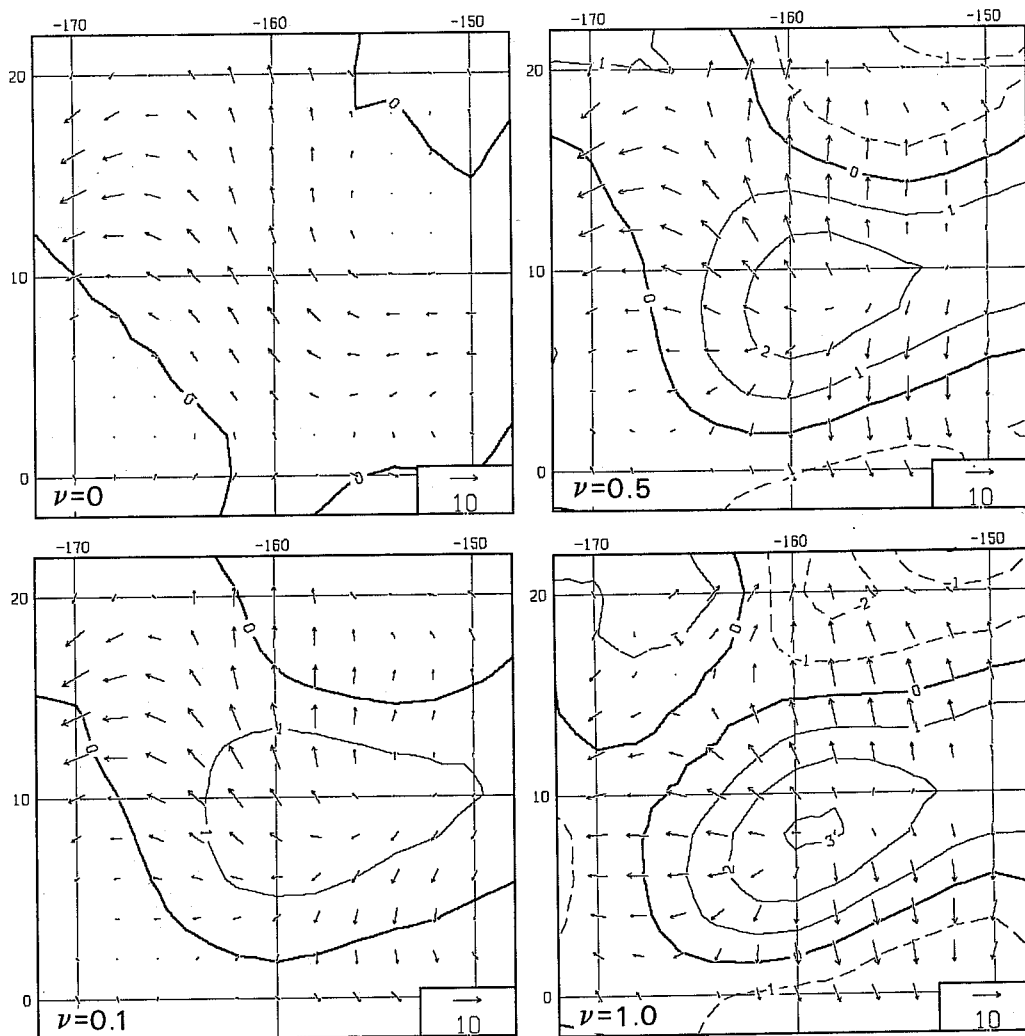
Fig. 38 Wind increments for the case of 18 GMT 16 December 1978 in the same format as Fig. 36, with $\nu=0$.

ANALYSIS INCREMENT

Fig. 39   Wind increments for the case of 18 GMT 16 December 1978 in the same format as Fig. 38 except for the Markov function.

ANALYSIS INCREMENT

ANALYSIS INCREMENT

$\nu=0$

$\nu=0.5$

ANALYSIS INCREMENT

OBSERVATION INCREMENT

$\nu=0.1$
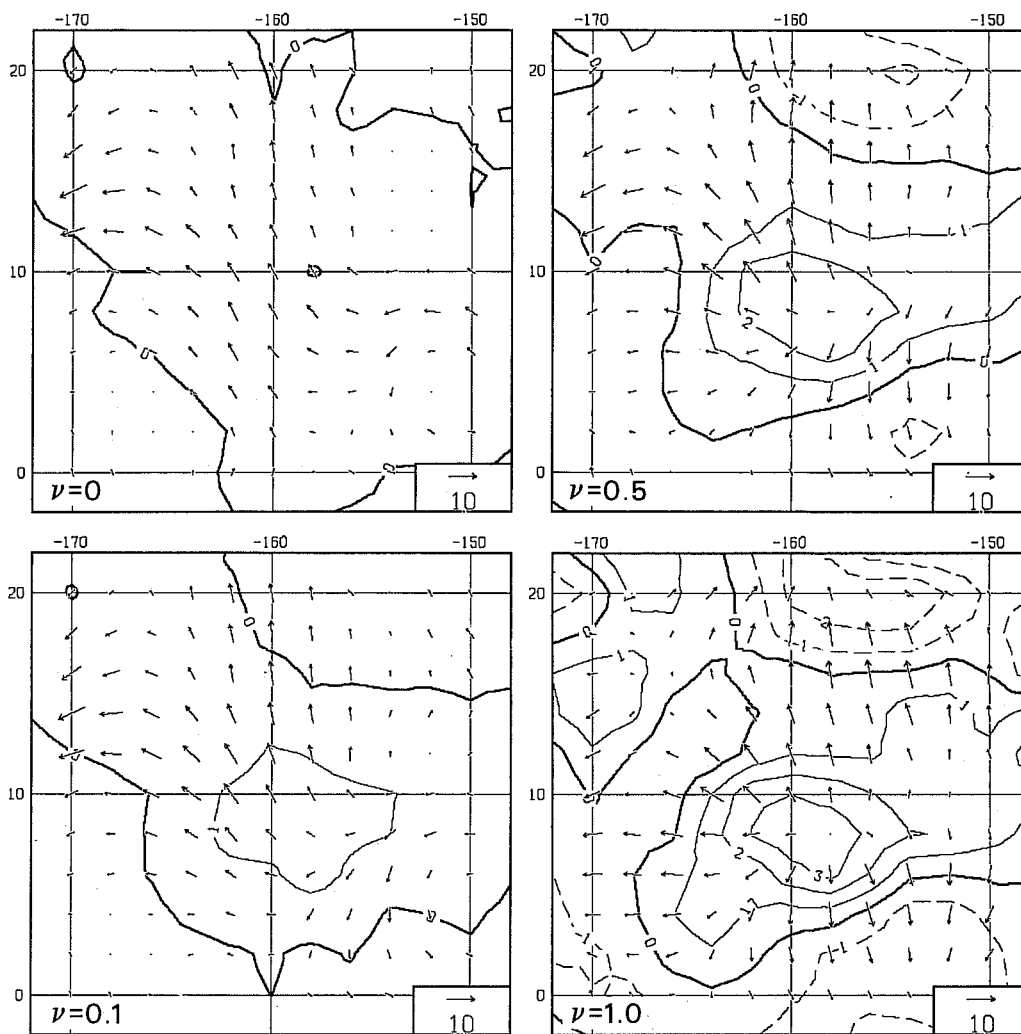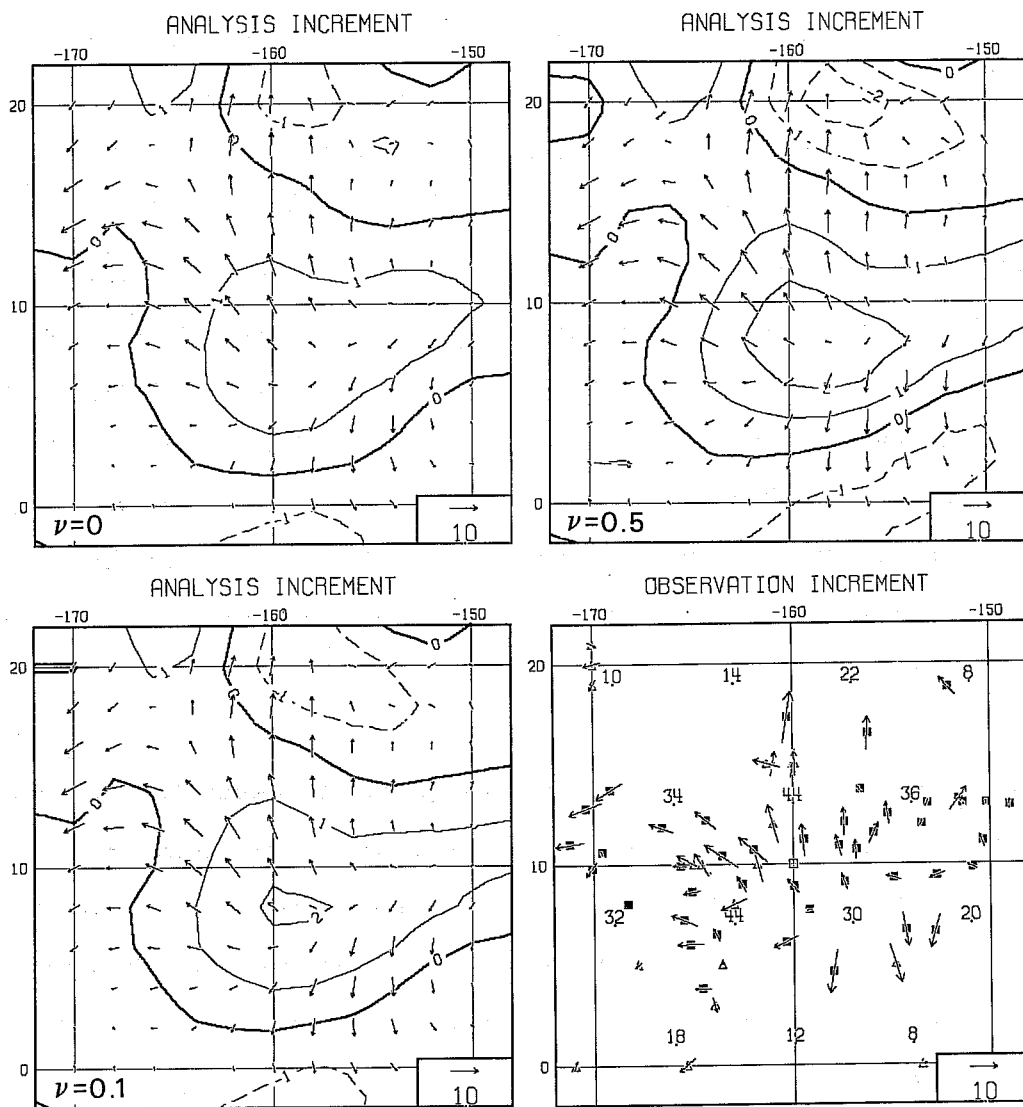
Fig. 40   Wind increments for the case of 18 GMT 16 December 1978 in the
same format as Fig. 38 except for a 600 km search radius.

In the course of this work, we have not generally been much concerned with

data selection strategies. In the regular observation networks used in

Sects. 3 and 4, the results are not all that sensitive to data selection.

For an irregular observation network, however, data selection does make a

difference as we show in Fig. 40. Here we show CASE II analysis increments

for $\nu = 0.$ upper left hand corner, $\nu = .1$ lower left hand corner, and

$\nu = .5$ upper right hand corner for an observation search radius of 600 km. All

other parameters are identical to those of Fig. 38. The number of

observations in each analysis box are indicated in the observation increment

panel in the lower right hand corner. Here, we notice that with many fewer

data selected the case $\nu = 0.$ differs substantially from the corresponding

panel of Fig. 38, with much more divergence being drawn in Fig. 40. On the

other hand, the $\nu = .1$ panels (lower left corner) are fairly similar in

Figs. 38 and 40. What is encouraging is that setting $\nu = .1$ seems to

produce a fairly consistent result even when the data selection algorithm is

substantially changed.

The experiments of Sect. 5 have been at least partially successful. We have

found that in one case, at least, slightly relaxing the non-divergence

constraint produces a substantially improved divergence analysis. This

analysis seemed to be less sensitive to changes in data selection strategy

than for an analysis produced using completely non-divergent structure

functions. Moreover, we have not found the analyses produced by slightly

divergent or even completely divergent structure functions to be noticeably

more 'noisy' than for the completely non-divergent structure functions.

Of course, relaxing the constraint of non-divergence is only the simplest of

several steps that must be taken to produce good tropical divergence

analyses. The high level outflow discussed here must be combined with low

level inflow if the divergence fields are not to be destroyed by the

initialization process or natural Rossby adjustment in an uninitialized

model.   The combination of good low level wind data with appropriate vertical

correlations will be required.   The use of IR data to define the high level

clouds as suggested by Julian (1980) would also be helpful.   A third

ingredient for quality tropical divergence analyses is a sound convective

parameterization scheme for production of the first guess field.

6. THE ANALYSIS OF LARGE-SCALE TROPICAL FLOW WITH A REALISTIC OBSERVATION NETWORK

The experiments of Sect.4.2 together with the results of Cats and Wergen (1982) have suggested that there are deficiencies in the analysis of the large-scale flow even with a uniform observational network. Further experiments have been performed by Cats and Wergen (1982) which imply that the analysis of the large-scale flow is even worse when a realistic observation network is used. In these experiments a single large-scale Rossby or Kelvin mode was sampled on a realistic non-uniform observation network (obtained from an operational file). These pseudo-observation minus forecast data (synthetic but realistically distributed) were then analyzed by the operational ECMWF analysis procedure. The analysis produced by the ECMWF analysis system from these pseudo-observations was very poor, with the input mode being severely damped together with substantial aliasing onto the other modes. They were able to define a response matrix which demonstrated how the amplitude of any particular large-scale mode was aliased onto the other modes. As before, the problem was the worst in the tropics.

These results of Cats and Wergen (1982) are somewhat alarming, because they suggest that there may be serious errors in the operational analysis of the large-scale flow. Their results, however, are somewhat at variance with two earlier studies - those of Leary and Thompson (1973) and Baer and Tribbia (1976). Leary and Thompson (1973) examined the response of the analysis system of Starr et al. (1970) to the input of single spherical harmonics of geopotential sampled at the Northern Hemisphere radiosonde locations. They found that there was a good response for large-scale spherical harmonics and a poor response for small-scale harmonics, which is intuitively reasonable. Baer and Tribbia (1976) defined a 'true'

one-dimensional Fourier representation which they sampled on various

irregular one-dimensional networks. The analysis was performed using a

Gram-Schmidt analysis procedure which produced estimates of each Fourier

coefficient directly from the pseudo-observations. They concluded that

wavelengths greater than or equal to twice the maximum gap in the network

would be well-analyzed, but that shorter waves would not. These results of

Leary and Thompson (1973) and Baer and Tribbia (1976) are intuitively

reasonable, but they are at variance with the results of Cats and

Wergen (1982).

The single-wave experiment of Cats and Wergen (1982), although philosophically

similar to that of Leary and Thompson (1973), is considerably more realistic.

It is global and thus includes tropical problems. It is multivariate and the

input modes are also multivariate. It is three-dimensional and thus includes

the very difficult vertical problem.

Presenting the analysis system with a single mode and examining the resulting

response is a technique we have used extensively in the uniform observation

network experiments of Sect.4. However, the OI method assumes that there

exists a spectrum of specified character, and not just a single wave, so that

in some sense, the single wave experiments are unfair. For the uniform

network experiments of Sect.4, it is reasonable to deal with individual waves

because of the linearity of the problem and because aliasing is minimal except

for the short waves near the Nyqvist limit. In the realistic network case,

however,the validity of single wave experiments is less clear. Cats and

Wergen (1982) demonstrate that there is substantial alaising from a given wave

into other waves. Since the aliasing can obviously go in both directions and

may have constructive as well as destructive properties, it is possible that

single wave experiments could give misleading results.

We can distinguish here between two types of errors. Let us suppose that we

have a group of large-scale waves that we wish to analyze. We will further

suppose that we are only interested in the low-frequency modes - Rossby and

Kelvin waves. We could construct a large-scale 'truth' from these modes,

sample it on a realistic network and present these pseudo-observations to the

OI system. From the resulting analyses on a uniform grid, we could project

back onto the set of large-scale Rossby and Kelvin modes and calculate the

error. This is essentially what was done by Cats and Wergen (1982) and more

simply by Leary and Thompson (1973), except that they only presented one mode

at a time. This type of error we will refer to as direct error.

There is, however, another type of large-scale error not examined by either

Cats and Wergen (1982) or Leary and Thompson (1973). That is the error caused

by the aliasing of smaller-scale waves into the large-scale waves due to an

inhomogeneous observation network. We will refer to this type of error as

indirect error.

It is clear that OI methods have both direct and indirect error. There are

analysis methods, however, which have no direct error. For example, a

least-squares fit to the large-scale Rossby and Kelvin modes, will have zero

error if the original pseudo-observations were constructed solely from these

modes. This is true on virtually any arbitrary observation network.

In this section we intend to investigate a number of questions raised in the

preceeding discussion. Our experiment will concentrate on the analysis of

the large-scale tropical flow. As before the experiment will be restricted

to two-dimensions, but in most other respects it will be more general than

previous work in this area.

We will define a 'truth' which is hopefully realistic in its spectral

characteristics and which is known everywhere. We will define two realistic

observation networks taken from the FGGE observational coverage. We will

sample the 'truth' with and without observational error at the observational

points and use the OI technique to obtain uniform grid analyses. We will

then project the analysis onto a set of large-scale Rossby and Kelvin modes and compare the results with the appropriate 'truth'. We will also develop a direct least-squares method for calculation of the Rossby and Kelvin modes and compare the results with the OI procedure. Both direct and indirect errors will be calculated. We shall attempt to resolve the discrepancies between the results of Cats and Wergen (1982) and the earlier results of Leary and Thompson (1973) and Baer and Tribbia (1976). We will also examine the validity of single wave inhomogeneous network experiments.

6.1 Experimental design

Perhaps the most controversial aspect of experiments of this type is the choice of the 'truth'. We wish to define a 'truth' which would have all the characteristics of an observed minus forecast field, if such a field could be known everywhere. The requirement of being known everywhere automatically precludes the use of real observations, so we are forced to rely on existing analyses. We decided to use the fields obtained by subtracting two existing ECMWF analyses 6 hours apart as our 'truth'. These analyses are the uninitialized 200 mb heights and winds for 00 and 06 GMT January 15, 1979.

This 'truth' is shown in Fig.41(a) - geopotential height (m) and Fig.41(b) - winds (ms^{-1}) on a 4 degree grid. These figures show the sections from 36 degrees South to 36 degrees North and from 180 degrees East to 180 degrees West. The contour interval for geopotential is 30 meters and the wind magnitude (in ms^{-1}) is indicated by the box in the lower right hand corner of Fig.41(b). The tropical domain which we intend to use throughout this experiment is defined by Fig.41. The rms height and vector wind variances in Fig.41(a) and (b) are 22.16 meters and 6.913 ms^{-1} respectively.

The roughly geostrophic character of the 'truth' at higher latitudes is evident. It is also clear that there is power in all parts of the spectrum, particularly in the smaller scales. We have chosen the 200 mb field for two
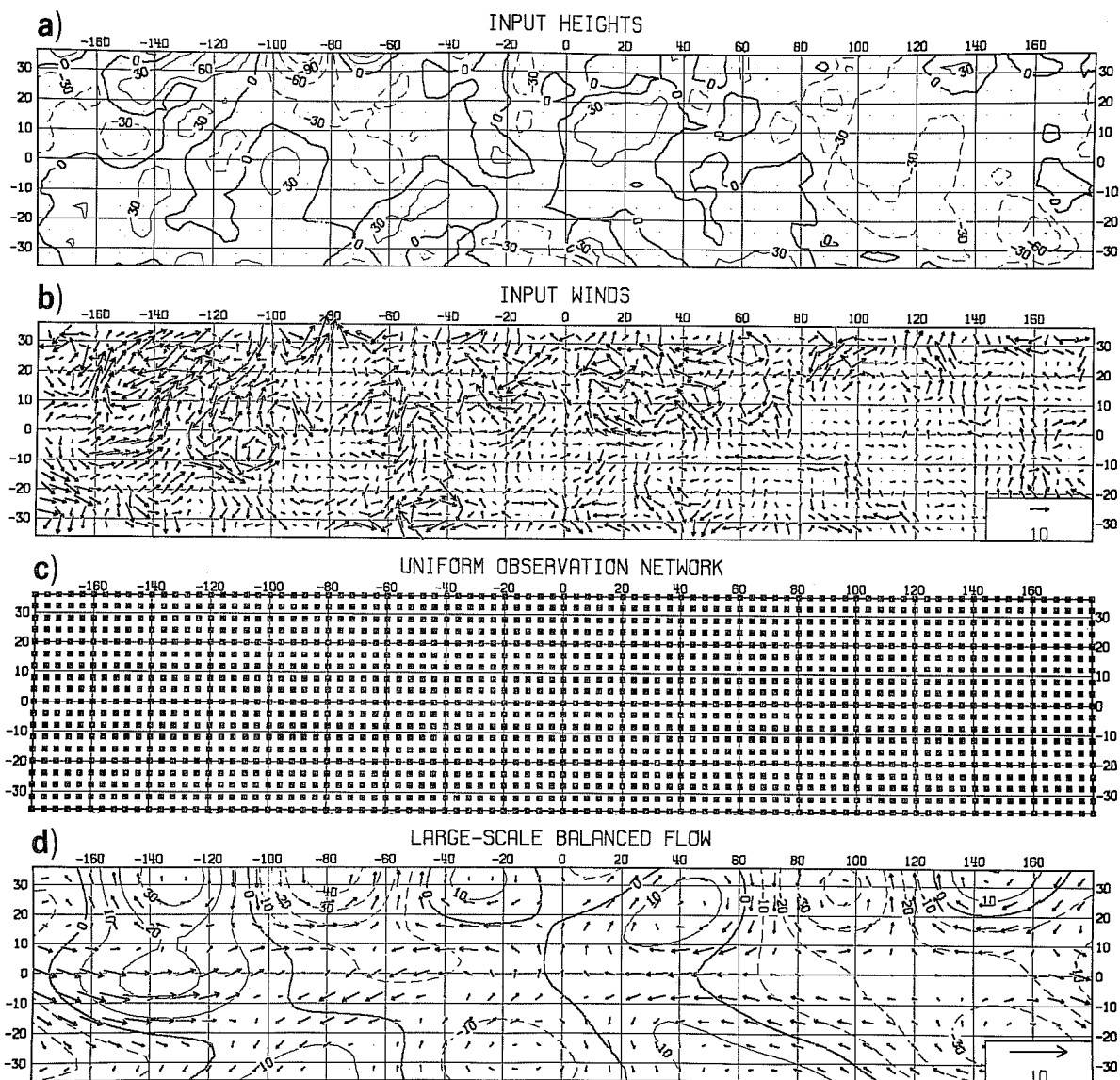
Fig. 41   Input height fields (a), wind fields (b) for the experiment of section
6. The height field has a contour interval of 30 meters and the wind
field is on a 4 degree grid with magnitude (ms^{-1}) indicated in the
lower right hand corner. The uniform 4 degree grid used for analyzing
the large-scale balanced flow is shown in Fig. 41 (c). The solid
squares indicate the observation position. The resulting large-scale
balanced flow (Rossby and Kelvin waves of zonal wavenumbers 0-4)
determined from Fig. 41 (a) and (b) by network 41 (c) are shown in
Fig. 41 (d). The abscissa is longitude and the ordinate is latitude.

reasons. Firstly, the tropical observation network at 200 mb is better than at most other levels. Secondly, the 200 mb tropical flow is more interesting than, say, the 500 mb tropical flow.

The next task is to determine the large-scale 'truth' from the complete 'truth' shown in Fig. 41(a) and (b). We will arbitrarily define the large-scale 'truth' as consisting of the 4 gravest Rossby modes and the Kelvin mode of zonal waves 0 to 4. This defines $5 \times (2 \times 4 + 1) = 45$ degrees of freedom. In three-dimensional experiments Rossby and Kelvin modes of many different equivalent depths would be relevent. In two-dimensional experiments, however, there is only one equivalent depth which is at the disposal of the experimenter. Because this was a tropical 200 mb experiment, we decided to use the second internal mode of the ECMWF model, which has an equivalent depth of 928 meters. We note that this mode is essentially an upper tropospheric mode with a peak around 200 mb and is largely tropically trapped.

As mentioned before, the domain of the experiment is 36 degrees North to 36 degrees South. We use the horizontal modes corresponding to the second internal mode of the ECMWF model, which are orthogonal over the sphere. The modes of different zonal wavenumber or different equatorial symmetry are also orthogonal over our tropical domain. However, waves of the same zonal wavenumber and symmetry are not orthogonal over the tropical domain. Although, not strictly necessary for our experiments we decided to make the modes orthogonal over the tropical domain by using a simple Gram-Schmidt procedure on the global ECMWF modes. We started with the Rossby and Kelvin modes and constructed a new set of Rossby, Kelvin and gravity modes which were orthogonal over the tropical domain. It might be noted, that because of the way the procedure was ordered, all the orthogonal Rossby and Kelvin modes were linear combinations of the old non-orthogonal Rossby and Kelvin modes. This Gram-Schmidt process is not strictly necessary and all results obtained in this section are virtually unchanged if it is not used.

The large-scale 'truth' (Rossby and Kelvin waves) was constructed from the complete 'truth' using the uniform 4 degree observational network shown in Fig.41(c). The solid squares in this figure are the uniform observation points where each of u,v, and z are assumed to be known. The resulting large-scale 'truth' is shown in Fig.41(d). The height contour interval is 10 meters and the winds are shown every 8 degrees with the wind magnitude shown in the lower right hand corner in ms^{-1}. The rms height and wind vector variance of these large scale fields are 16.18 meters and $2.036ms^{-1}$ respectively. Again, the geostrophic character at higher latitudes is evident. We might add here, that if Rossby and Kelvin modes of a different equivalent depth (say 10 km) were to be used, Fig.41(d) would not be substantially different.

The next step is to define the observation network. The FGGE observation network for 00 GMT 15 January 1979 was used as a basis. Two categories of observations were defined. Firstly, observation types which had a complete vertical sounding such as TEMPS, PILOTS and SATEMS and secondly, single level data such as AIREPS and SATOBS. Any single level data point in the tropical domain between 300 mb and 100 mb was considered to constitute an observation point. In order to make the experiment truly tropical and to avoid edge effects we assumed that we have observations of u,v, and z every 4 degrees of longitude at 32 and 36 degrees North and South. The complete observation network can be seen in Fig.42(a). Complete u,v, and z reports are shown by solid squares, z only by stars and winds only by 'v'. It is fairly easy from Fig.42(a) to pick out satellite tracks and the radiosonde network. We note that we use the FGGE data to determine the observation position and type, but make no other use of the data.

The observation network shown in Fig.42(a), which we will refer to as Network 1 is a fairly complete network. It is not representative of other levels because it includes much single level data. Single level data aliases

OBSERVATION NETWORK 1

OI BOX CENTERS - 1

OBSERVATION NETWORK 2

OI BOX CENTERS - 2

Fig. 42   Observation network 1 and 2 are shown in Figs 42 (a) and (c). The box
centers with numbers of observations are shown in Figs. 42 (b) and
(d). Solid squares indicate observations of u, v and z, stars indi-
cate observations of z only and v indicates observations of u and v
only.

badly in the vertical and would be the cause of much error in a three-dimensional experiment such as that of Cats and Wergen (1982). Consequently, we constructed a second network shown in Fig.42(c) which has no single level data and is thus more representative of the network used in Cats and Wergen(1982). This network we shall refer to as Network 2.

The OI analysis procedure used in the subsequent experiments was much the same as that used in Sect. 4.2. Thus the definition of b, μ, ν, box size etc. were unchanged. Our standard version had a data search radius of 800 km, but we limited the number of observation per box to 50. The only change of any significance from Sect. 4.2 was that the 200 mb rather than the 500 mb prediction error was used. The assumed observation error for the winds was 5 ms^{-1} and for the heights was 12 meters. The box centres and numbers of observations per box for the two networks are shown in Fig.42(b) and (c), for a search radius of 800 km. In the OI procedure we worked with a strict latitude-longitude coordinate system and did not alter the geometry as in Sect. 4.2 because the analysis went no further from the equator than 40^0. We did, however, partially correct for the convergence of the meridians by using approximately the true spherical distance in the prediction error correlation function.

As mentioned earlier, we also tested a second procedure – a direct least-squares estimate of the large-scale Rossby and Kelvin waves. This procedure is related to an experimental procedure described by Halberstam and Tung (1983). This procedure has no direct error, and it also has the correct multivariate large-scale tropical relationship. This procedure attempts to minimize the following sum:

$$I = \sum_{i} [F(i) - \sum_{\ell} A^{\ell} G^{\ell}(i)]^2 W(i)\cos\phi_{i} \qquad (23)$$

where i indicates an observation point,

F(i) is a datum at the observation point i,

$G^{\ell}(i)$ is the value of a particular large-scale Rossby or Kelvin or gravity mode at the point i,

A^{ℓ} is the unknown amplitude of the mode $G^{\ell}(i)$,

W(i) is a specified weight function,

ϕ_{i} is the latitude of the point i.

Minimizing this sum with respect to the A^{ℓ} gives

$$\sum_{k} A^{k} R^{k}_{\ell} = F^{\ell} \qquad (24)$$

where

$$F^{\ell} = \sum_{i} F(i) G^{\ell}(i) W(i) \cos\phi_{i}$$

$$\qquad (25)$$

$$R^{k}_{\ell} = \sum_{i} G^{\ell}(i) G^{k}(i) W(i) \cos\phi_{i}$$

This defines a matrix problem of order L where $1 \leqslant \ell, k \leqslant L$. In actual fact, the $G^{\ell}(i)$ are vectors with u,v, and z components, so the more

correct form of F^{ℓ} is

$$F^{\ell} = \sum_{i} \left[F_u(i)\ G_u^{\ell}(i)\ \tilde{\Phi}\ W_u(i) + F_v(i)\ G_v^{\ell}(i)\ \tilde{\Phi}\ W_u(i) \right.$$

$$\left. + F_{\Phi}(i)\ G_{\Phi}^{\ell}(i)\ W_{\Phi}(i) \right]\ \cos\ \Phi_i \tag{26}$$

where $F_u(i)$, $F_v(i)$, $F_{\Phi}(i)$ are data at the point i,

$G_u^{\ell}(i)$, $G_v^{\ell}(i)$, $G_{\Phi}^{\ell}(i)$ are the values of u, v, or z components of a particular large-scale mode,

$W_u(i)$, $W_{\Phi}(i)$ are the relative wind or height weights,

$\tilde{\Phi}$ is the equivalent depth.

The complete equation for R_{ℓ}^{k} is obtained in the same way as equation (26).

We note that in equation (26) we do not require that the observation points be regular or that all of u,v,z be available at every point. In the case of the ECMWF modes with a regular observation grid consisting of the grid points of the ECMWF model and all $W(i) = 1$, the R_{ℓ}^{k} would equal δ_{ℓ}^{k} - the Kronecker delta. In the case of the Gram-Schmidt orthogonalized modes defined on the regular 4 degree tropical grid shown in Fig. 41(c), the R_{ℓ}^{k} would equal δ_{ℓ}^{k}. In general, however, the R_{ℓ}^{k} is a full matrix.

The fact that the R_{ℓ}^{k} is a full matrix limits the utility of the method to

less than ≃ 500 degrees of freedom because of machine constraints. In addition, it is well-known that this method (when used with many degrees of freedom) gives good results in data-rich regions,but gives bizarre results in data-poor regions. For these two reasons we must limit ourselves to a sub-set of large- scale modes. We choose the set of modes to consist of the 4 gravest large-scale modes (Rossby, Kelvin and gravity) for the second internal mode of zonal waves 0 to 4. This gives 4x3x(2x4+1) = 108 degrees of freedom. We have arbitrarily chosen to include the large-scale gravity modes in this process to reduce aliasing into the large-scale Rossby and Kelvin modes that really interest us. We note in passing, that the reason that the Gram-Schmidt procedure discussed earlier, was not strictly necessary was that the least-square procedure (24) can be used to obtain the amplitude of the large-scale Rossby and Kelvin modes from the grid of Fig.41(c) even when the modes are not orthogonal over the domain.

One very important property of the least-squares technique is that if the data presented to it consists of only a linear combination of the 108 modes it attempts to resolve, then it will make no error. This is true for any observation network except for a few pathological examples (i.e. fewer observations than modes, or the presentation of a single mode sampled at the nodes of the mode). This means, that the least-square method has no direct error, and thus provides an interesting comparison to the OI procedure.

The weights - $W(i)$ in this procedure are arbitrary. For true optimality considerable experimentation would have to be performed. Consequently, we have arbitrarily set all $W(i) = 1$. There is also the possibility that one can force the analysis in the no-data regions to the first-guess field simply by inserting appropriate dummy observations of zero (when analyzing observation minus forecast data). This technique would be similar to that used in the Hough analysis scheme at NMC (Flattery, 1971). We have not attempted to exploit any of these refinements.

6.2 Experimental results

The OI and least-square methods were tested using data extracted from the 'truth' - Fig.41(a) and (b) sampled on the two observation networks Fig. 42 (a) and (c). The large-scale Rossby and Kelvin modes were obtained directly in the least-squares case and via direct projection from the uniform analysis grid in the case of OI. Four typical large-scale analyses are shown in Fig.43. Fig.43(a) shows the OI analysis for Network 1, Fig.43(b) shows the least-squares analysis for Network 1, Fig.43(c) shows the OI analysis for Network 2, and Fig.43(d) shows the least-square analysis for Network 2. Comparing these analyses with the 'true' large-scale flow - Fig.41(d), we note serious errors in all cases - particularly in the Network 2 cases. OI has a tendency to under-analyze, least-squares to over-analyze. The fit at the northern and southern boundaries is as desired.

Rather than present large numbers of analyses we used two techniques to condense the information. In Fig.44 we show the root mean square error in the large-scale Rossby and Kelvin modes as a function of zonal wavenumber for the Network 1 case. On the left is the vector wind error (ms^{-1}) and on the right the geopotential height error(m). For reference, we show in the solid black line (top panel) the variance in these waves as determined from Fig.41(d). The light solid line in the top panel is the OI error and the dashed line (top panel) is the least-squares error. It is evident, that with the possible exception of wavenumber 0, that the OI procedure is substantially better in this case.

To see why this is so, we have done further experiments with OI, shown in the bottom panel. Here, we have repeated for reference the light solid line of the top panel, but changed the scale of the ordinate. The dash-dot line is the
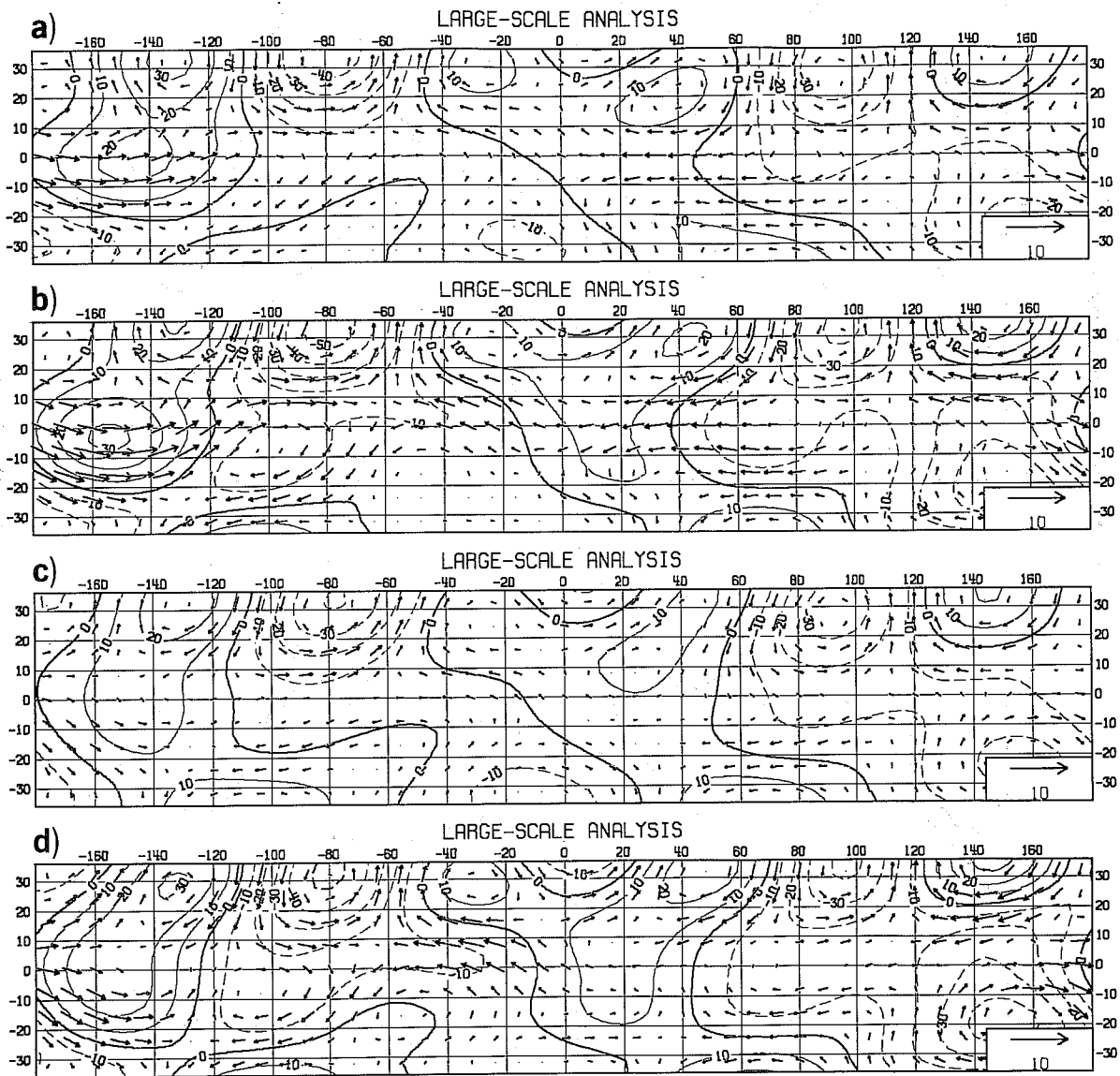
Fig. 43   Resulting large-scale analyses for 4 cases – (a) Network 1- OI, (b)
Network 1 - Least-squares, (c) Network 2 - OI, (d) Network 2 -
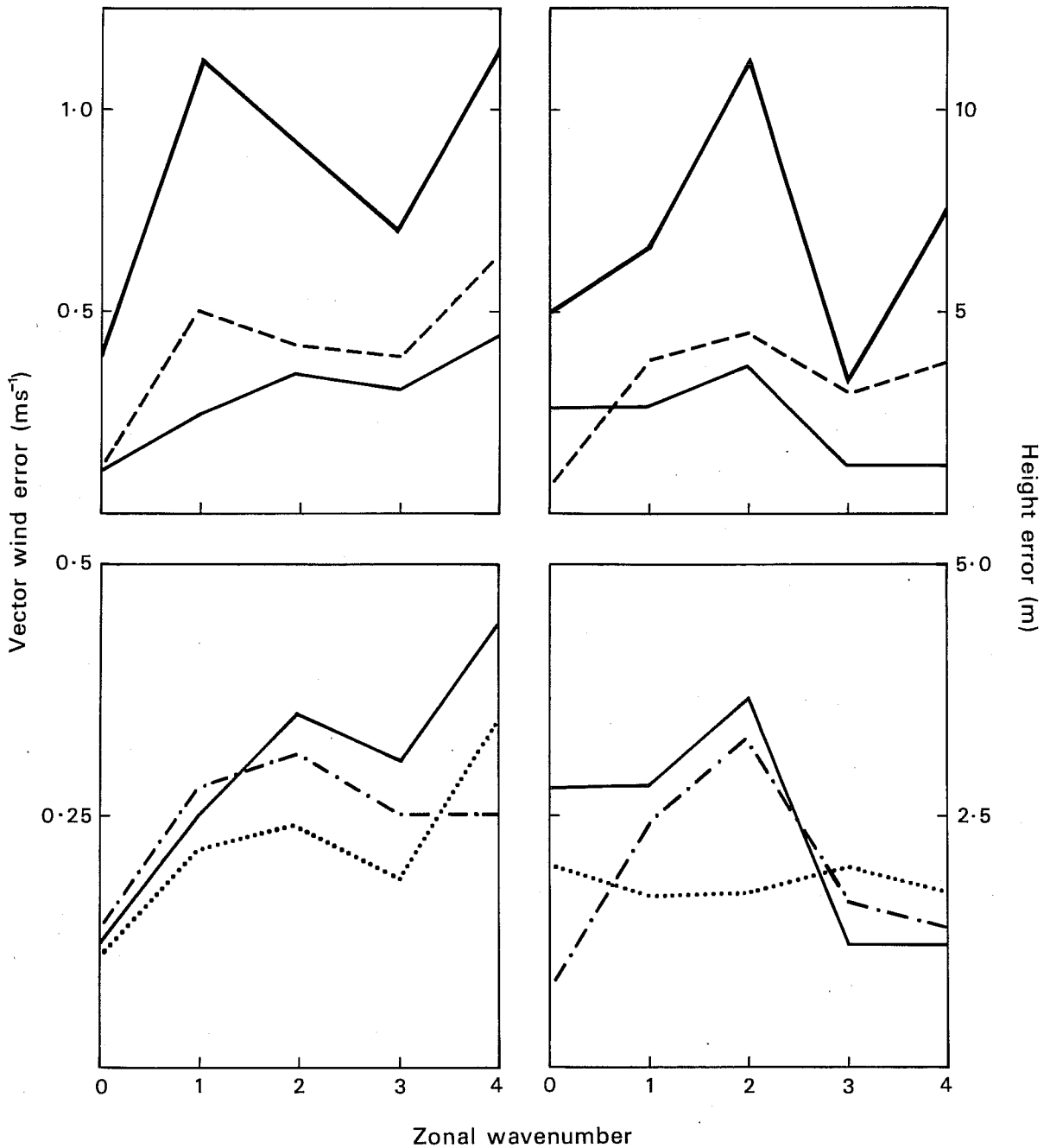Least-squares. The format of each panel is the same as Fig. 41 (d).

Network 1

Fig. 44 RMS vector wind error (ms^{-1}) - left panels and geopotential height
error (m) - right panels as function of zonal wavenumber in the
Rossby and Kelvin modes for Network 1. In the top panel are shown
the variance in the Rossby and Kelvin modes (ie. Fig. 41 (d)). The
dashed curve shows the error for the Least-square method and the
light solid curve shows the error for the OI method. In the lower
panels the light solid curve is repeated. The dotted curve shows
the aliasing from the short waves into the large-scale Rossby and
Kelvin waves for the OI method. The dash-dot curve shows the response
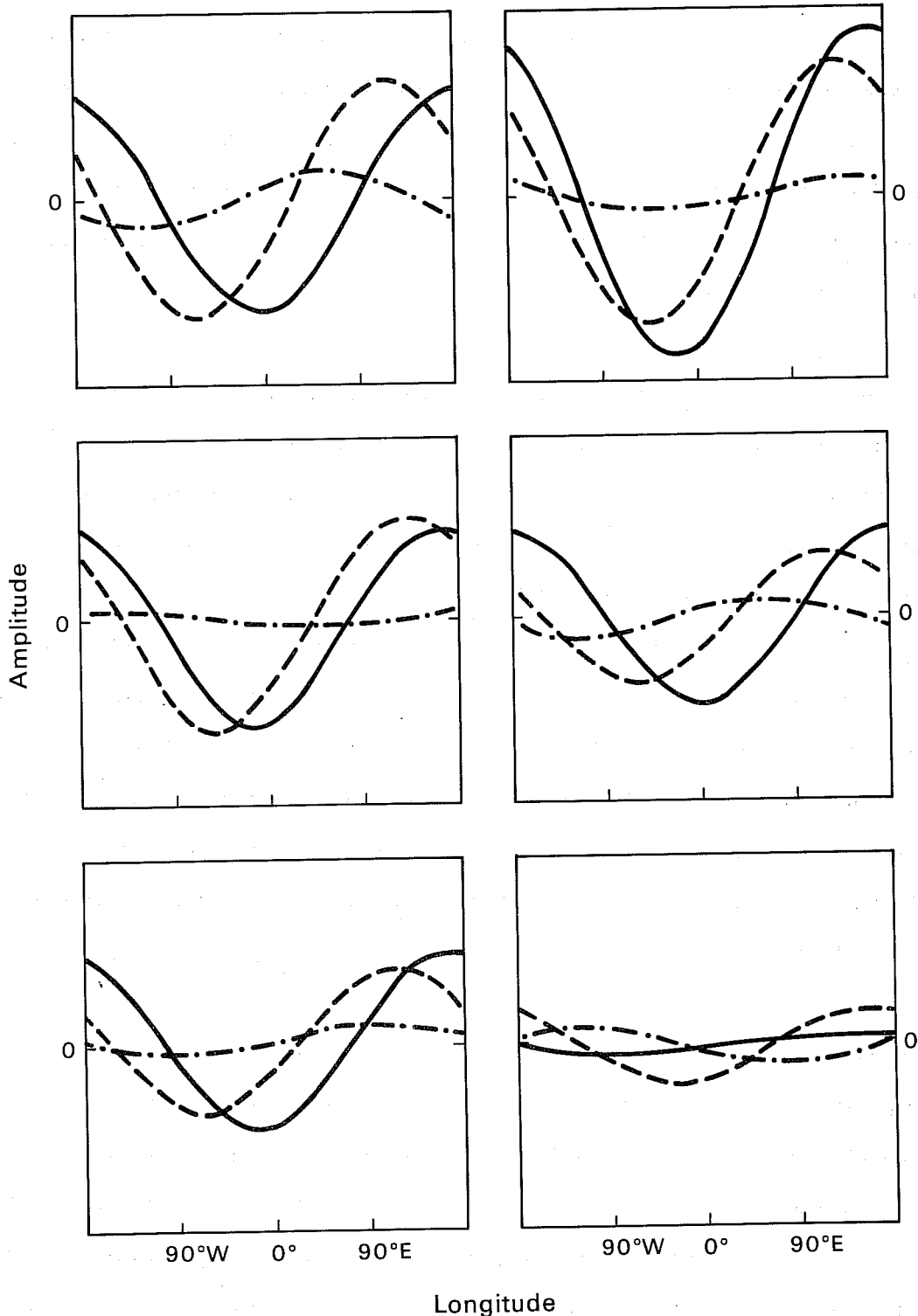of the OI system to the input of large-scale Rossby and Kelvin waves.

Fig. 45 The gravest symmetric Rossby mode (solid), Kelvin mode (dashed) and mixed Rossby-gravity mode (dash-dot) of wavenumber 1 as function of longitude (degrees). The ordinate is amplitude. The upper left hand panel is the truth . The upper right panel is the Least-square analysis. The middle left is the OI analysis. The remaining panels all describe OI experiments. The middle right is the OI response to the three individual waves. The lower left is the OI response to the input of all large-scale Rossby and Kelvin modes. The lower right shows the alaising into the 3 modes from small-scale input. This figure is for Network 1.

OI large-scale error if the analysis is presented only with the Rossby and Kelvin waves of Fig.41(d). The dotted line is the error in the large-scale Rossby and Kelvin modes if the the OI scheme is presented with all the remaining modes (i.e. 'truth' minus Rossby and Kelvin modes). These remaining modes would thus consist of all the small-scale modes plus the large-scale gravity modes. Basically, the dash-dot curve measures direct error, the dotted curve is the indirect error.

Now the total OI large-scale error (light solid) is made up of both types of error. We note, however, that the total error curve is usually less than the square root of the sum of the squares, which means that the two types of error must be negatively correlated to some extent. In some cases the total error is less than either the direct or indirect. We note that the direct error has much the same shape as the original variance spectrum (dark solid), but that the indirect error is fairly flat. This result might perhaps have been anticipated, because the OI procedure is designed to analyze a complete spectrum, which is more like the 'truth' of Fig.41(a) and (b) than the large-scale 'truth' of Fig.41(d). Although the least-squares technique has no direct error, its indirect error is substantial in this case, and thus it produces an inferior large-scale analysis.

A second method of examining these analysis methods is to display the response of three seperate long waves under different experimental conditions. Normally, the amplitude and phase of a long wave would be presented as a vector on a polar diagram. We choose instead to multiply the cosine and sine components of each long wave amplitude by the relevent cosine and sine of longitude and display as a function of longitude. One can also think of this presentation as a plot of z or u for a given mode as a function of longitude for any fixed latitude. In Fig.45 we show 3 zonal wavenumber 1 modes for Network 1. They are the gravest symmetric Rossby (solid), Kelvin (dashed), and mixed Rossby-gravity (dash-dot). In the upper left hand corner is the 'truth'. In the upper right is the least-squares analysis and the
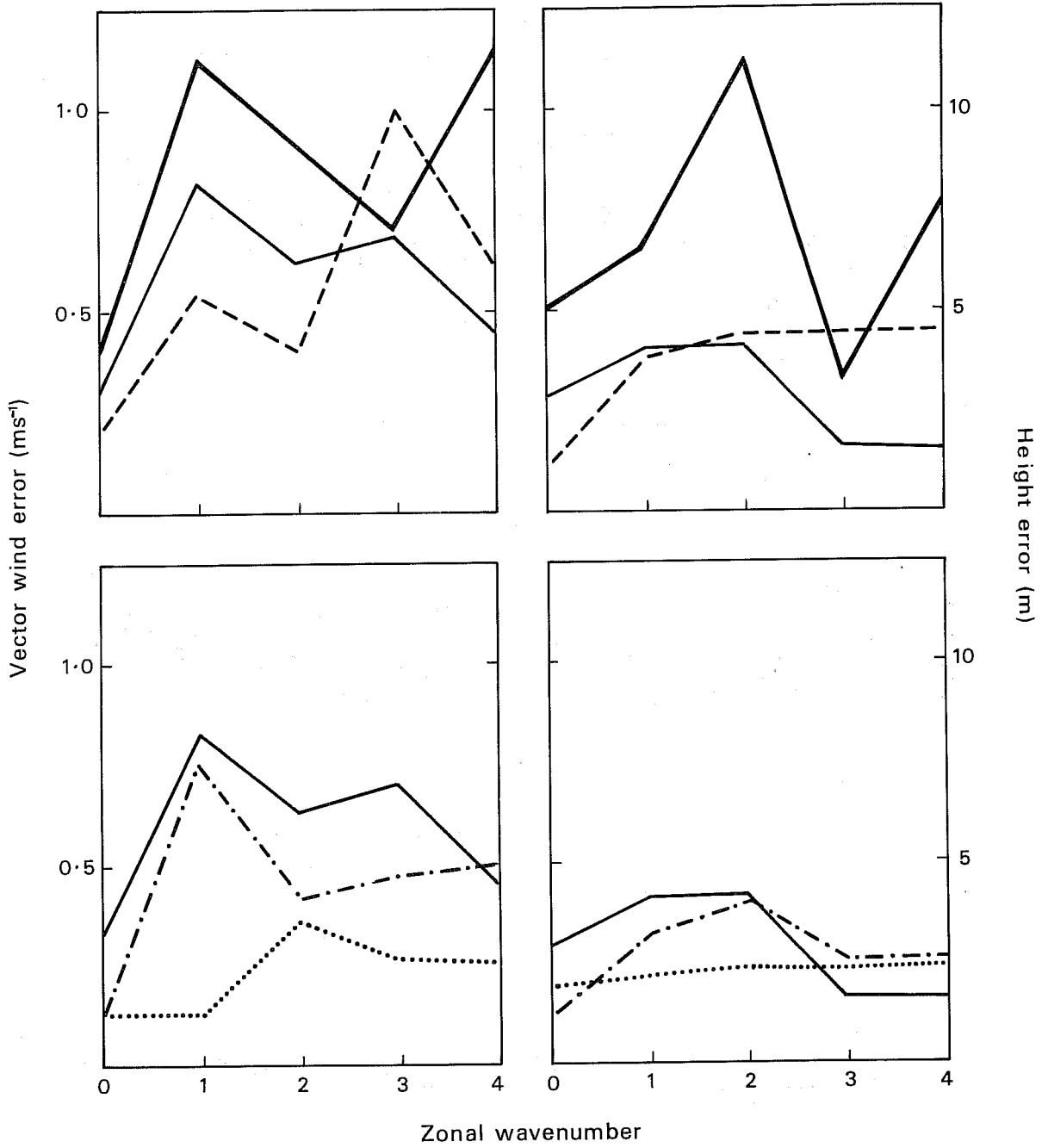
Network 2

Fig. 46 Same as Fig. 44 except for Network 2.
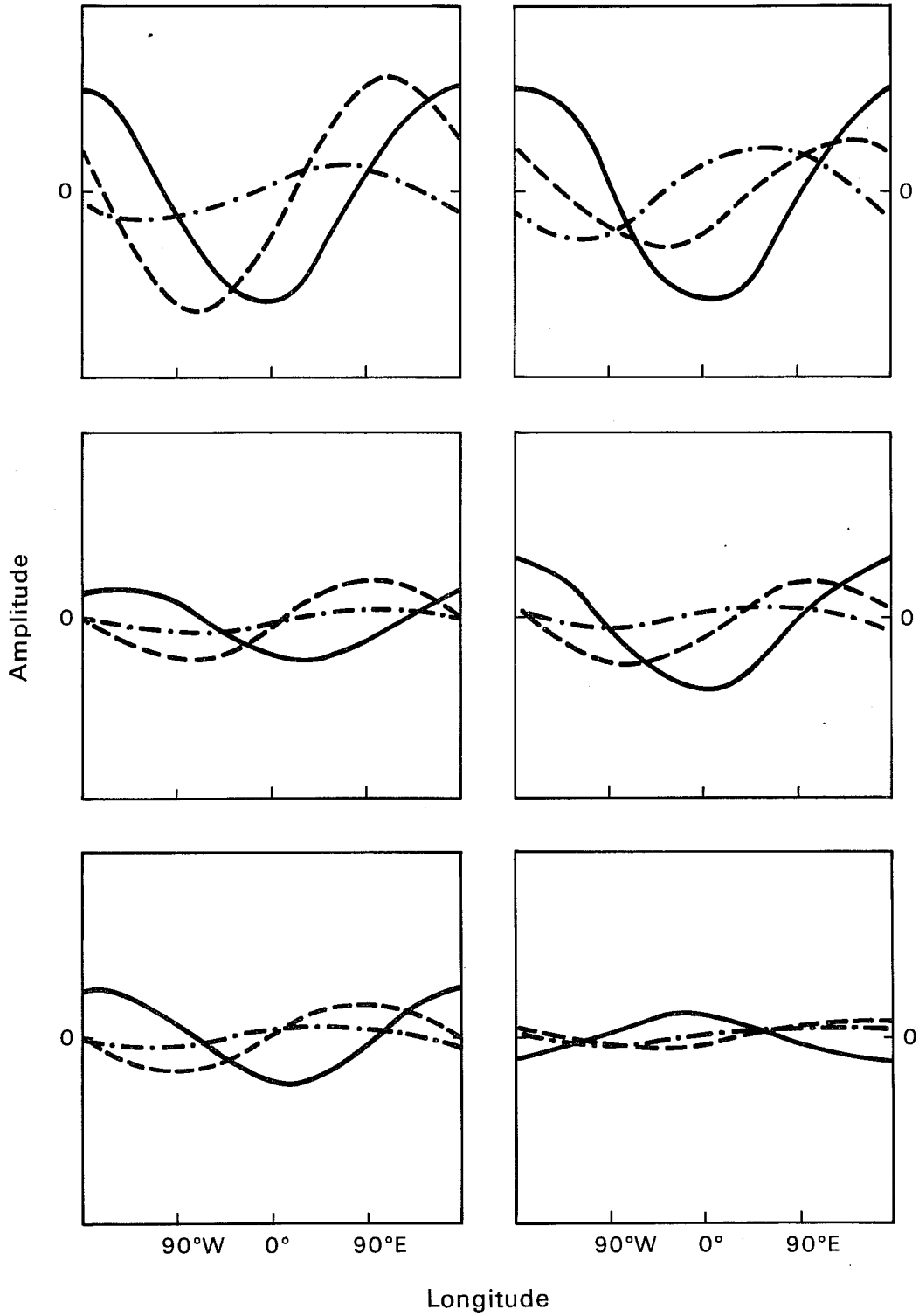
Network 2

Fig. 47 Same as Fig. 45 except for Network 2.

middle left the OI analysis. It is evident that the least-squares is overdrawing and the OI slightly underdrawing. The relatively low amplitude mixed Rossby-gravity wave is completely mis-analyzed by both methods.

In the remaining panels of Fig.45 we show 3 OI experiments. In the middle right panel are shown three sub-experiments in which the OI scheme was presented with each of the 3 modes in turn. In the lower left panel we presented the OI scheme with all the large-scale Rossby and Kelvin modes simultaneously (as in dash-dot curve of Fig.44). In the lower right we presented to the OI the 'truth' minus Rossby and Kelvin waves (as in dotted curve of Fig.44). It is evident that the middle right and lower left panels are similar; also, the negative correlation can be seen again when examining the Kelvin wave in the middle left and lower right and left.

In Figs.46 and 47 we show the Network 2 counterparts of Figs.44 and 45 in the same format. Fig.46 demonstrates how much worse the error is with Network 2 and that for waves 0,1 and 2 the least-squares procedure seems better than OI. In Fig.47 the least-squares clearly produces a better result as the OI seriously underdraws. Surprisingly enough, the phase errors are not too bad.

All of the experiments so far considered perfect observations. We did one experiment to consider the effect of random observation error. Using Network 2, we constructed random observation errors from a normal distribution with mean zero and standard deviation of 22.16 meters for height and 6.913 ms^{-1} for wind (the same as in the 'truth' of Fig.41(a) and (b)). We then looked at the error in the large-scale flow caused by this random observation error (the 'true' signal was set to zero). The results for OI (light solid) and least-squares (dashed) are shown in Fig.48 (top panel). As expected the OI procedure is much less sensitive to random observation error.
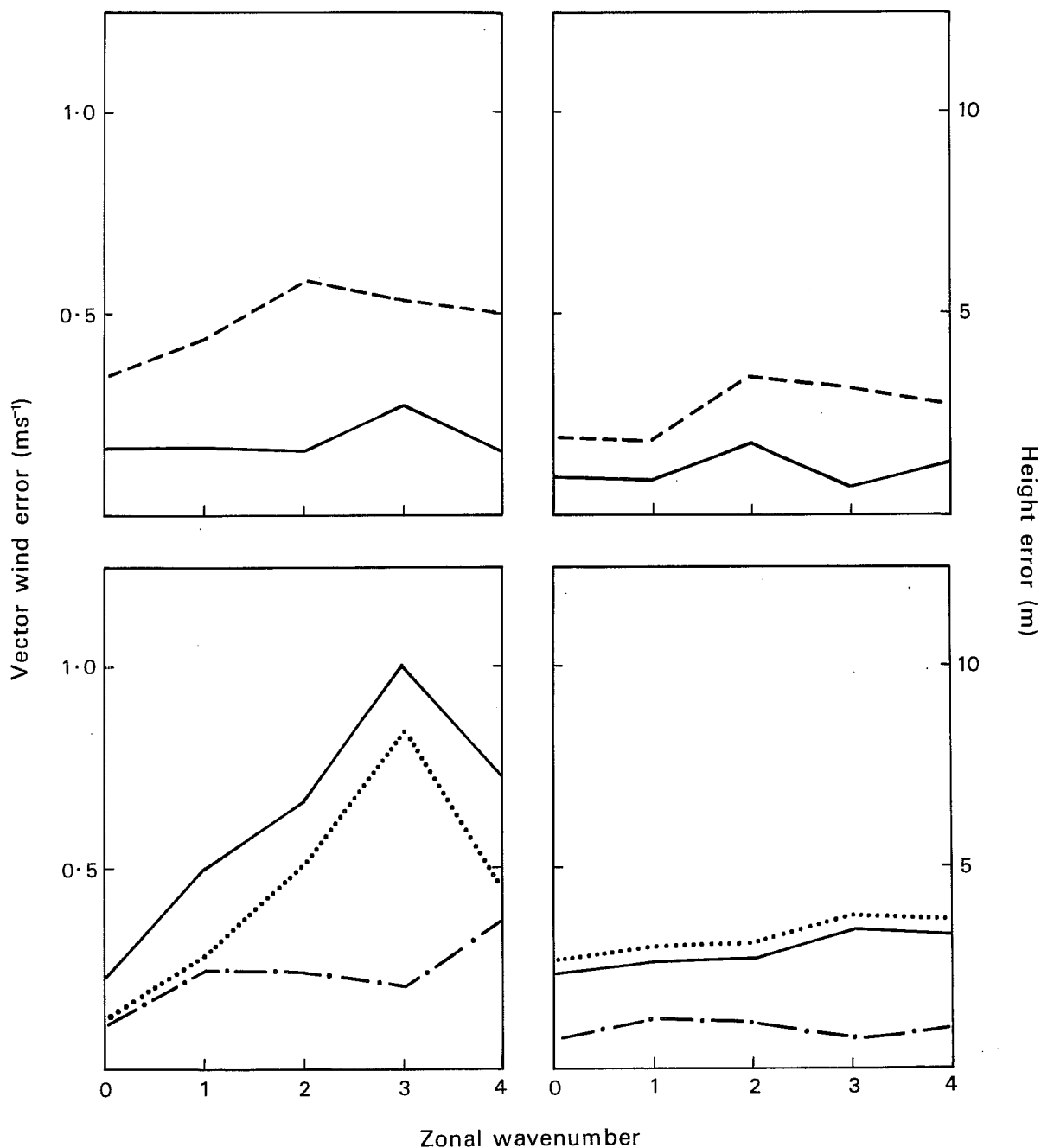
Network 2

Fig. 48 Same format as Fig. 46. Top panel shows the large-scale error for OI (light solid) and Least squares (dashed) for input of random observational error. Bottom panel shows the large characteristic scale OI experiment (b increased by a factor of 5 with a large search radius). Total error is light solid, indirect error is dotted, direct error is dash-dot.

The uniform network experiments at Sect. 4.2 suggested that the long-wave response could be improved by increasing the characteristic scale b to make it more consistent with the scale of the long waves. Several experiments were performed with Network 2 to see if the same result followed. Firstly, b was increased to a value 5 times its normal size (i.e. approximately 3000 km in Northern Hemisphere). This had virtually no effect on the long wave analysis (although it drastically affected the short wave analysis). Next, using the large value of b we modified the data selection so that the data search radius was increased from 800 km to 3200 km. In this way, data from much further away was used in the low observational density regions.

The simultaneous increase in b and the search radius had a dramatic effect on the long wave analysis as can be seen in Fig. 48 - lower panels. In this figure, in the same format as Fig.46 - lower panel - are plotted the total OI error (light solid), direct error (dash-dot) and indirect error (dotted). As compared with Fig. 46 - lower panel, the direct error has been reduced dramatically - as expected. Unfortunately, the indirect error (aliasing from smaller scales) has increased substantially. The net result is somewhat better in waves 0-1, but worse in waves 3-4. It would appear that increasing b (and modifying data selection) produces much the same effect as the least-squares analysis (which has no direct error, but a substantial indirect error). It might be noted that the random observational error for the large b experiment also produces considerable long wave error.

The large long wave errors due to aliasing from smaller scales and observational noise in the least squares and large b OI experiments might be explained as follows. The true longwave signal in the observation increments has relatively small amplitude compared to either the shortwave signal or the observational noise and this makes it difficult to detect accurately except with a network of uniform density.

6.3 Experimental summary

In this section we have examined some of the problems of large-scale analysis with non-uniform observational networks. We have examined both direct errors as in Cats and Wergen (1982) and indirect errors (aliased from smaller scales). Both OI and a least-squares technique with no direct error have been examined.

In general, the results agree with those of Cats and Wergen(1982) - particularly for Network 2, which is the one most analagous to the three-dimensional network that they used. Thus, the large-scale Rossby and Kelvin modes are not well analyzed at all by either OI or least-squares. The smaller amplitude modes such as the mixed Rossby-gravity mode are completely incorrect. It would appear that the more optimistic results of Leary and Thompson (1973) and Baer and Tribbia (1976) are primarily due to the over-simplified nature of their experiments, i.e. restriction in dimensionality, restriction to higher latitude and restriction to a univariate analysis procedure.

In general, the OI procedure seems to yield better results than least-squares, although there is some indication that for sparse networks and very long waves, least-squares may be better. Both direct and indirect errors are important in the OI large-scale analysis but there is some cancellation between them. The OI technique is much superior in suppressing random observation errors.

These experiments (and those of Cats and Wergen - 1982, Leary and Thompson - 1973, and Baer and Tribbia - 1976) were static experiments in which only a single analysis was done from the data assumed collected over a single analysis cycle (6 hours at ECMWF). The results of this experiment show that

the large-scale analysis produced in this way is inadequate. We note,
however, that Figs.44-48 show that the longwave errors, although large, are
generally less than 100%. This means that even for the long waves, the
analysis if generally closer to the "truth" than is the first guess. Thus, if
Networks 1 or 2 were to be used in a forecast-analysis cycle with a "perfect"
model, the longwave analysis would eventually converge to the "truth" (within
observation error). It is the implicit assumption of the forecast-analysis
cycle, that the major reduction in error occurs through the forecast
operation, and that a somewhat lesser reduction occurs through the analysis
operation. The present results show that the reduction in longwave error
through the analysis operation is very small and thus the veracity of the
final long wave analysis will be very dependent upon the accuracy of the
forecast model.

7. CONCLUSIONS

The definition of the initial state of the atmosphere is of crucial importance in deterministic forecasting. Initial errors would still rank near the top in most subjective assessments of the causes of forecast errors. Despite this, objective analysis has had relatively less attention than other aspects of the forecast-analysis cycle. This relative neglect is manifested in a paucity of good pedagogical material and an under emphasis in training courses. Nonetheless, objective analysis provides a wealth of interesting and worthy scientific problems to attract the research scientist.

Our aim in the present work was to explore a number of different aspects of objective analysis - with particular reference to multi-variate statistical analysis (OI). Our approach was midway between a strictly theoretical statistical approach and a synoptic examination of specific analysis situations. Thus, we tended to treat the objective analysis system as a largely unknown operator, whose properties we wished to determine. Generally, we presented this operator with well-controlled, idealized inputs and examined the outputs to determine the response of the operator. We had a variety of parameters internal to the operator which were under our control, and could thus determine responses by sweeping through parameter space.

Our study was highly constrained in one direction, that is, we confined all our work to the two-dimensional horizontal problem, and completely neglected the very important vertical problem. On the other hand, we used a particularly general form of the prediction error correlation, which allowed greater flexibility in the horizontal problem. The prediction error correlation used at ECMWF has a free parameter μ which describes the geopotential-streamfunction correlation or alternatively, the strength of the

geostrophic coupling. In the same spirit, the present prediction error correlation introduces three new parameters - ν (the ratio of the divergent wind error to the total wind error), λ (the streamfunction-velocity potential correlation) and $\lambda*$ (the geopotential-velocity potential correlation). ν corresponded to a shrinking or stretching of the wind-wind prediction error correlation while λ or $\lambda*$ corresponded to rotation.

Calculations with atmospheric data and a literature search suggested that λ and $\lambda*$ were very small, but that ν was non-negligible. The parameter ν was defined to be 0 for a completely non-divergent prediction error correlation (the value in the present ECMWF system). ν was defined to be 1 for a completely divergent prediction error correlation. The value of ν obtained from atmospheric data was approximately .1.

We developed two forms of the prediction error correlation, the Gaussian model which is presently in use at ECMWF and a second order autoregressive model which we refer to as the Markov model. Both models have one free parameter corresponding to their characteristic scale. The Markov model had a much more spread-out height-height correlation and much more concentrated wind-wind correlation than the Gaussian model.

We wished to examine three seperate aspects of the objective-analysis system:

- multi-variate relationships

- analysis of divergent tropical flows

- analysis of tropical large-scale flows

In the main body of the work (Sects. 3-6) we developed a number of techniques for examining these problems. In general, each of these sections and sub-sections have been oriented around a particular technique and not

111

around one of three aspects listed above. We will attempt here to summarize

our conclusions for each of the three above aspects in turn, with material

drawn from the entire body of the study.

7.1 Multi-variate relationships

Much of the theoretical work in objective analysis in general and OI in

particular has been univariate and somewhat less emphasis has been placed on

multi-variate aspects. We concentrated on two particular multi-variate

relationships - the geostrophic relationship and the non-divergence

relationship - both of which were under our control through the free

parameters μ and ν defined above.

Multi-variate relationships serve two functions. Firstly, they can act as

filters against types of flow which are considered undesirable. Thus, by

setting $\mu=1$, it is possible to minimize the amount of ageostrophic or anti-

geostrophic flow in the analysis. Similarly, by setting $\nu=0$, it is possible

to minimize the response of the analysis system to divergent flow. Secondly,

in the case of μ, if only geopotential or only wind observations are

available, it is possible to get an estimate of the unobserved variable.

It is well-known that OI is linear in the observations, it is less well-known

that OI is highly non-linear in μ and ν. For example, in the case of μ, we

can define $\mu=1$ as the geostrophic limit and $\mu=0$ as the uncorrelated limit. If

we examine the matrix of analysis weights, we find that the analysis weights

do not vary linearly as μ is varied. Thus, if $\mu=.9$, the analysis weights are

already halfway between the geostrophic and uncorrelated limits and by $\mu=.5$

the weights are virtually the same as in the uncorrelated limit. The same

result hold true for ν. This suggests that unless the constraint is applied

rigorously, i.e. μ near 1 and ν near 0, it will be ineffective. Conversely, if

it is considered desirable to have a non-geostrophic or divergent analysis, the constraints $\mu=1$ or $\nu=0$ have only to be relaxed slightly.

An analysis of the eigenstructure of the prediction error correlation confirmed this conclusion. In this form of analysis, it was easy to show how the ageostrophic and divergent eigenvectors were completely suppressed at $\mu=1$ and $\nu=0$. When the constraints were even slightly relaxed, the response of the ageostrophic and divergent eigenvectors increased rapidly. The results with the Markov model were quite different. In particular, the Markov model had much less sensitivity to variations of μ and ν, and for $\mu=1$ and $\nu=0$, the Markov model was much less effective in suppressing ageostrophic and divergent structures. Thus the Markov model would tend to produce a "noisier" analysis. We were also able to show that the reason that the ageostrophic eigenvectors existed when $\mu=1$ (assumed geostrophy) was because the analysis was discrete and not continuous.

The eigenvector analysis suggested that when $\mu=1$ and there is a supporting geostrophically consistent wind, the height will be better analyzed. This result was confirmed by examining the spectral response on a two-dimensional f-plane of the OI procedure.

7.2 Analysis of divergent tropical flow

Our more general form of the prediction error correlation permitted for the first time a serious examination of the analysis of divergent flow. The simple experiments discussed in Sect. 7.1 suggested that a value of ν which was non-zero but still small might improve the analysis of divergence. This was further supported by examination of the spectral response of the OI system to the input of divergent structures. Thus in the present ECMWF systems ($\nu=0$) only divergent structures of very large-scale and even then only with a reasonably fine observation network are well-drawn. The response at $\nu=0$ was largely confirmed by an examination of the divergent kinetic energy spectrum in the FGGE analysis. When ν is allowed to increase to the suggested value of .1, the divergent response is much improved.

We tested the more general prediction error correlation on two real data cases taken from the FGGE year. They were both 200 mb tropical cases where it had been conjectured that the deficiencies in the operational divergent wind analyses were due to the operational setting of $\nu=0$. There had been some concern expressed that setting $\nu=.1$ would result in 'noisier' analyses. This did not turn out to be the case. In some cases, the analyses were not very sensitive to variations of ν. In one case, at least, there was considerable improvement in the divergent wind analyses when ν was increased to .1. We found that setting $\nu=.1$ produced an analysis which was less sensitive to the more arbitrary aspects of OI, such as data selection. In general, we found that the Markov correlation model produced 'noisier' results than the Gaussian model.

7.3 Analysis of large-scale tropical flow

Recent results of Cats and Wergen (1982) have cast some doubt on the quality of large-scale tropical analyses. They did experiments which suggested that there were non-negligible errors with uniform observation networks and alarming errors with realistic observation networks.

We completed a whole hierarchy of experiments to examine this problem. We first calculated the estimated analysis error for simple one-dimensional uniform networks in which the scale of the input information was different from that assumed in the prediction error correlation. This allowed us to produce plots of estimated analysis error as a function of observation spacing and sub-population characteristic scale. Several problems in the analysis of the large-scale were immediately apparent. There were, first of all, several difficulties in determining the winds from the heights and vice versa in the large-scale. In effect, the geostrophic relationship ($\mu=1$) is not appropriate on these scales and causes difficulties. Perhaps more

serious, was a substantial underdrawing of the large-scale windfield for larger observation spacing (of the order of 1.5 times the assumed characteristic scale of the prediction error correlation). The reason for the underdrawing was the negative lobes of the wind-wind correlation. It was thought that this problem might be potentially serious in the tropics where μ is assumed small.

These results were confirmed by uniform network two-dimensional f-plane experiments which determined the spectral response of the OI procedure. There were further uniform network experiments on the sphere, in which various large-scale Rossby and Kelvin modes were presented to the analysis system. There were serious deficiencies in the response of OI to the input of these modes. In particular, the tropical windfield was seriously underdrawn and the flow was forced to be geostrophic at too low a latitude. However, for these uniform network experiments most of the large-scale analysis problems could be rectified by using a prediction error with a much larger characteristic scale. In our two-dimensional context, we could not examine the serious vertical problem noticed by Cats and Wergen (1982).

Lastly, we examined the analysis of the large-scale tropical flow with a realistic observation network. We defined a tropical domain and specified two realistic observation networks. We defined a 'truth' which we hoped would have the spectral characteristics of the observed minus forecast field and yet would be known everywhere. We sampled the 'truth' on the two networks and produced analyses using OI. We then calculated the analyzed large-scale flow using direct projection from the uniform analysis grid and compared with the 'true' large-scale flow. We considered two types of large-scale error. Direct error is the error caused by a poor response of the objective analysis system to the input of large-scale structures. Indirect error is the error caused by aliasing from the smaller scales into

the large-scale due to a non-uniform observation network. We also tested a
least-squares analysis procedure which has no direct error and the correct
large-scale multi-variate relationships and compared it to OI.

We found that, in general, OI was more accurate in the large-scale than the
least-squares technique. Although the OI procedure has both direct and indirect
error, they tend to be somewhat negatively correlated, resulting in lower total
error. OI was also more effective in suppressing random observation error. For
very long waves, and sparse networks, however, the least-squares technique was
more accurate. Both techniques produced very poor results in the large-scales
with observation networks which we considered realistic.

7.4 Discussion

The use of slightly divergent prediction error correlation functions ($\nu \neq 0$)
looked fairly promising and should be pursued. This step alone will not
solve all the problems of the divergent wind analysis however. The vertical
problem with the coupling between high level outflow and low level inflow
must also be addressed. The use of infra-red data to define the high level clouds
would also be useful. The coupling between the analyzed divergence and the
convective parameterization should also be further examined.

With respect to the analysis of the large-scale tropical flow, our results
confirmed those of Cats and Wergen(1982). The results suggested that all the
data available in a 6 hour time window is insufficient to adequately define
the large-scale tropical flow. This result is at variance with earlier
studies of Leary and Thompson (1973) and Baer and Tribbia(1976). Our
least-squares technique, which was by no means completely exploited, looked
promising, but there are obvious limits defined by the observation network.

Although, it can be argued that observations coming in over several days might be adequate to define the stationary and transient parts of the large-scale tropical flow, this has not been proven. We know that large-scale forecast errors are still appreciable, especially in the medium range, and it may well be that initial large-scale tropical error is an important contributing factor.

REFERENCES

Ahlqvist, J.E. 1982: Normal-mode global Rossby waves: Theory and observations. J. Atmos. Sci., 39, 193-202.

Alaka, M. and R. Elvander 1972: Optimum interpolation from observations of mixed quality. Mon. Wea. Rev., 100, 612-624.

Baer, F. and J. Tribbia, 1976: Spectral fidelity of gappy data. Tellus, 28, 215-227.

Boer, G. and T. Shepherd, 1983: Large-scale two dimensional turbulence in the atmosphere. J. Atmos. Sci., 40, 164-184.

Buell, C., 1960: The structure of two-point wind correlations in the atmosphere. J. Geophys. Res., 65, 3353-3366.

Buell, C., 1971: Two-point wind correlations on an isobaric surface in a non-homogeneous non-isotropic atmosphere. J. Appl. Met., 10, 1266-1274.

Cats, G. and W. Wergen, 1982: Analysis of large-scale normal modes by the ECMWF analysis scheme. ECMWF Workshop Proceedings on "Current Problems in Data Assimilation" (available from ECMWF).

Flattery, T.W. 1971: Spectral models for global analysis and prediction. Proceedings of the Sixth AWS Technical Exchange Conference, U.S. Naval Academy, 1970, Air Weather Service, Report 142, 42-53.

Gandin, L., 1963: Objective analysis of meteorological fields. Israel Program for Scientific Translation. Jerusalem, 1965, 242 pp.

Halberstam, I. and S. Tung 1983: Objective analysis using orthogonalized discrete Hough Function vectors. Pre-print volume. 6th Conference on Numerical Weather Prediction, Omaha, Nebraska, June 6-9, 1983).

Hollingsworth, A., 1984: ECMWF Lecture Notes.

Hollingsworth, A. and G. Cats, 1981: Initialization in the Tropics. Workshop on Tropical Meteorology and its Effects on Medium Range Weather Prediction at Middle Latitudes. European Centre for Medium Range Weather Forecasts. March 11-13, 1981, 105-115.

Julian, P., 1980: Data assimilation for the FGGE Tropical Observing System. ECMWF Seminar on Data Assimilation Methods, 15-19 September 1980, 375-395.

Julian, P. and J. Thiebaux, 1975: On some properties of correlation functions used in optimum interpolation schemes. Mon. Wea. Rev., 103, 605-616.

Leary, C. and R. Thompson, 1973: Shortcomings of an objective analysis scheme. J. Appl. Met., 12, 589-594.

Lorenc, A., 1979: Meteorological data analysis. ECMWF Lecture Note No. 3, 68 pp.

Lorenc, A., 1981: A global three-dimensional multivariate statistical interpolation scheme. Mon. Wea. Rev., 109, 701-721.

Mesinger, F. and A. Arakawa, 1976: Numerical methods used in atmospheric models. GARP Publications Series No. 17 - Global Atmospheric Research Program - WMO. Secretariat of the World Meteorological Organization, Case Postale No. 5, CH-1211 Geneva 20, Switzerland.

Ramanathan, Y., P. Kulkarni and D. Sikka, 1973: On a study of winter season wind structure at 500 mb in the Indian Region, for use in objective analysis of the wind field. J. Appl. Met., 12, 977-983.

Schlatter, T., 1975: Some experiments with a multivariate statistical objective analysis scheme. Mon. Wea. Rev., 103, 246-287.

Seaman, R., 1975: Distance-time autocorrelation functions for winds in the Australian region. Aust. Met. Mag., 23, 27-40.

Seaman, R. 1977: Absolute and differential accuracy of analyses achievable with specified observational network characteristics. Mon. Wea. Rev., 105, 1211-1222.

Seaman, R. and D. Gauntlett, 1980: Directional dependence of zonal and meridional wind correlation coefficients. Aust. Met. Mag., 28, 217-221.

Starr, V.P., J.P. Peixoto and W.E. Gaut 1970: Momentum and zonal kinetic energy balance of the atmosphere from five years of hemispheric data. Tellus, 22, 251-274.

ECMWF PUBLISHED TECHNICAL REPORTS

No. 1   A Case Study of a Ten Day Prediction

No. 2   The Effect of Arithmetic Precisions on some Meteorological Integrations

No. 3   Mixed-Radix Fast Fourier Transforms without Reordering

No. 4   A Model for Medium-Range Weather Forecasting - Adiabatic Formulation

No. 5   A Study of some Parameterizations of Sub-Grid Processes in a Baroclinic
        Wave in a Two-Dimensional Model

No. 6   The ECMWF Analysis and Data Assimilation Scheme - Analysis of Mass
        and Wind Fields

No. 7   A Ten Day High Resolution Non-Adiabatic Spectral Integration:
        A Comparative Study

No. 8   On the Asymptotic Behaviour of Simple Stochastic-Dynamic Systems

No. 9   On Balance Requirements as Initial Conditions

No.10   ECMWF Model - Parameterization of Sub-Grid Processes

No.11   Normal Mode Initialization for a multi-level Gridpoint Model

No.12   Data Assimilation Experiments

No.13   Comparison of Medium Range Forecasts made with two Parameterization
        Schemes

No.14   On Initial Conditions for Non-Hydrostatic Models

No.15   Adiabatic Formulation and Organization of ECMWF's Spectral Model

No.16   Model Studies of a Developing Boundary Layer over the Ocean

No.17   The Response of a Global Barotropic Model to Forcing by Large-Scale
        Orography

No.18   Confidence Limits for Verification and Energetics Studies

No.19   A Low Order Barotropic Model on the Sphere with the Orographic and
        Newtonian Forcing

No.20   A Review of the Normal Mode Initialization Method

No.21   The Adjoint Equation Technique Applied to Meteorological Problems

No.22   The Use of Empirical Methods for Mesoscale Pressure Forecasts

No.23   Comparison of Medium Range Forecasts made with Models using Spectral or
        Finite Difference Techniques in the Horizontal

No.24   On the Average Errors of an Ensemble of Forecasts

No.25   On the Atmospheric Factors Affecting the Levantine Sea

No.26   Tropical Influences on Stationary Wave Motion in Middle and High Latitudes

ECMWF PUBLISHED TECHNICAL REPORTS